ELECTRON TUNNELING STUDY OF SURFACE AND CORRELATION EFFECTS IN BI-LAYERED LANTHANUM-STRONTIUM MANGANITES

BY

DANIEL MAZUR

Submitted in partial fulfillment of the
requirements for the degree of
Doctor of Philosophy in Physics
in the Graduate College of the
Illinois Institute of Technology

Approved _____
Advisor

Chicago, Illinois
December 2006

ACKNOWLEDGMENT

I would like to thank Dr. John F. Zasadzinski, my academic advisor at Illinois Institute of Technology (IIT), and Dr. Kenneth E. Gray, my research leader and supervisor at Argonne National Laboratory (ANL), whose tutoring and encouragement at every stage of my doctorate program was invaluable, and who guided me through the dissertation process. I also wish to thank Dr. Liam Coffey, Dr. Marco Saraniti and Dr. Carlo U. Segre, all from IIT, who served in my dissertation Committee, for their time and for the feedback and encouragement I was receiving from them.

This Dissertation could not have been written without my colleagues Dr. Hong Zheng and Dr. John F. Mitchell from ANL, who provided me with the world's best single crystals of bi-layered LSMO. Neither could it have been written without the help I received from Dr. Herbert Schmidt and Dr. Lütfi Özyüzer, who introduced me to point contact tunneling instrumentation, measurements and data analysis. My greatest thanks go also to Dr. Igor Beloborodov, who greatly helped me to understand the theory of electron-electron interactions in metals.

For the permission to use their facilities and instruments I would also like to thank Dr. Vladimír Matolín from the Surface Physics Division at Charles University (CUNI) in Prague, and Dr. John W. Freeland and Dr. Richard A. Rosenberg from ANL. For their help with various experimental tasks my thanks go to Dr. Jon M. Hiller and Dr. Helmut Claus from ANL, and Dr. Kateřina Veltruská and Mgr. Miloš Cabala from CUNI. I also would like to express my appreciation to Mrs. Joy Calderone, the BCPS Department Coordinator at IIT, for the great administrative help I was receiving during my entire graduate appointment.

TABLE OF CONTENTS

LIST OF TABLES

LIST OF FIGURES

LIST OF SYMBOLS

Symbol	Definition
i	Imaginary Unity
π	Ludolf Number
e	Electron Elementary Charge
μ_0	Permeability Constant
$\hbar$	Planck Constant
k_B	Boltzmann Constant
$\delta(x)$	Dirac Delta-Distribution
$f(\mathcal{E})$	Fermi Function at Energy $\mathcal{E}$
d	Number of Dimensions
N	Number of Inelastic Tunneling Channels
α	Inter-layer Coupling Strength in the Quasi 2D Model of Metals.
A, A_0	Point Contact Junction Area, and a Thin-Film Junction Area of a Known Size, Respectively
a, c	Lattice Constants In-Plane and Out-of-Plane, Respectively
a, b, c	Coefficients of a Polynomial Expansion of Tunnel Current in Powers of Voltage
B_0	External Magnetic Field
$c(V_{max}), \tilde{c}(V_{max})$	Scaling Parameters of the Low-Bias and High-Bias Memory Effect, Respectively
δ_1, δ_2	Doping Boundaries of Certain Phases of the Bi-Layered LSMO at Doping 50% and 60%, Respectively
D	Tunnel Barrier Matrix Element

$\mathcal{D}, \mathcal{D}_{ab}, \mathcal{D}_c$	Diffusion Constant, and Its ab-Plane and c-axis Contribution, Respectively
d_{nn}	Nearest-Neighbor Distance Between Atoms in a Solid
d_0	Inter-Layer Distance in a Quasi Two-Dimensional Metal
e_g, t_{2g}	Sub-Bands of Manganese $3d$ Band
$\vec{E}$	Intensity of an Electrostatic Field
$E, \mathcal{E}$	Energy
E_x	Projection of Electron Kinetic Energy in the Direction of Tunneling
$\mathcal{E}_F$	Fermi Energy
$\mathcal{E}_{CO}$	Characteristic (Crossover) Energy of the DOS Correlation Effect
E_m, E_n	Energy of Electron State with Quantum Number m and n, Respectively
Ψ_m, Ψ_n	Wavefunction of Electron State with Quantum Number m and n, Respectively
$\Sigma_m, \Sigma_{\mathcal{E}}$	Energy Correction to the State with Energy E_m, and Mean Energy Correction to States of Energy $\mathcal{E}$
BE, KE	Photoelectron Binding and Kinetic Energy, Respectively
KE^{vacuum}	Kinetic Energy of a Photoelectron with Respect to the Vacuum Level
$KE^{analyzer}$	Kinetic Energy of a Photoelectron with Respect to the Analyzer
$\Phi_{sample}, \Phi_{analyzer}$	Workfunction of Sample and Analyzer, Respectively
Φ, V_Φ	Tunnel Barrier Height and the Corresponding Voltage
t_0	Tunnel Barrier Thickness

$\Delta\Phi, \Delta t_0$	Absolute Error of Barrier Height, and Barrier Thickness in Fitting Data with a Coherent Tunneling Model for Junction Area Calibration
$f(x), \phi(x/2)$	Functions Supplying the Energy and Temperature Dependence of the Electron-Electron Interactions DOS Effect by Alt'shuler and Aronov, and by Abrikosov, Respectively
x, y	Generalized Argument and Parameter of the Electron-Electron Interaction Correction to the Density of States
γ_{TF}	Thin-Film Junction Conductance per Unit Area
G	Alternative Symbol for Tunneling Conductance dI/dV
$G(0)_{TF}, G(0)_{PC}$	Zero-Bias Conductance of Thin-Film and Point-Contact Tunneling Junctions, Respectively
$G(0)^m, G(0)^{exp}$	Zero-Bias Conductance of Model and of Experimental Tunneling Data, Respectively
G_0, R	Zero-Bias Junction Conductance and Corresponding Resistance
H	Magnetic Field Strength
χ	Ratio Between Zero-Bias Conductances of Two Simulated Tunneling Current Characteristics
χ^2	Mean Quadratic Difference as a Measure of a Fit Quality
$I, I_T, \Delta I$	Tunnel Current and Tunnel Current Change
I^{exp}, I^{fit}	Experimental Tunnel Current and Fit to Tunnel Current, Respectively
$\vec{j}, J$	Current Density in Bulk Material and Through a Tunnel Junction, Respectively
$k, q, \vec{q}$	Wavevector (Quasimomentum) of Electron in a Metal
k_x, k_y, k_z	Wavevector (Quasimomentum) Cartesian Coordinates
k_F	Fermi Wavevector (Quasimomentum)
λ_F	Fermi Wavelength

λ_0	Screened Coulomb Potential in the $\vec{q}, \omega \to 0$ Limit
λ_ν	Dimensionality Crossover Parameter in the Density-of-States Correlation Effect
L_{e-e}	Screening Length of Electron-Electron Coulomb Interactions in a Metal
$\bar{l}$	Elastic Mean Free Path
$\mu, \mu_{tip}, \mu_{sample}$	Chemical Potential, Tip Chemical Potential, and Sample Chemical Potential, Respectively
M	Magnetization
m_0, m	Free Electron Mass and Effective Electron Mass, Respectively
m_t, m_l	Effective Mass in a Quasi Two-Dimensional Metal In-Plane and Out-of-Plane, Respectively
ν_0, ν_{0d}	Uncorrelated Density of States and the Same with Specified Dimensionality, Respectively
ν, ν_d	Correlated Density of States, and the Same with Specified Dimensionality, Respectively
$\delta\nu, \delta\nu_d$	Density of States Correlation Effect, and the Same with Specified Dimensionality, Respectively
ω	Angular Frequency, Fourier Transform of Time
$\Pi(\vec{q}, i\omega)$	Polarization Operator of a Metal in Diffusive Mode
p_d	Numeric Coefficient in Theory of Electron-Electron Interactions
p_F	Fermi Momentun
p_t, p_l	Quasimomentum in a Quasi Two-Dimensional Metal In-Plane and Out-of-Plane, Respectively
ρ, ρ_{ab}, ρ_c	Bulk Resistivity, the *ab*-Plane Resistivity, and the *c*-Axis Resistivity, Respectively
ρ_{max}, ρ_{exp}	Maximum Metallic Resistivity, and the Experimental Resistivity, Respectively

$\vec{r}, r$	Position and Distance in Three-Dimensional Real Space
r_A, r_B	Atomic Radii of Elements A and B
$\sigma, \sigma_{ab}, \sigma_c$	Bulk Conductivity, the ab-Plane Conductivity, and the c-Axis Conductivity, Respectively
τ	Elastic Scattering Time
$\bar{\tau}, \bar{\tau}_1, \bar{\tau}_2$	Mean Elastic Scattering Time, and the Same for Distinguished Elastic and Inelastic Expansion Fits of Tunneling Background, Respectively
τ_-, τ_+	Elastic Scattering Time Estimated from Negative and Positive Branch of the Normalized Tunneling Conductance, Respectively
T	Absolute Temperature
t	Time
$U(r), U(q)$	Static Electron Coulomb Potential, and Fourier Transform of the Same, Respectively
$U(q, i\omega)$	Fourier Transform of the Dynamically Screened Electron Coulomb Potential in Real and Phase Space Coordinates, Respectively
$V, \Delta V, V_{max}$	Voltage, Voltage Change, and Maximum Voltage Experienced by a Junction, Respectively
v, v_x	Electron Group Velocity and Its Projection in the Direction of Tunneling, Respectively
v_F	Fermi Velocity
$\hat{x}, \hat{y}, \hat{z}$	Unit Vectors of a Cartesian System of Coordinates
hf	Photon Energy
$F(E)$	Detector Efficiency Function
F_{xx}	Relative Sensitivity Factor in XPS Quantitative Analysis

$\gamma, \delta, \zeta, \phi$	Angular Dimensions of Respective Positions of the Radiation Source, the Sample, and the Photoelectron Detector
I_A	Intensity of a Photoelectron Spectral Peak
I^ϕ	Intensity of a Photoelectron Spectral Peak for Sample at Angle ϕ
J_0	Comprehensive Constant of Proportionality in XPS Quantum Analysis
λ_{IMFP}	Inlastic Mean Free Path
λ_{xx}	Inelastic Mean Free Path in Material xx
L_A	Coefficient of Angular Asymmetry
Σ	Illuminated Sample Area
s_A, S_A	Photoionization Cross-Section and Analyzer Sensitivity Factor for a Spectral Line of Element A, Respectively
ξ	Concentration of an Element in a Compound
x, y, z	Spatial Coordinates along Sample in Photoelectron Spectroscopy

ABSTRACT

In this thesis we report a discovery of electron-electron interaction effect in the electronic density of states of $La_{1.28}Sr_{1.72}Mn_2O_7$ single crystals. This correlation effect was found using the point contact electron tunneling spectroscopy at liquid helium temperatures. The correlation effect exhibits energy dependence $\sqrt{\mathcal{E}}$ near Fermi energy, in agreement with the first-order perturbation theory of electron-electron interactions in three-dimensional and quasi two-dimensional metals. We have verified the existence of an insulating phase on the surface of the bi-layered $La_{1.28}Sr_{1.72}Mn_2O_7$ by evaluation of the tunneling barrier effect in the tunneling spectra. We were able to observe the conservation of states of the density-of-states correlation effect and identify the characteristic energy scale as $\mathcal{E}_{CO} = 30 - 50$ meV. To our best knowledge, this is the first work that reveals state conservation of the electron-electron interaction effect. We used the available theory to derive estimates of the elastic scattering time τ from the low-energy $\sqrt{\mathcal{E}}$ proportionality, and based on the characteristic energy scale $\mathcal{E}_{CO}$. The obtained values of $\tau = 15 \pm 3$ fs are by about a factor of 3 larger than the published results of angle-resolved photoelectron spectroscopy, which is, however, within the limits given by the theory we used in our analysis. Apart from the tunneling experiments we also performed measurement of depth profile of the lanthanum and strontium relative concentration near surface by x-ray photoelectron spectroscopy. In the calibrated range $6-24$ Å we observed no deviation from the bulk nominal concentration. We conclude that the surface strontium enhancement observed by others, if it occurs, is localized to depths smaller than 6 Å.

CHAPTER 1
INTRODUCTION

1.1 Overview

We found a correlation effect in the density of states of the $La_{1.28}Sr_{1.72}Mn_2O_7$ single crystals, using point contact tunneling spectroscopy. This effect, caused by Coulomb interaction between electrons in solids, has so far been scarcely observed. Together with available results of the quantum interference measurements in the same material we were able to derive a fundamental parameter of conducting solids, the elastic scattering time τ, within the framework of Al'tshuler's and Aronov's perturbation theory of electron-electron interactions in disordered metals. By careful evaluation of the tunneling characteristics at intermediate voltages we observed conservation of the density of states by the correlation effect. Based on this we were able to evaluate the typical energy scale of the correlation, a quantity which to this date has not been experimentally evaluated from state conservation of the electron-electron interaction.

In order to present our results in a compact way, the thesis begins with an overview of current knowlegde about manganites, and in particular the group of bi-layered single-crystal $La_{2-2x}Sr_{1+2x}Mn_2O_7$ (LSMO). As we studied the correlation effect in the density of states (DOS) of LSMO in metallic phase, we present an outline of the elementary theory of metallic conductivity in the introduction. An overview of the double-exchange (DE) model of metallic conductivity in manganites, on the other hand, is added in Appendix A. The same is true for the basics of quantum interference effect in conductivity of metals, as a supplementary material it has been added in Appendix B. In the theoretical introduction we focus on the existing theory of electron-electron interaction effect on the metallic DOS. The key part comes with the theory by Alex A. Abrikosov, who expanded the original Al'tshuler and Aronov's theory of the correlation effect in disordered metals to layered, quasi two-dimensional

metals. Surface properties of the bi-layered LSMO 36% were crucial for success of the point contact spectroscopy and we introduce them in the final section of this chapter.

The second chapter is dedicated to a concise summary of the theory of electron tunneling spectroscopy as it applies to our measurements and procedures of data analysis. This is where we present our evaluation of the voltage regions suitable for the fitting of the tunneling background. Description of the point contact instrument used in the measurements follows.

With Chapter 3 presentation of our experimental results begins. Firstly we introduce the correlation effect as it has been observed in the tunneling conductance. In order to verify the tunneling character of point contact junctions between gold tip and the bi-layered LSMO 36%, we fit the general features of the wide-voltage-range I(V) spectra with simulated spectra a simple model of coherent tunneling through a rectangular barrier. In the process of doing this, we evaluate the appropriateness of the use of Simmons' expansion in the low-bias limit, for analysis of our spectra at intermediate voltages. Having separated the tunnel barrier effect from the correlation effect in the tunneling conductance, we could normalize the tunneling conductance, observe the conservation of states by the correlation effect, and make estimates of the elastic scattering time τ in LSMO 36%.

There is a number of mechanisms in solid state tunneling, which have been seen to produce similar zero-bias anomalies in the tunneling conductance to the electron-electron interaction effect in the density of states. In Chapter 4 we discuss the alternative sources of zero-bias anomalies in a separate chapter. In the course of this we present our observation of an effect in the tunneling spectra, which is likely to be related to the change in the surface insulating barrier potential profile. We show that this barrier effect is not the source of the zero bias anomaly we analyze as a DOS correlation effect.

Apart from point-contact measurements, we have also sputtered thin gold films on freshly cleaved surfaces of LSMO 36%, and measured the $I(V)$ spectra of thin film gold/bi-layered LSMO junctions. The obtained spectra allowed us to utilize the model of tunneling through a rectangular barrier for calibration of the areas of the point contact junctions (Chapter 5). Our application of this procedure is, to our knowledge, unique among tunneling studies. Although our calibration is also burdened by a significant error, it gives us an improved length scale of surface homogeneity.

Finally, we performed x-ray photoemission measurements to investigate the chemical composition of the bi-layered LSMO surfaces, and we present our results in Chapter 6. There have been observations of changes of chemical composition in manganites near their surfaces, and recently this has been reportedly observed in the bi-layered LSMO as well. Such change of composition near surface could be identified as the reason for surface insulating behaviour. We found that in the measured region of electron escape depths $\sim 6 - 24$ Å the chemical composition does not observably change. This experiment stands apart from all the rest of the thesis and therefore this one chapter contains all necessary: the overview of the theory of x-ray photoemission spectroscopy (XPS), instrumentation overview and results.

Due to format and style requirements imposed on Ph.D. thesis by the Graduate College of Illinois Institute of Technology, all figures are printed in greyscale. Figures reprinted from other sources may be available in color in the original publications. More importantly, the figure captions had very limited length allowance, which lead to a significant deviation from the caption forms common in scientific journals. Therefore, detailed descriptions and discussions of *all* figures were included in the text, whether or not the respective figure caption contains a phrase "Figure Described in Detail in the Text" or similar. Wherever this phrase was used, it indicates that reading the relevant passage in text is *strongly* recommended for understanding.

1.2 Historical Milestones of Manganite Research

Manganese oxides, widely known as manganites, have been studied since 1950's, when Jonker and van Santem [27][1] reported ferromagnetism in $(La, Ca)MnO_3$, (La, Sr)-MnO_3 and $(La, Ba)MnO_3$ mixed crystals. While antiferromagnetic (AF) order would seem to be a natural ground state, when the crystals are viewed as systems of fixed interacting magnetic dipoles, the existence of ferromagnetism (FM) and the observed correlation between ferromagnetism and metallicity were intriguing. Both was explained by Zener [62, 63], who proposed that FM order arises from the energy considerations of electron delocalization. This delocalization is allowed by a coherent carrier motion from the originating Mn ion to the neighboring oxygen and from this oxygen to the target neighboring Mn ion. Since two simultaneous processes of electron transport are involved in the model, the mechanism was called *double-exchange model* (DE). The DE model, as well as it's limitations, are outlined in Appendix A.

Manganites and were then studied at a moderate pace over several decades, and the first measurement of manganite magnetoresistance (MR) was done by Searle and Wang in 1969 [52]. At the beginning of 1990's, very large magnetoresistance values started to come, as measured by Kusters et al. in 1989 [31] and von Helmolt et al. in 1993 [58]. Eventually, the present explosion of world-wide interest in manganites was produced by the discovery of "colossal" magnetoresistance (CMR) in manganite thin films reported by Jin et al. in 1994 [26] and Xiong et al. in 1994 [60]. Since then study of manganites evolved into one of the main areas of research within the area of magnetics and strongly correlated electrons.

In 1999 Okuda et al. [43] measured temperature dependence of bulk conductivity of a metallic phase of a bi-layered lanthanum-strontium manganite and found

---

[1]Reference [27] in Bibliography

a deviation from behavior typical for metals. They observed that the $\sigma(T)$ dependence is one characteristic to metals in dirty limit, or else metals near a metal-to-insulator transition. The suggested mechanism causing this conductivity deviation was quantum interference, which has been known to arise in disordered metals. Quantum interference was later directly observed by Li et al. [34], but it did not seem to fully explain the conductivity deviation from metallic behavior. At the same time research focused on exploration of the electronic density of states near Fermi energy begun. This has been done using angle-resolved ultra-violet photoelectron spectroscopy (ARUPS) [36] and scanning tunneling spectroscopy (STS) [49] thus far and the results will be described below. There are limitations to both these methods that may seriously affect the interpretation of the results, partly inherent in the methods, partly due to surface effects seen on the bi-layered lanthanum-strontium manganite in a metallic phase [18]. Research described in this thesis focuses at measurement of the electronic density of states near Fermi energy using the point contact tunneling spectroscopy. Auxiliary methods have been used for sample characterization, such as temperature dependence of magnetization and x-ray photoelectron spectroscopy.

1.3 Structure and Phase Diagram of the Bi-Layered LSMO

1.3.1 Crystal Structure. The general chemical formula for the mixed manganese oxides (manganites) is $T_{1-x}D_xMnO_3$. In this formula, T is a trivalent element, usually rare earth, and D is a divalent element, usually alkaline. More specifically, the formula is precisely valid for manganites in *perovskite* structure, which is displayed in Figure 1.1a. Its unit cell is nearly cubic, with a manganese ion in the body center, oxygen ions in the face centers, and a combination of T and D ions in the vertices. The structure is stable enough to allow production of single crystals for large ranges of ratios of T and D concentrations (this ratio x also represents the *hole doping*), although there are also ranges of x, where only mixtures of separate phases or no

long range order at all can be manufactured. Perovskite structure, as described above, is a member of a family of Rudlesden-Popper structures with general formula $(\mathrm{T,D})_{n+1}\mathrm{Mn_nO_{3n+1}}$. The idea of these structures is that the near-cubic unit cells as in Figure 1.1a can be arranged in a variery of *superlattices*. The Rudlesden-Popper series describes the elementary unit cells close-packed in single-, double- or generally n-layers, which are separated by a (T,D)O rocksalt layer. Experimentally, perovskites can be grown as single-crystals or thin films (using sputtering techniques), while the n-layered structures can only be grown from melt as single crystals. The work presented in this thesis focused on bi-layered lanthanum-strontium manganites, i.e. T = La, D = Sr, and $n = 2$ as shown in Figure 1.1b, whose formula can be written as $\mathrm{La_{2-2x}Sr_{1+2x}Mn_2O_7}$. From this point onward, the acronym LSMO optionally followed by a percentage (e.g. LSMO 36%) will refer to these bi-layered lanthanum-strontium manganites, and the percentage will represent the nominal value of sample hole-doping x, e.g. 36% stands for $x = 0.36$.

In manganites, oxygen is in the $\mathrm{O^{2-}}$ state, because it has a filled $2p$ shell. Lanthanum looses three electrons to the chemical bonds from its $6s$ and $5d$ shells, thus becoming $\mathrm{La^{3+}}$, and strontium looses two electrons from $5s$ shell becoming $\mathrm{Sr^{2+}}$.To compensate for this mixture of La and Sr oxidation states, manganese exists (according to the simplest model) in two oxidation states, $\mathrm{Mn^{3+}}$ and $\mathrm{Mn^{4+}}$. Atomic manganese has an incomplete d-shell (Mn: $[\mathrm{Ar}]3\mathrm{d}^5 4\mathrm{s}^2$). When ionized, manganese first looses the two s-shell electrons and then one or two from the d-shell. Confinement to a cubic structure of LSMO lifts degeneracy of the d-band, splitting it in two, as shown in Figure 1.2: lower-energy t_{2g} band containing d_{xy}, d_{yz} and d_{zx} electron levels, and higher-energy e_g band containing the $d_{x^2-y^2}$ and $d_{3z^2-r^2}$ levels. Both oxidation states of manganese have filled the t_{2g} band with three electrons. Hund's coupling still exists between t_{2g} and e_g levels and therefore the extra electron that distinguishes $\mathrm{Mn^{3+}}$ goes in the e_g shell with spin aligned with the three t_{2g} electrons. This becomes

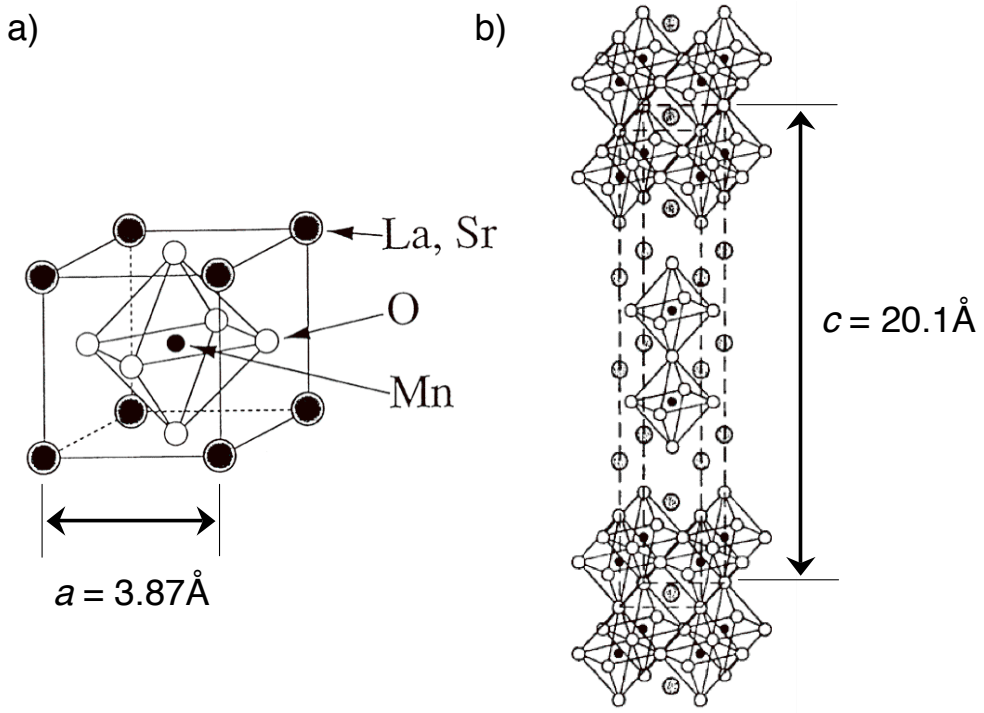

Figure 1.1. Crystal Structure of a) Perovskite and b) Bi-Layered Manganite. Values of Lattice Constants are Shown, $a = 3.87$ Å and $c = 20.1$ Å.

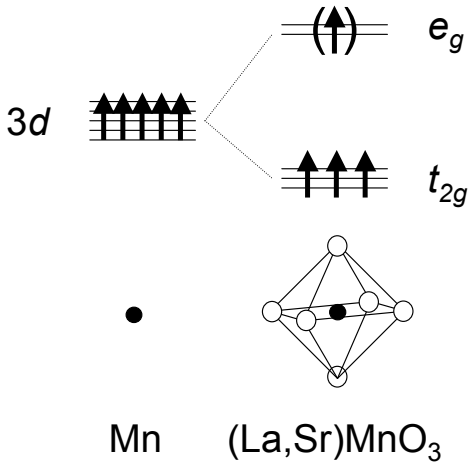

Figure 1.2. Splitting of $3d$ Band Due to Octahedral Symmetry of $(\mathrm{La,Sr})\mathrm{MnO_3}$. Degeneracy of the Resulting e_g and t_{2g} Bands May be Further Reduced by Lattice Distortions.

important in considerations of the *double-exchange* (DE) model of manganite conductivity. Understanding of double exchange is not needed in any part of this thesis, the only important fact to remember is that it leads to metallic type of conductivity. For this reason we present the DE basics in Appendix A. Concentrations of Mn^{3+} and Mn^{4+} are in the same relation as the concentration of La^{3+} and Sr^{2+}, so that the expanded chemical formula of LSMO reads $(Sr^{2+}O^{2-}) \cdot (La^{3+}_{1-x}Sr^{2+}_{x}Mn^{3+}_{1-x}Mn^{4+}_{x}O^{2-}_{3})_2$. Increase of strontium abundance in the compound then corresponds to the increase of Mn^{4+} concentration and hence the e_g hole concentration.

1.3.2 Electronic and Magnetic Phase Diagram. The LSMO exists in a variety of phases, which are under on-going exploration. The up-to-date temperature–hole doping phase diagram is displayed in Figure 1.3. It has been mentioned above that the bi-layered compounds have thus far only been successfully manufactured by growth from a melt. The procedure involves grinding and mixing amounts of La_2O_3, SrO and $SrMnO_3$ given by the desired stoichiometry, melting the mixture in a floating zone optical image furnace, and growing the LSMO single crystal boules in flowing 100% O_2. For measurements the boules are divided into small (4×4 mm and smaller) specimens, to ensure satisfactory uniformity of hole doping level across the measured samples.

To this date, $La_{2-2x}Sr_{1+2x}Mn_2O_7$ single crystals have been successfully grown at hole dopings $x \geq 0.30$. As shown in the Figure 1.3, the high-temperature phase is paramagnetic, with thermally activated transport. We choose to adopt the thermally-activated conductivity as the defining attribute of an *insulator*, although this alternative definition is not fully accepted across scientific community. Transition into a variety of phases occurs during cool-down from room temperature, at the respective Curie T_C, and Néel T_N critical temperatures drawn in Figure 1.3.

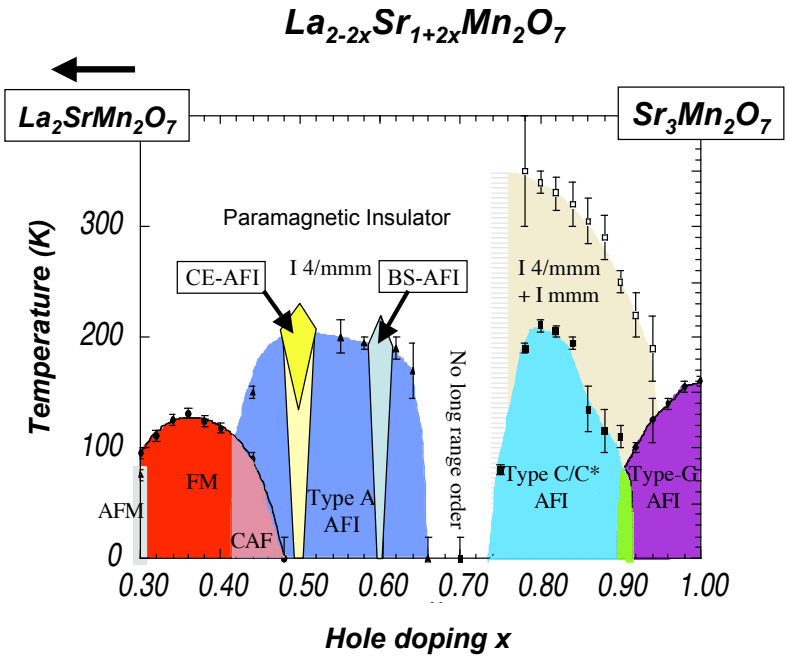

Figure 1.3. Temperature-Versus-Doping Phase Diagram of Bi-Layered Lanthanum-Strontium Manganite $La_{2-2x}Sr_{1+2x}Mn_2O_7$. Figure Is Described in Detail in the Text. Courtesy of Dr. K. E. Gray, Published with Permission.

Let us start our description of the LSMO phase diagram with the lowest doping exhibiting long-range order, the LSMO 30%. While crystal structure is the same for all doping levels and temperatures, the magnetic order and, accordingly, electrical conductivity varies. The LSMO 30% has a magnetic structure shown in Figure 1.4a, with FM-ordered bi-layers, which are arranged in an alternating anti-ferromagnetic sequence along the *c*-axis. The magnetic dipoles are oriented close to normal to the bi-layers. The LSMO 30% compound is not in focus of the research presented in this thesis, but it has been a very illustrative case for demonstration of the *double-exchange* conductivity mechanism, see Reference [35].

In the short doping range from 30% to 32%, the ground-state order of the bi-layers flips from AF to FM, as shown in Figure 1.4b. The magnetic moments remain aligned out of the bi-layer plane. The LSMO 32% below its critical temperature, in agreement with the double-exchange model, exhibits conductivity of a three-

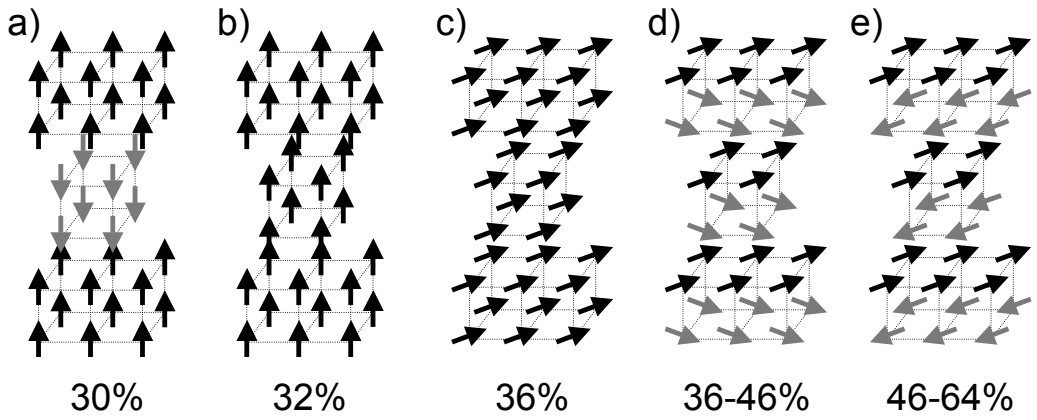

Figure 1.4. Alignment of Individual Manganese Magnetic Momenta in the Magnetic Phases of Bi-Layered Lanthanum-Strontium Manganite in the Doping Range $30\% - 64\%$.

dimensional (3D) metal. Let us point out here, what remains true for all bi-layered manganites, that even 3D-metallic phases remain strongly anisotropic in terms of bulk conductivity. Anisotropy values for select doping levels are displayed in Table 1.2 in Section 1.4.

With increased doping, the magnetic moments that were fully aligned out-of-plane in LSMO 32% start tilting, so that at the doping level $x = 36\%$ the moments all lie in the *ab*-plane, still fully FM-ordered as shown in Figure 1.4c. In agreement with the double-exchange model again, this compound is a three-dimensional metal below its critical temperature. With further increased doping, the magnetic moments rotate about the *c*-axis in such a way that the two layers within a bi-layer develop a finite angle between their magnetization vectors, see Figure 1.4d. Magnetic moments within a single layer, though, remain ordered ferromagnetically. This process is called *in-plane canting*, the resulting magnetic order has both FM and AF components, and is labeled *canted anti-ferromagnet* (CAF). The LSMO 40%, which is very similar to LSMO 36% and used to be studied much more frequently, is such canted anti-ferromagnet. The canting angle is a non-trivial function of temperature, which makes

interpretation of temperature dependencies of measurables on LSMO 40% far more complicated. This is the main reason why scientific focus shifted to LSMO 36% as a model system in the ferromagnetic-metallic phase.

As doping increases still further, the canting angle rises to 180^o so that by the time $x = 0.46$, the two layers within every bi-layer are fully anti-ferromagnetically ordered, as shown in Figure 1.4e. This AF order (it is called the *A-type anti-ferromagnet*) then remains valid for all doping levels up to $x = 0.64$. Compounds above $x = 0.74$ exist as insulators in several AF-ordered phases at low temperatures. Compounds in range $0.66 - 0.74$ do not exhibit long-range magnetic order and presumably consist of a mixture of A-type and C-type AF phases.

Let us stress out that double-exchange is not the only mechanism determining bulk properties of the anti-ferromagnetic compounds with x in the range $0.48 - 0.64$. At $x \approx 0.50$ and at $x \approx 0.60$ the electronic ground states are *charge-ordered* and *orbital-ordered*. The phase formed around $x = 50\%$ is the CE-type charge-ordered antiferomagnetic insulator (CE-AFI), and the phase around $x = 60\%$ is the *bi-stripe* anti-ferromagnet (BS-AFI). This means that, while DE predicts all the compounds with x from 0.46 to 0.64 to be two-dimensional metals, compounds with $x = 0.50 \pm \delta_1$ and $x = 0.60 \pm \delta_2$ are bulk insulators. The δ_1 and δ_2 values and the LSMO phases within their ranges are nowadays under close investigation. One can make a higher estimate as $\delta_1 \approx 0.02$ based on the fact that the LSMO 46% crystal is bulk insulator, which can be nevertheless driven to a metallic state with magnetic field of several tesla.

As reproducibility of the crystal growth varies even in this range, it is customary to measure temperature dependence of magnetization $M(T)$ of samples of each nominal composition. By comparison of the obtained curves with accepted phase diagram we ascertain the samples' actual doping x, which may vary somewhat (repro-

ducibility is approx. $\pm 1\%$) and in some parts of the phase diagram may dramatically influence the observables.

1.4 Conductivity of Metals and the Case of LSMO

In Section 1.2 we mentioned that the coexistence of metallic phase and ferromagnetism was explained by the double-exchange model proposed by Zener in 1951, see Refs. [62, 63]. The double-exchange is responsible for metallic character of conductivity of mixed manganites below respective critical temperature T_c and, therefore, for existence of finite density of states at Fermi energy. As this thesis primary topic is analysis of a correlation effect in the DOS near Fermi energy, but otherwise does not address the DE mechanism, we present an overview of the DE model in Appendix A. Below in this section, however, we overview the results of Sommerfeld theory of metals first, and after that we discuss what happens to electrical conductivity of metals, when disorder is put in the (originally periodic) crystal potential.

Modern theories of metals customarily start off with solving the problem of motion of electron wave packets in periodic potential, as an approximation of the ideal single crystal metals. Potential periodicity gives rise to forbidden regions in electronic energy spectrum, the *band gaps*, and the dispersion relation[2] $\mathcal{E}(p)$. Sommerfeld theory of electrical conductivity in metals treats conduction electrons in metals as a system of non-interacting particles, which experience collisions with the ions of the solid state metal lattice. Solution of kinetic equation, utilizing the Fermi-Dirac distribution (strictly correct only for metals in themodynamic equilibrium) of electron in conduction band, gives the relation between electrical current density $\vec{j}$ and electric field $\vec{E}$

$$\vec{j} = \frac{1}{3} e^2 \vec{E} \, [v^2 \tau \nu(\mathcal{E})]_{\mathcal{E}=\mu} \quad , \tag{1.1}$$

[2]Note that p is not momentum, it is the quasimomentum. An increase in p does not imply that the electron is accelerated.

Table 1.1. Experimental Resistivity and Maximum Metallic Resistivity Values of Several Metals.

Material	$\rho_{max}(\mu\Omega\cdot\text{cm})$	$\rho_{exp}(\mu\Omega\cdot\text{cm})$
Fe	167	10.1
Cu	257	1.7
Al	139	2.7
Au	292	2.2
Ag	292	1.47

where e is elementary charge, v is group velocity, τ is the electron's mean free path and $\nu(\mathcal{E})$ is electronic density of states (in units of $(energy \times volume)^{-1}$, containing both spin orientations), all these taken at the chemical potential μ. Taking into account Ohm's law in the form $\vec{j} = \sigma\vec{E}$, we extract the metallic conductivity σ from Eq. 1.1 as

$$\sigma = \frac{1}{3}e^2[v^2\tau\nu(\mathcal{E})]_{\mathcal{E}=\mu} \ . \tag{1.2}$$

We have chosen the notation of $[v^2\tau\nu(\mathcal{E})]_{\mathcal{E}=\mu}$, because chemical potential μ exists, whether the metal is in equilibrium or not. In quasi-equilibrium three-dimensional cases, $\mu \doteq \mathcal{E}_F$ where $\mathcal{E}_F$ is Fermi energy, and Eq. 1.2 can be written as

$$\sigma = \frac{1}{3}e^2v_F^2\tau\nu(\mathcal{E}_F) = e^2\mathcal{D}\nu(\mathcal{E}_F) \ . \tag{1.3}$$

In this equation $v_F = v(\mathcal{E}_F)$ is the Fermi velocity, and we introduced a new parameter $\mathcal{D}$, which is the coefficient of diffusion of conduction electrons. In reduced dimensionality the diffusion coefficient has a different numeric pre-factor, but its use in the right-hand expression of Eq. 1.3 stays the same.

Different materials can have very different values of conductivity, which largely reflects to what extent each real material satisfies the assumptions of the *non-interacting*

Table 1.2. Experimental Values of Bulk Resistivities and Anisotropy of LSMO. *Value of LSMO 46% Given for Its Metallic Phase at 7T.

Material	$\rho_{ab}(\mu\Omega\cdot\text{cm})$	$\rho_c(\Omega\cdot\text{cm})$	Anisotropy ρ_c/ρ_{ab}
LSMO 30%	2000	5.0	2500
LSMO 40%	770	0.13	170
LSMO 46%*	1000	0.10	100
LSMO 58%	2200	8.3	3800

electron model, on which both Drude and Sommerfeld theories of metals depend. In order to determine, if any such extension is necessary for a particular material, the concept of *maximum metallic resistivity*, ρ_{max}, was introduced. If the experimental value of resistivity ρ is well below the parameter ρ_{max}, the non-interacting electron model is appropriate for description of that particular material. If, however, $\rho \gtrsim \rho_{max}$, it is indicated to modify the model in some way. There are several approaches to estimate the limit of validity of the nearly-free electron model. We are going to use the Drude expression connecting resistivity with inelastic scattering of conduction electrons

$$\rho = \frac{m_0 v}{e^2 n_e \bar{l}} \, . \tag{1.4}$$

Here, m_0 is electron rest mass, n_e is spatial density of conduction electrons, v is velocity of conduction electrons and $\bar{l}$ is the scattering mean free path. In order to get our estimate, we use the substitution $v = v_F$ in Eq. 1.4 (rather than Maxwell-Boltzmann distribution of velocities, which Drude originally used), and the nearest-neighbor interatomic distance d_{nn} as the lower limit of mean free path $\bar{l}$. The maximum metallic resistivity estimate is then

$$\rho_{max} = \frac{m_0 v_F}{e^2 n_e d_{nn}} \, . \tag{1.5}$$

Values obtained from Eq. 1.5 using values of v_F, n_e and d_{nn} from [10] are shown in Ta-

ble 1.1 along with respective experimental values at 300 K. In Table 1.2, experimental bulk resistivity values of several LSMO compounds have been added for comparison. Because of anisotropic character of LSMO, *ab*-plane values ρ_{ab} and *c*-axis values ρ_c are distinguished. It can be seen that the maximum metallic resistivity estimate values are all in range $100 - 300$ $\mu\Omega$.cm .

Experimental ρ values for ordinary metals are about $1 - 2$ orders of magnitude *below* ρ_{max}, which verifies validity of assumptions of the basic model of metals about non-interacting electrons. It is not yet possible to reliably evaluate ρ_{max} of manganites, as their relevant Fermi velocity has not been agreed upon. If we choose to rely on the ARPES measurement by Sun et al., we can use $v_F = 3 \times 10^7$ cm/s for Fermi velocity in Eq. 1.5. The Fermi velocity value was derived from figure in [56], which we reprinted in this thesis in Appendix D. There, the free-electron model is represented by full black circles in part b) of Figure D.2. Using the density of conduction electrons relevant for LSMO 40% $n_e = 0.60 \times a^{-3}$ and $d_{nn} = a$ we calculate that $\rho_{max} = 660\mu\Omega$.cm, below the LSMO 40% *ab*-plane resistivity. The ρ_{max} ranges between 570 $\mu\Omega$.cm and 1000 $\mu\Omega$.cm for LSMO doping from 30% to 70%. Values of LSMO experimental *ab*-plane resistivities of the same order of magnitude or *above* the estimated ρ_{max} values. This motivates considering modifications to the non-interacting electron model.

A large amount of work has been done over the 20^{th} century, and especially since 1975 until now, to extend the theory of metals to accommodate materials, where the model of non-interacting conduction electrons fails. Two important effects arise from increased disorder in a metal, which are to our best knowledge relevant to the case of metallic manganites: the quantum interference and the electron-electron interactions. Quantum interference is an effect, which leaves the density of states of conduction electrons intact, but increases metallic resistivity via the diffusion co-

efficient $\mathcal{D}$ (please recall Eq. 1.3). This effect has a characteristic dependence on temperature and magnetic field. By thorough magnetoconductance experiments by Li et al. quantum interference was shown to take place in LSMO 40% [33]. The principles of quantum interference, also referred to as *weak localization*[3], as well as an overview of results of Li et al. [33, 34] are presented in Appendix B. As the key results of the magnetoconductance experiments are important for analysis of electron tunneling spectra presented in this thesis, we supply the relevant parameters in context below when presenting Abrikosov's correlation model.

1.5 Electron-Electron Interactions

1.5.1 Overview. The electron-electron interactions are an important effect of disorder in metallic systems. They influence conductivity via the density of states $\nu(\mathcal{E})$, which means that they belong to a larger category of *correlation effects* also including the electron-boson interaction effects such as superconductivity. Okuda et al. [43] suggested the occurrence of electron-electron interactions in bi-layered LSMO 40% based on the temperature dependence of bulk conductivity of the metallic phase, $\delta\sigma(T) \propto \sqrt{T}$, as predicted by Al'tshuler and Aronov [6] in 1979. Our analysis of this effect in the tunneling spectra of LSMO 36% is based on theoretical work of A. A. Abrikosov, who in the year 2000 adapted Al'tshuler's and Aronov's theory of conductivity in disordered metals to layered (quasi-two-dimensional) metals.

In three-dimensional metals these theories predict a principal $\propto \sqrt{\mathcal{E}}$ energy dependence of the DOS effect, where energy $\mathcal{E}$ is measured from Fermi energy. We are the first to report observation and analysis of these correlation effects in the density of states of bi-layered LSMO. Tunneling measurements were reported before on a number

[3]The expression "weak localization" is often used by experimentalists as a reference to either quantum interference or electron-electron interactions. The convention used by theorists, however, narrows the meaning to quantum interference effects.

of perovskites [48, 42, 41] including $La_{0.75}Sr_{0.25}MnO_3$, where qualitative agreement with the theory of electron-electron interactions was observed. We acknowledge their data as such. As neither conservation of states nor a proper fitting of the tunneling conductance were addressed by the authors in any way, the value of their analysis is reduced and the resulting values of model parameters need to be treated with caution.

1.5.2 Theory of Electron-Electron Interactions. In the short mean free path limit, the diffusion of conduction electrons is effectively slowed down, so that they spend increased amount of time within reach of each other's screened Coulomb potential. Consequentially, the electrons will be substantially influenced by the interactions among them. Interactions between electrons around Fermi level tend to change their energy distribution or, in other words, have an effect on the density of states. A rigorous theoretical treatment of the electron-electron interactions in disordered conductors is due to Al'tshuler and Aronov [5, 6, 7] and presented in a review article by the same authors, Ref. [8], which we follow almost verbatim on the following few pages.

The authors treat the electron correlation as a first-order correction in the inverse sample conductance in the theory of perturbations to the density of states. According to Al'tshuler and Aronov in [8], a correction to a state at energy $|E_m| > 0$ (from Fermi level) with wavefunction $\Psi_m(\vec{r})$ can be represented as the sum

$$\Sigma_m = -\sum_{E_n<0} \int d\vec{r} d\vec{r'} U(\vec{r}-\vec{r'}) \{ \Psi_m^*(\vec{r}) \Psi_n^*(\vec{r'}) \Psi_m(\vec{r'}) \Psi_n(\vec{r}) - \\ - \Psi_m^*(\vec{r}) \Psi_n^*(\vec{r'}) \Psi_m(\vec{r}) \Psi_n(\vec{r'}) \} \quad , \tag{1.6}$$

where E_n and $\Psi(\vec{r})$ are energies and wavefunctions of states below Fermi level and $U(\vec{r}-\vec{r'})$ is a static potential of finite range. The mean energy shift $\Sigma_{\mathcal{E}}$ averaged over

all states with energy $\mathcal{E}$ is

$$\Sigma_{\mathcal{E}} = \frac{1}{\nu_0 a^3} \sum_m \langle \delta(\mathcal{E} - E_m) \Sigma_m \rangle \quad , \tag{1.7}$$

where ν_0 is the non-interacting electronic DOS and a^3 denotes a unit volume. The quantity $\Sigma_{\mathcal{E}}$ is related to the correction to the density of states $\delta\nu$ via expression

$$\frac{\delta\nu}{\nu_0} = -\frac{\partial \Sigma_{\mathcal{E}}}{\partial \mathcal{E}} \quad , \tag{1.8}$$

which was derived by Abrahams et al. in 1981 [1]. This is the core equation that ties the energy shifts of the states to an effect in the metallic DOS ν. By expanding the right-hand side of Eq. 1.8 using Eq. 1.6, the electron-electron interaction correction to three-dimensional DOS at finite temperature can be expressed as

$$\delta\nu_3(\mathcal{E}, T) = Im \int_0^\infty \frac{d\omega}{2\pi} \int (dq) U(\vec{q}, i\omega) \nu_3 \frac{2 - tanh(\mathcal{E} + \omega/2T) - tanh(\omega - \mathcal{E}/2T)}{(-i\omega + \mathcal{D}q^2)^2} \quad , \tag{1.9}$$

and the correction to DOS in other dimensionalities can be expressed as

$$\delta\nu_{1,2}(\mathcal{E}, T) = -Im \int_0^\infty \frac{d\omega}{2\pi} \int (dq) U(\vec{q}, i\omega) \nu_{1,2} \frac{tanh(\mathcal{E} + \omega/2T) + tanh(\omega - \mathcal{E}/2T)}{(-i\omega + \mathcal{D}q^2)^2} \quad , \tag{1.10}$$

where the unperturbed total (both spins together) density of states ν_0 in d dimensions can be obtained from the standard expressions

$$\begin{aligned} \nu_{0d} &= \frac{m p_F}{\pi^2 \hbar^3} \quad , && d = 3 \\ &= \frac{m}{\pi \hbar^2} \quad , && d = 2 \\ &= \frac{1}{\pi \hbar v_F} \quad , && d = 1 \end{aligned} \tag{1.11}$$

where m represents the effective mass of the conduction electrons.

In Equations 1.9 and 1.10, $U(\vec{q}, i\omega)$ is the Fourier transform of the Coulomb interaction potential with dynamical screening given by formula

$$U(\vec{q}, i\omega) = \int d\vec{r} \mathrm{e}^{-i\vec{q}.\vec{r}} U(\vec{r}, i\omega) \quad . \tag{1.12}$$

If the potential $U(\vec{q}, i\omega)$ tends to a constant as $\vec{q}, \omega \to 0$, then the correction of the density of states will be

$$\frac{\delta\nu_d}{\nu_{0d}} = p_d \frac{\lambda_0 (k_B T)^{d/2-1}}{(\hbar\mathcal{D})^{d/2}} f_d\left(\frac{\mathcal{E}}{k_B T}\right) \quad , \tag{1.13}$$

where

$$\begin{aligned} p_d =& \frac{1}{4\sqrt{2}\pi^2} && , \quad d=3 \\ =& \frac{1}{2\pi^2} && , \quad d=2 \qquad (1.13a) \\ =& \frac{1}{2\sqrt{2}\pi} && , \quad d=1 \end{aligned}$$

$$\lambda_0 = U(0,0) - 2\overline{U(\vec{q},0)} \quad , \tag{1.13b}$$

$$f_d(x) = -\int_0^\infty \frac{dy}{2y^{2-d/2}} \frac{\sinh y}{\cosh y + \cosh x} \quad . \tag{1.13c}$$

Here, notation $\overline{U(\vec{q},0)}$ denotes an average of the statically screened Coulomb interaction potential over the whole Fermi surface. It is the parameter λ_0 alone in Eq. 1.13, which carries the information about the interaction. Note that the expression for λ_0 has been introduced in Ref. [8] as referring to the static screened potential $U(\vec{q},0)$ in the $\vec{q}, \omega \to 0$ approximation. Quite generally, λ_0 is the result of integration over q-space and over ω in Eqs. 1.9 and 1.10. Below, when we present Altshuler and Aronov's λ_0 resulting from an evaluation of the dynamically screened Coulomb interaction, we assume these had been derived from the said integration, rather than the difference between zero-point $U(0,0)$ and Fermi surface average $2\overline{U(\vec{q},0)}$.

The Fourier transform of the static (unscreened) Coulomb potential e^2/r in d dimensions is

$$\begin{aligned} U_d(\vec{q}) =& \frac{4\pi e^2}{q^2} && , \quad d=3 \\ =& \frac{2\pi e^2}{|q|} && , \quad d=2 \qquad (1.14) \\ =& e^2 ln \frac{1}{q^2 a^2} && , \quad d=1 \end{aligned}$$

While in real space the interaction potential has units of energy regardless of dimensionality, it is natural that in momentum space (q-space) the units vary. The unscreened Coulomb potential is appropriate to describe insulators, but in metals the Coulomb interaction is screened. The introduction of dynamic (ω-dependent) screening involves defining the polarization operator

$$\Pi_d(\vec{q}, i\omega) = \langle \rho(0,0)\rho(\vec{r},t)\rangle_{\vec{q},i\omega} = \nu_d \frac{\mathcal{D}q^2}{|\omega| + \mathcal{D}q^2} \quad . \tag{1.15}$$

This form of the operator is valid in the diffusion limit of metallic conductivity and there has been no further approximation involved. It can be derived from the hydrodynamic equations of Fermi liquid. Using this polarization operator we can express the screened Coulomb potential in momentum representation as

$$U(\vec{q}, i\omega) = \frac{U(\vec{q})}{1 + U(\vec{q})\Pi(\vec{q}, i\omega)} \quad , \tag{1.16}$$

where the $U(\vec{q})$ represents the unscreened Coulomb potential from Eq. 1.14 in a suitable dimensionality. Let us discuss, how this form of screened potential behaves in the limit of an insulator and in the limit of a metal in the diffusive mode. For an insulator the polarization operator vanishes at Fermi energy, as the DOS vanishes (insulating gap). Hence, the effective potential is equal to the unscreened one

$$U_d(\vec{q}, i\omega) = U_d(\vec{q}) \quad . \tag{1.17}$$

Good metals on the other hand represent the limit $U_d(\vec{q})\Pi_d(\vec{q}, i\omega) >> 1$, in which the unity in the denominator of Eq. 1.16 can be neglected. In the case of good metals then

$$U_d(\vec{q}, i\omega) = \Pi_d^{-1}(\vec{q}, i\omega) \quad . \tag{1.18}$$

Note that while $U(\vec{q})$ carries the information about electron charge, the polarization operator $\Pi_d(\vec{q}, i\omega)$ does not. Therefore, the screened potential in the limit of conduc-

tion electrons in diffusive mode[4] is practically independent of electron charge. This is an apparent paradox, because the correction to the density of states in this limit does not vanish in the "turning interactions off" limit, $e \to 0$. Resolution of this paradox lies in recognizing that the $e \to 0$ limit only has a physical meaning, when we consider its effect on the full screened Coulomb interaction potential $U_d(\vec{q}, i\omega)$ as introduced in Eq. 1.16. When we do that we observe, that as $e \to 0$, the static potential $U(\vec{q}) \to 0$. In the denominator of Eq. 1.16 the unity becomes the dominant term and therefore $U_d(\vec{q}, i\omega) \approx U(\vec{q}) \to 0$. Asymptotic equations 1.17 and 1.18 could only have been made under the implicit assumption that the electron charge e is sufficiently large. Testing behavior of the asymptotic solutions in $e \to 0$ limit is nonphysical and should be avoided. Until this point we closely followed the theory as presented in Ref. [8]. Below we present results from several other publications, and our own work that followed from them.

Alexei Abrikosov developed a theory of quantum interference and also derived the DOS correction due to electron-electron interactions in quasi two-dimensional metals. He used[5] the asymptotic expression for screened potential in the limit of metals with conduction electrons in diffusive mode. In Ref. [3] Abrikosov considered a simple quasi two-dimensional model of a metal consisting of a stack of two-dimensional metallic sheets with energy spectrum

$$\mathcal{E} = \frac{p_t^2}{2m_t} + \alpha \cos\left(\frac{p_l d_0}{\hbar}\right) \quad , \tag{1.19}$$

where p_t and p_l are the in-plane and out-of-plane Fermi momenta, m_t is the in-plane effective mass of conduction electrons, d_0 is the distance of the adjacent sheets[6], and α

[4]Valid for good metals, the diffusive mode is defined so that the elastic scattering length $\bar{l}$ is much shorter than the effective radius of the screened Coulomb potential.

[5]Igor Beloborodov, private communication.

[6]In LSMO, d_0 can be related to, e.g. the bi-layer repeat distance, which is

is the tight-binding coupling energy between the two-dimensional sheets. For metals that can be described by this model Abrikosov derived the theory of quantum interference, and also a formula for the density-of-states correction due to electron-electron interactions. The three-dimensional limit of his quasi two-dimensional expression is

$$\frac{\delta\nu}{\nu_0} = \frac{1}{\pi}\frac{\sqrt{k_B T}\sqrt{\tau}}{\sqrt{\hbar}(\frac{\mathcal{E}_F\tau}{\hbar})(\frac{\alpha\tau}{\hbar})}\phi\left(\frac{\mathcal{E}_F}{2k_BT}\right) \quad , \tag{1.20}$$

where $\phi(x)$ is defined as

$$\phi\left(x\right) = \frac{1}{\sqrt{2}}\int_0^\infty \sqrt{y}\left(cosh^{-2}(y-x) - cosh^{-2}(y+x)\right)dy \quad . \tag{1.21}$$

Note that[7] Abrikosov developed his theory as valid only in the vicinity of Fermi level, where the band structure is re-normalized and the quantity $\mathcal{E}_F$ looses correspondence with the actual Fermi energy measured from the bottom of the free-electron conduction band. As this correspondence is lost, Abrikosov chose to define it as $\mathcal{E}_F = p_F v_F$. In order to identify the differences between purely three-dimensional and the quasi two-dimensional case, we used Al'tshuler and Aronov's equations presented earlier in this section to derive the correction to the metallic DOS for a quasi two-dimensional system.

We started off with Eq. 1.13 in the three-dimensional form. It can be shown (please see Ref. [8] for details) that in three dimensions a dynamically screened Coulomb potential results in $\lambda_0 = 2/\nu_{03}$, while in the quasi two-dimensional case $\lambda_0 = 2d_0/\nu_{02} = 2\pi\hbar^2 d_0/m$. We then inserted this in Eq. 1.13 and obtain

$$\frac{\delta\nu_3(\mathcal{E},T)}{\nu_{03}} = \frac{1}{2\sqrt{2}\pi}\frac{d_0\sqrt{\hbar}\sqrt{k_BT}}{m\mathcal{D}^{3/2}}f_3\left(\frac{\mathcal{E}}{k_BT}\right) \quad . \tag{1.22}$$

Apart from λ_0, the quasi two-dimensionality also enters this formula due to considerations of the diffusive motion of electrons. We know from experiments that the c-axis

---

one-half of the c-axis lattice constant.

[7] A.A. Abrikosov and K.E. Gray, private communication.

bulk conductivity σ_c is much smaller than the ab-plane bulk conductivity σ_{ab}, as shown in Table 1.2. As $\mathcal{D}$ and σ are proportional (recall that $\sigma = e^2\mathcal{D}\nu(\mathcal{E}_F)$, Eq. 1.3), the ratio of the c-axis diffusion constant $\mathcal{D}_c$ to the ab-plane diffusion constant $\mathcal{D}_{ab}$ is just the conductance anisotropy. The expression for anisotropy used in Ref. [35] is

$$\frac{\mathcal{D}_c}{\mathcal{D}_{ab}} = \frac{\sigma_c}{\sigma_{ab}} = \left(\frac{\left(\frac{\alpha\tau}{\hbar}\right) d_0}{v_F \tau} \right)^2 \quad , \tag{1.23}$$

where τ is the elastic scattering time of electrons' diffusive motion. In a quasi two-dimensional system we recognize the term $\mathcal{D}^{3/2}$ in Eq. 1.22 as really meaning $\sqrt{\mathcal{D}_{ab}^2 \mathcal{D}_c}$. We use Eq. 1.23 to eliminate $\mathcal{D}_c$, and then use the substitution $\mathcal{D}_{ab} = v_F^2\tau/2$, and Abrikosov's definition $\mathcal{E}_F = mv_F^2 = p_F v_F$. The resulting DOS correction then is

$$\frac{\delta\nu_3(\mathcal{E},T)}{\nu_{03}} = \frac{1}{\pi} \frac{\sqrt{k_B T}\sqrt{\tau}}{\sqrt{\hbar}\left(\frac{\mathcal{E}_F\tau}{\hbar}\right)\left(\frac{\alpha\tau}{\hbar}\right)} f_3\left(\frac{\mathcal{E}}{k_B T}\right) \quad . \tag{1.24}$$

Since Al'tshuler and Aronov's function $f_3(x)$ and Abrikosov's function $\phi(x/2)$ are equal, we have hereby reconstructed Abrikosov's derivation of the electron-electron interactions effect in the density of states of a quasi two-dimensional metal in the three-dimensional screening limit.

Rather than presenting the rigorous proof, let us list the asymptotic behavior for $f_3(x)$ and $\phi(x/2)$ in limits $x \to 0$ and $x \to \infty$. The limits, naturally, agree as

$$\begin{aligned} x \to 0 \quad &: \quad f_3(x) = \phi(x) \quad = 1.07215 \quad , \\ x \to \infty \quad &: \quad f_3(x) = \phi(x/2) \quad = \sqrt{x} \quad . \end{aligned} \tag{1.25}$$

Abrikosov's perturbation theory result presented in Eq. 1.20 is well behaved in the sense that almost all of the $\phi(x)$ dependence is well approximated by one of the asymptotic expressions from Eq. 1.25. Furthermore, at a temperature as low as 4.2 K (sample temperature in most of our measurements) the limit $x \to \infty$ is a valid approximation everywhere apart from a region $\sim \pm 1.6 k_B T$ around Fermi

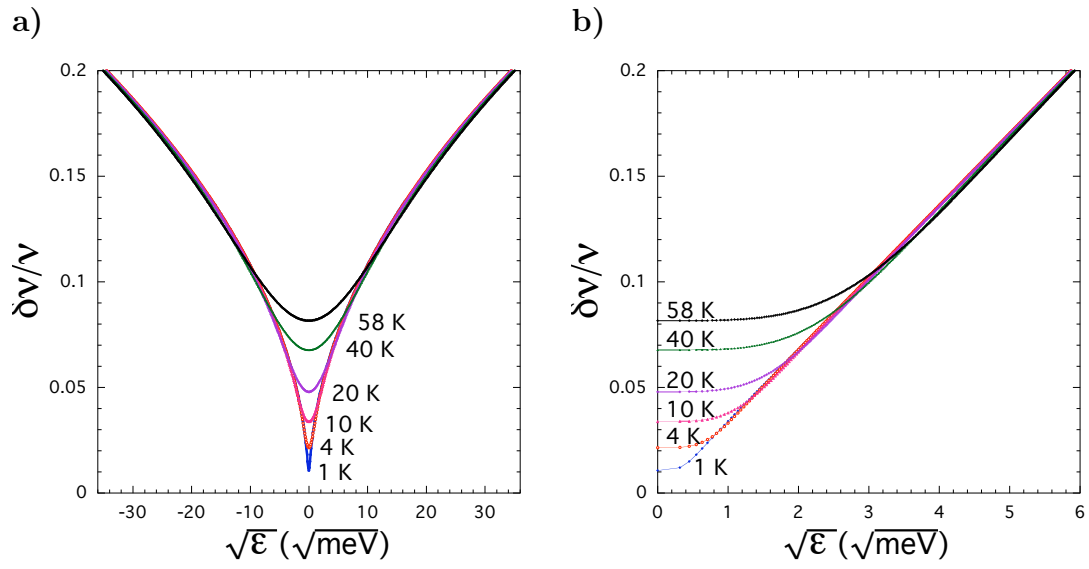

Figure 1.5. Abrikosov's Model $\frac{\delta\nu}{\nu}(\mathcal{E},T)$ Curves Calculated Using Equation 1.20 for Several Values of Temperature. Curves Plotted Versus a) Energy, and b) Square Root of Energy.

energy[8]. This is very well demonstrated in Figure 1.5, which displays model curves calculated using Eq. 1.20. The figure shows, that the range of the large deviation from $x \to \infty$ limit is localized around Fermi energy (zero of the horizontal axis). The deviation is due to finite temperature and the range $\sim \pm 1.6 k_B T$ is conveniently determined from either of the two plots. Part b) of the figure displays the model curves versus $\sqrt{|\mathcal{E}|}$. This type of display is the most efficient tool to identify regions of proportionality $\delta\nu/\nu_0 \propto \sqrt{|\mathcal{E}|}$ at $1.6 k_B T < \mathcal{E}$, which is where limit $x \to \infty$ gives very good approximation.

Let us recall Eq. 1.3 once more, which says that bulk conductivity is tied to the metallic DOS at the Fermi energy by formula $\sigma = e^2 \mathcal{D} \nu(\mathcal{E}_F)$. To evaluate the DOS correction at the Fermi energy we utilize Eq. 1.20 in the $\mathcal{E}/2k_B T \to 0$ limit,

[8]Corresponds to voltage regions of $\sim \pm 2.5 k_B T/e$ around zero-bias in electron tunneling spectra due to additional thermal smearing in the counterelectrode.

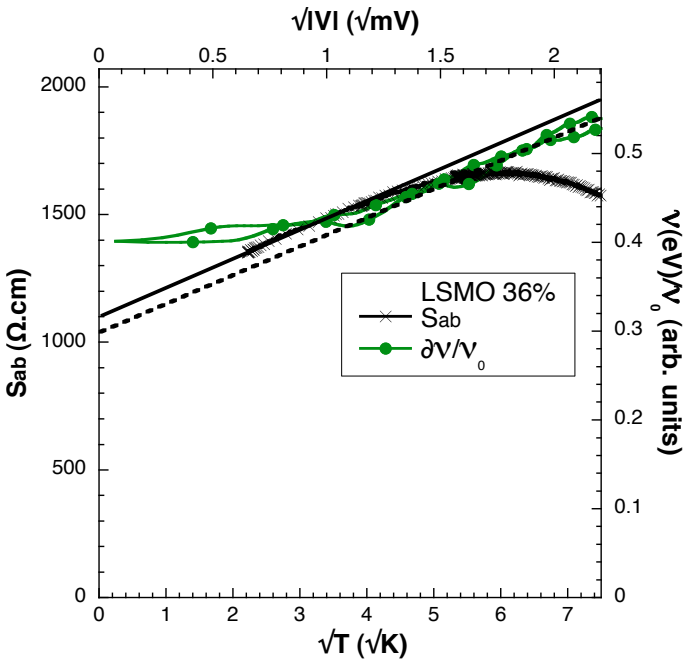

Figure 1.6. Matching the Bulk Conductivity $\sigma_{ab}(T) \propto \sqrt{T}$ and Normalized Tunneling Conductance $\nu/\nu_0(V) \propto \sqrt{V}$ Dependence. Note That Horizontal Scales Match via the $\sqrt{k_B/e}$ Ratio. Figure Discussed in Detail in the Text.

which is

$$\frac{\delta\nu}{\nu_0} = \frac{1}{\pi}\frac{\sqrt{\tau}\sqrt{k_B T}}{\sqrt{\hbar}(\frac{\mathcal{E}_F\tau}{\hbar})(\frac{\alpha\tau}{\hbar})} \quad , \tag{1.26}$$

This expression says that electron-electron interactions effect in the density of states in a quasi two-dimensional system has temperature dependence $\delta\nu/\nu_0 \propto \sqrt{T}$. In conductivity then a correction is implied that (assuming constant $\mathcal{D}$) has the same temperature dependence, $\delta\sigma(T)/\sigma_0 \propto \sqrt{T}$. This correction has been observed in bulk conductivity of LSMO 36% and 40% (both *ab*-plane and *c*-axis) and the proportionality holds up to ~ 50 K. This agreement between experiment and the above theoretical prediction identified the electron-electron interactions in LSMO.

We have gone one step further in identification of the $\sqrt{T}$ dependence of conductivity with the electron-electron interactions than the original publication of Okuda et al. [43]. In Figure 1.6 we publish bulk *ab*-plane conductivity $\sigma_{ab}(T)$ of

LSMO 36% as a function of $\sqrt{T}$ (black cross markers and line) and a normalized tunneling conductance ν/ν_0 as a function of $\sqrt{V}$ (green/grey circles and line). We show that when the square-root-energy scales are matched as one energy scale, as it has been done in the figure, the low-temperature parts of the dependences with effective $\sqrt{\text{Energy}}$ dependence very nearly match[9]. We used a solid line to highlight the $\sqrt{T}$-dependent part of the conductivity and a dashed line to highlight the $\sqrt{V}$-dependence of the normalized tunneling conductance. This can be interpreted as evidence that at a large majority the long-known effect in bulk conductivity is due to electron-electron correlations.

Physically, the connection between electron-electron interaction and diffusive motion of conduction electrons arises from the fact, that along the length of the effective radius of the screened Coulomb potential L_{e-e} the conduction electrons experience a number of elastic collisions. Equation 1.20 can be considered as a mathematical formulation of this relation and therefore it can be used, for example, to determine the elastic scattering time.

In the limit $\phi(\mathcal{E}/2k_BT) \rightarrow \sqrt{\mathcal{E}/k_BT}$, the Eq. 1.20 can be written as

$$\frac{\delta\nu}{\nu_0} = \frac{1}{\pi}\frac{\sqrt{\tau}\sqrt{\mathcal{E}}}{\sqrt{\hbar}(\frac{\mathcal{E}_F\tau}{\hbar})(\frac{\alpha\tau}{\hbar})} \quad , \tag{1.27}$$

where, as before, we chose to use parameters $\mathcal{E}_F\tau/\hbar = 2.93$ and $\alpha\tau/\hbar = 0.154$, which have been determined from a quantum interference experiment with LSMO 40%. We then can extract the elastic scattering time from Eq. 1.27. The total proportionality between the DOS correction and the elastic scattering time in Eq. 1.27 is $\delta\nu/\nu_0(\tau) \propto \tau^{-3/2}$, but as we use the quantum interference parameters, the effective

[9]Note that the smearing in the tunneling conductance is largely due to thermal smearing, but partly also due to numerical smoothing of the data during analysis.

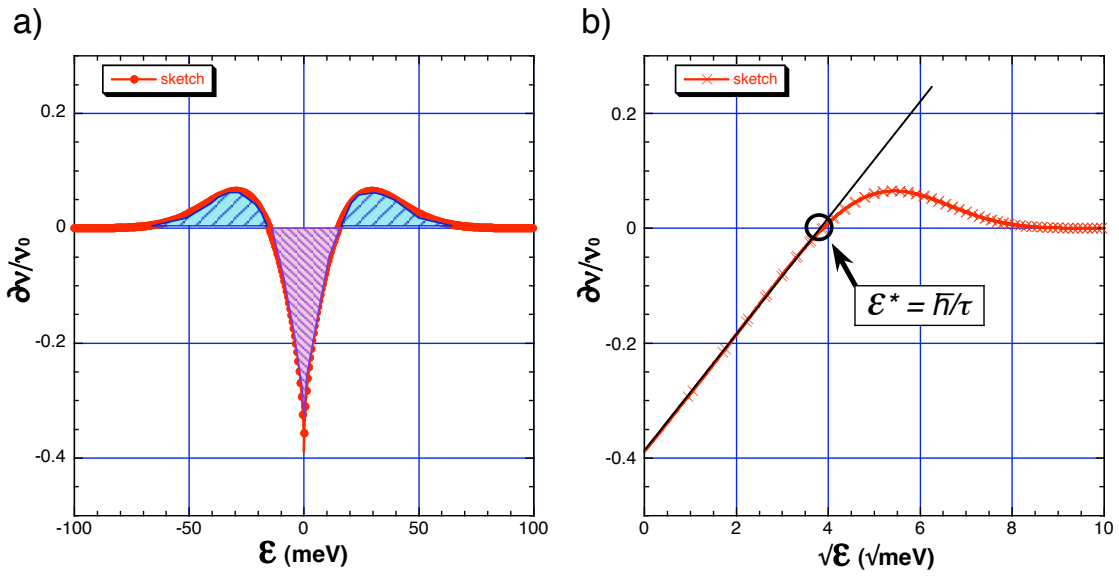

Figure 1.7. Artificial $\delta\nu(\mathcal{E})/\nu_0$ Curve to Illustrate the Conservation of States by the Electron-Electron Correlation Effect in 3D Metallic DOS in Large Energy Range. Curve Potted Versus a) Energy, and b) Square Root of Energy.

formula for elastic scattering time is

$$\tau = \hbar\left[\pi\left(\frac{\varepsilon_F\tau}{\hbar}\right)\left(\frac{\alpha\tau}{\hbar}\right)\right]^2\left(\frac{\frac{\delta\nu}{\nu_0}(\mathcal{E})}{\sqrt{\mathcal{E}}}\right)^2 = 1.327\ \text{eV}\cdot\text{fs}\times\left(\frac{\frac{\delta\nu}{\nu_0}(\mathcal{E})}{\sqrt{\mathcal{E}}}\right)^2 \quad . \tag{1.28}$$

In the right-hand expression, the remaining squared analytical term represents the slope of the DOS correction in the plot versus $\sqrt{|E|}$, as in Figure 1.5b. This slope should be expressed in the $\text{eV}^{-1/2}$ units.

In the outset of this section on the theory of electron-electron interaction we stated that the interactions are a state-conserving effect in the density of states. This means that the energies of states in quasimomentum phase space (q-states) near Fermi energy $\mathcal{E}_F$ are enhanced, i.e. electrons have higher energy while their quasimomentum does not change. However, due to a number of approximations, results of Al'tshuler's and Aronov's theory (as well as Abrikosov's theory above, naturally) only describe the shape of the DOS correction near Fermi energy. There is no theory currently in existence that gives a large-range state-conserving model of the DOS correction due

to interaction effects. In Figure 1.7 we present an artificial curve, a "cartoon", which has been constructed to possess the main features of the real-life electron-electron interactions' DOS correlation effect. The states conservation is best evaluated by comparison of the shaded areas in part a) of Figure 1.7 above and below $\delta\nu/\nu_0 = 0$ axis. Our sketched curve also has the $\propto \sqrt{|\mathcal{E}|}$ energy dependence near Fermi level, which is best observed in part b) of the figure in the $\delta\nu/\nu_0$ vs. $\sqrt{|\mathcal{E}|}$ plot, and it conserves states so that the states removed near Fermi energy are piled up at higher energies. The line added to this plot to stress out the extent of $\propto \sqrt{\mathcal{E}}$ proportionality is irrelevant in the sketched curve, which has no physical meaning, but it will become significant in the analysis of experimental data.

In the Figure 1.7 we observe that to conserve states the $\delta\nu/\nu(\mathcal{E})$ correction is negative near Fermi energy and so it must become positive at some higher energies. To describe this behavior analytically, based on available theory, we need to remove one approximation made in the derivation of Equations 1.24 and 1.20. According to Abrikosov's book (Ref. [2], page 219 of the first English edition), the relative electron-electron interaction correction to the DOS in three dimensions can be expressed as a time integral of probability of electrons' to be found in volume $(\mathcal{D}t)^{3/2}$ (once again we use the quasi two-dimensional way, $\mathcal{D}^{3/2} = \sqrt{\mathcal{D}_{ab}^2 \mathcal{D}_c}$) during their diffusive motion in a metal. Using this substitution, $\delta\nu/\nu(\mathcal{E})$ can be estimated as

$$\frac{\delta\nu}{\nu_0} \approx -\int_{\tau}^{\hbar/|\mathcal{E}|} dt \frac{v_F \lambda_F^2}{(\mathcal{D}t)^{3/2}} = \frac{2\sqrt{2}}{\lambda_\nu} \frac{\sqrt{\tau}}{\left(\frac{\mathcal{E}_F \tau}{\hbar}\right)\left(\frac{\alpha\tau}{\hbar}\right)} \left(\sqrt{\frac{|\mathcal{E}|}{\hbar}} - \frac{1}{\sqrt{\tau}}\right) \quad , \tag{1.29}$$

where λ_F is the wavelength of electron at Fermi energy, and $\lambda_\nu = 2d_0\nu_{03}/\nu_{02} = 2p_F d_0/\pi$ is a dimensionless parameter describing the crossover between two-dimensional and three-dimensional metals[10]. We can compare this result with the quasi two-dimensional one we derived from Al'tshuler's and Aronov's theory in Eq. 1.24 by

[10]Bare ν_{02} and ν_{03} can be recalled from Eq. 1.11.

writing down the $\mathcal{E}/k_BT \to \infty$ asymptotic solution

$$\frac{\delta\nu_3(\mathcal{E},T)}{\nu_{03}} = \frac{1}{2\pi}\frac{\sqrt{\tau}}{\left(\frac{\mathcal{E}_F\tau}{\hbar}\right)\left(\frac{\alpha\tau}{\hbar}\right)}\sqrt{\frac{\mathcal{E}}{\hbar}} \quad . \tag{1.30}$$

We can see that apart from the difference in the numerical pre-factor, Eq. 1.30 is an approximation of Eq. 1.29 assuming $1/\tau << |\mathcal{E}|/\hbar$. Because in Eq. 1.29 the DOS correction $\delta\nu/\nu(\mathcal{E})$ is zero at $1/\tau = |\mathcal{E}_{CO}|/\hbar$, this defines a characteristic energy scale for the DOS correction

$$\mathcal{E}_{CO} = \frac{\hbar}{\tau} \quad . \tag{1.31}$$

There is no hindrance in considering this energy scale $\mathcal{E}_{CO}$ a valid estimate for the quasi two-dimensional Abrikosov's solution in Eq. 1.27 as well. The energy scale definition in Eq. 1.31 only has a meaning, if the $\propto \sqrt{\mathcal{E}}$ character of the real DOS correction persists in the vicinity of $1/\tau = |\mathcal{E}|/\hbar$. As we show in the experimental results, this requirement is fairly well satisfied. With this we conclude our introduction to the theory of electron-electron interactions in metals. Theoretical aspects of measurements of the DOS correlation effect by electron tunneling spectroscopy are presented later, in Section 2.1.

1.6 Surface Phase of LSMO, x = 0.36 – 0.46

In 2005 Freeland et al. discovered non-ferromagnetic character of the first surface bi-layer of bulk-ferromagnetic LSMO 36% [18] at low temperatures. Similar character had been observed before on perovskite manganites (see Reference [44] for example), in surface layers about 5 nm thick. Whereas in perovskites ferromagnetic order builds up gradually with distance from the surface, in the bi-layered LSMO the magnetic character changes from fully non-FM to almost (about 98%) fully FM just as we cross from the first surface bi-layer to the nearest one below. This is illustrated by the graphics in Figure 1.8.

Point contact tunneling spectroscopy data were published in Freeland's article

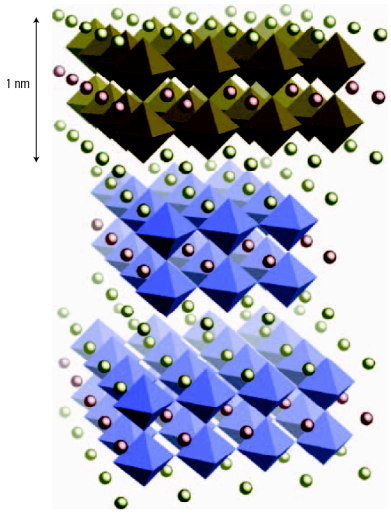

Figure 1.8. Illustration of the Non-Ferromagnetic, Insulating Surface Bi-Layer of LSMO 36%. Adopted from Reference [18] with Permission from Authors and the Publisher.

as well, which showed that there is a surface insulating phase on the LSMO 36% and that the thickness of the surface insulator corresponded to one insulating bi-layer. This was deduced by comparison of the point contact current-voltage characteristics with a calculated tunneling $I(V)$ through a rectangular potential barrier. We use the same procedure in Section 3.2 to evaluate several tunneling models and to estimate the areas of our point contact LSMO junctions.

Reason behind the insulating character of the LSMO surface is yet unknown, although several possible explanations are being currently examined. One reason may be the relaxation of unit cell dimensions due to the free boundary condition. It is well known that distortions of the cubic cell lift the valence band degeneracy further beyond the splitting illustrated in Figure 1.2, and it is possible for this process to disrupt the double-exchange mechanism or even introduce a hard insulating gap.

Other hypotheses consider the possibility of a change in surface chemistry. It has been shown before now that sputtered perovskite LSMO thin films exhibit

increased concentration of strontium in the surface[16]. There is a reasoning that a manganite's surface free energy can be minimized, when the crystal structure is finished by an electrically neutral plane. As the manganite structure is cubic, the surface two-dimensional lattice is a square one. This favors the divalent element oxide, strontium oxide in the case of LSMO, on the crystal surface. Whatever the force behind the chemistry change is, local change in the hole doping x can substantially change the electronic and magnetic ground state, as is clear from the phase diagram shown in Figure 1.3.

Of course, processes at the temperatures of thin film deposition (several hundred ^{o}C) can be quite different from what is happening on the surface of bi-layered LSMO during cleaving. Dulić et al. [16], for example, interpreted the strontium-rich surface phase of thin films using a structure geometrically different from the bulk perovskite. This can hardly be the case of surfaces obtained by cleaving of bulk bi-layered LSMO single crystals we study. However, changes in chemical composition in a rapid process immediately after cleaving (possibly fueled by the energy released from broken crystal bonds) can occur. We have decided to carry out an additional experiment using x-ray photoelectron spectroscopy on vacuum-cleaved bi-layered LSMO to examine surface chemistry. One experiment indeed showed the surface chemical composition from the bulk that could not be explained by extrinsic surface contamination or similar effect. The second, more detailed experiment, however, indicated no measurable composition variation in the range $6 - 24$ Å below surface. Data from both experiments are presented in Chapter 6. This project of surface chemical analysis is carried out in collaboration with the Department of Electronics and Vacuum Physics at Charles University in Prague, Czech Republic.

CHAPTER 2
ELECTRON TUNNELING SPECTROSCOPY

In this chapter we summarize the available results of the theory of electron tunneling between two metallic electrodes, outline the analysis of electron tunneling data necessary to extract the correlation effects in the density of states of the electrodes and, eventually, describe the mechanical and electronic hardware setup of our instrumentation.

2.1 Measurement of Correlation Effects in a Metallic Density of States

Large part of the original theoretical work on electron tunneling across an insulating layer between two metals is due to Frenkel [19], Holm and Kirchstein [24, 25] Bardeen [11], Harrison [23], Simmons [53, 54] and Stratton [55]. Their contributions were later processed by many authors into textbooks on the principles of electron tunneling spectroscopy. Expressions presented below were adopted from Wolf's book [59].

2.1.1 Rectangular Barrier Model of Tunneling Between Metals. When two electrodes with partially filled conduction bands are in close proximity, tunneling of electrons through the spacing between them becomes significant. This spacing is realized by vacuum (as in scanning tunneling microscope, STM) or by a thin insulating layer in mechanical contacts. The basic theory of tunneling assumes a planar tunneling junction. Assumption of a barrier homogeneous across junction area reduces the situation into a one-dimensional problem, which is illustrated in the diagram in Figure 2.1. In part a) of the figure we show a junction with a rectangular barrier defined by barrier height Φ above Fermi energy $\mathcal{E}_F$, and barrier thickness t_0. Part b) demonstrates, how the tunneling phenomenon is used in measurements of the density of states: at a finite bias there is a net current flow from left (tip, flat-band metal) electrode into the empty states in the right electrode (sample, correlated metal). The

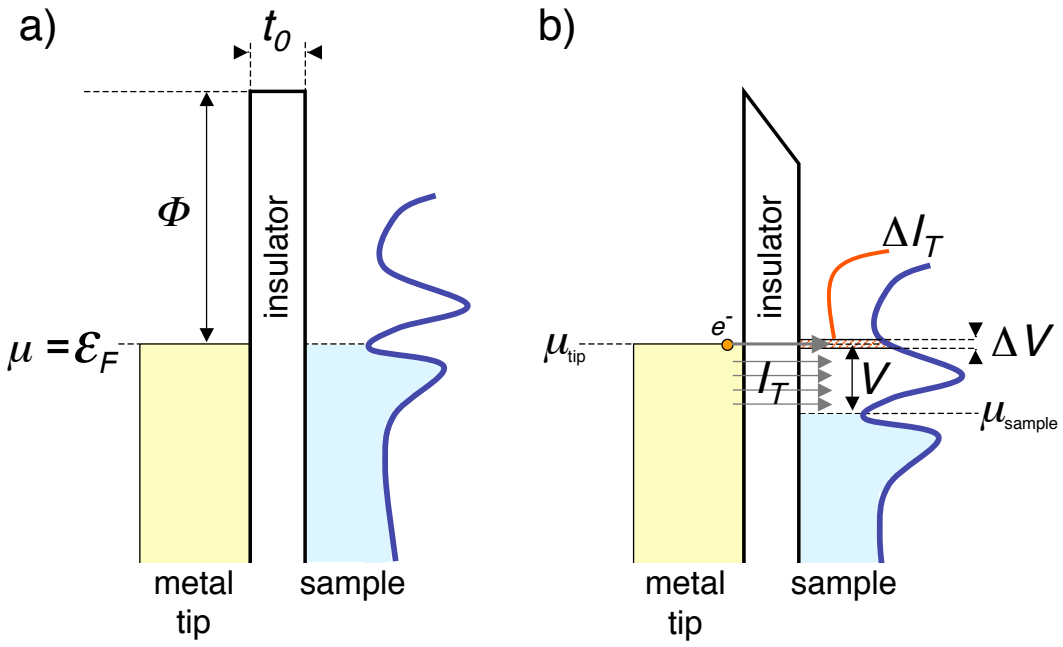

Figure 2.1. Diagram of a Tunneling Junction with a Simple Rectangular Barrier. This Diagram Illustrates a One-Dimensional Problem of a Tunneling Junction a) in Equilibrium, and b) at a Finite Voltage Bias.

total tunnel current I_T is proportional to the integral of the sample density of states (DOS) represented by the squiggly line on the right, in the limits from μ_{sample} to $\mu_{tip} = \mu_{sample} + eV$. In response to a differential increase of bias voltage by ΔV the tunnel current I_T increases by ΔI_T. Basic geometrical considerations show that in the infinitesimal limit, $\frac{\Delta I_T}{\Delta V} \rightarrow \frac{dI_T}{dV}$, proportional to sample DOS.

To develop theory of tunneling one starts with solving the Schrödinger equation and Hamiltonian appropriate for this system in stationary state. Resulting wavefunctions are then used in the quantum transport equation, from which the net current density through the junction can be derived in the form

$$J(V) = \frac{2e}{(2\pi)^3\hbar} \iiint \left[f(E) - f(E - eV)\right] D(E_x, V) \left(\frac{\partial E}{\partial k_x}\right) d^3k \quad , \tag{2.1}$$

where $f(E)$, $f(E-eV)$ are Fermi functions of their respective energies, k_x and E_x are the x-components of the wavevector and energy of electrons, respectively, $D(E_x, V)$

is the barrier transmission coefficient, and $(1/\hbar)(\partial E/\partial k_x)$is the group velocity of conduction electrons along the tunneling direction. The barrier transmission coefficient D has the form

$$D(V, E_x) = g\ exp\left(-2\ \int_{x_1}^{x_2} \sqrt{\frac{2m}{\hbar^2}\left[U(V,x) - E_x\right]}dx\right) \quad , \tag{2.2}$$

where, x_1 and x_2 are the coordinates of the barrier's classical turning points at energy E_x and voltage V, $U(V,x)$ is the barrier profile, and g is a prefactor[11], which we assume equal to unity, $g = 1$, throughout this thesis.

In the zero-temperature approximation, the three-dimensional integration in Eq. 2.5 can be separated into parts parallel with tunneling direction $\hat{x}$ and perpendicular to this direction (i.e. lying in the $\hat{y}\hat{z}$ plane). The integration in the $\hat{y}\hat{z}$ plane can be carried out analytically[12]. The resulting formula was

$$J(V) = \frac{em_t}{\pi\hbar^2}\left[eV\int_{\mu}^{-eV} D(E_x, V)dE_x - \int_{-eV}^{0} D(E_x, V)E_x dE_x\right] \quad , \tag{2.3}$$

where m_t is the effective mass in the $\hat{y}\hat{z}$ plane, E_x is the energy corresponding to the momentum in $\hat{x}$ direction k_x, measured from Fermi level, and μ represents the Fermi level energy measured from the bottom of conduction band. Because the left-hand integral converges fast with rising μ, it is customary to choose an arbitrary large number for μ in numerical calculations.

The coefficient D is known to have a far more complicated form in real barriers, which would be better represented by a tunneling matrix with nontrivial dependence on k_y and k_z. As the research presented here is only the second consistent tunneling work on the bi-layered LSMO, which uses the intrinsic surface insulator as the

[11]Harrison [23] derived g exactly and it is in the order of unity in the usual Werner-Kramer-Brillouin (WKB) approximation. The WKB approximation in this context means that $U(V,x)$ is "slowly varying" in the vicinity of points x_1 and x_2.

[12]This was done by Holm and Kirchstein [24, 25].

tunneling barrier, our understanding is not advanced enough to go beyond the one-dimensional model. We can expect that the analysis gets refined in this respect in future, as it happened in tunneling into high-temperature superconductors (i.e. nodal preferential tunneling).

2.1.2 Analysis of Electron Tunneling Spectra. The three equations above form the theory of electron tunneling between two metals with flat conduction bands, i.e. metals with $d\nu/d\mathcal{E}(\mathcal{E} \approx \mathcal{E}_F) = 0$. This condition holds very well in ordinary metals, such as gold, copper, silver, etc. However, the strength of tunneling spectroscopy is that for the DOS in the electrodes it can measure *deviations* from the flat-band model caused by *correlations* of conduction electrons. One well known example of effects causing such DOS correlation effect is superconductivity, which gives rise to tunneling spectra with characteristic gap around zero bias and quasiparticle peaks. Superconductivity is a result (proven in classical superconductors, very likely in HTS) of coupling of conducting electrons to a boson. At sufficiently low temperatures, this interaction causes large deviation from the nearly-free electron model of metals by Sommerfend.

In Chapter 1 we presented an overview of Sommerfeld theory of metals, which is based on the assumption of non-interacting conduction electrons. In this model, motion of electrons is diffusive and ruled by impurity scattering. One electronic correlation that exists in all metals, is the Coulomb interaction between conduction electrons themselves. Due to screening of the Coulomb potential and a long elastic mean free path $\bar{l}$ of the electron diffusion the effect in ordinary metals is negligible. However, in disordered metals (e.g. ones with large concentration of impurities) the Coulomb interaction can have a substantial effect, for which the theory is presented in Section 1.5. In the theory we showed that the interaction redistributes electron k-states on the energy scale without creation nor annihilations - the interac-

tion conserves states.Effects of this interaction on the metallic DOS has been observed rarely, because it is negligible for all materials except those with extremely short mean free path. LSMO is, however, material with such short mean free path ($\lambda = 1.44$ nm in LSMO 40%, see Ref. [34]). The principal purpose of our tunneling experiments was to reveal, if a there is a measurable effect in the density of states and if it corresponds to electron-electron interactions.

Regardless of the origin of the interaction nature, let us assume that it causes a deviation $\delta\nu/\nu_0(\mathcal{E})$ from the interaction-free model, so that the total correlated DOS of the sample is

$$\frac{\nu}{\nu_0}(\mathcal{E}) = \frac{\nu_0 + \delta\nu(\mathcal{E})}{\nu_0} \quad . \tag{2.4}$$

As before, ν_0 stands for the virtual DOS in the vicinity of Fermi energy *without interactions*. Let us then consider tunneling through a junction between this *correlated* material (sample) and a flat-band, uncorrelated metal electrode (tip), with a thin insulating barrier in between. The voltage dependence of the tunneling current $I(V)$ will be

$$I(V) = c \int \frac{\nu}{\nu_0}(\mathcal{E} + eV)\,[f(\mathcal{E}) - f(\mathcal{E} + eV)]\,D(V, \mathcal{E})\; d\mathcal{E} \quad , \tag{2.5}$$

where all details of the junction, the area, the tunneling barrier and the tunneling mode (momentum-conserving or non-conserving, inelastic tunneling channels, etc.), are contained predominantly in the transmission coefficient $D(V, \mathcal{E})$. This equation is implicit in $\delta\nu/\nu_0(\mathcal{E})$, and extraction of the correlation effect analytically is only possible in the zero-temperature limit, when also $D(V, \mathcal{E})$ is approximately constant in voltage. In such limit the DOS deviation can be obtained as

$$\frac{\nu}{\nu_0}(\mathcal{E}) \doteq \tilde{c}\; \frac{dI}{dV}(eV) \quad , \tag{2.6}$$

where the energy scale $\mathcal{E}$ of the DOS deviation is provided by the bias potential energy eV.

The rigorous approach to the analysis of tunneling data at finite temperatures is to implement a sensible model for $D(V, E)$ and the DOS correlation effect $\delta\nu/\nu(\mathcal{E})$, calculate the integral in Eq. 2.3 and iteratively fit the $I(V)$ or $dI/dV(V)$ tunneling data. In case of the Coulomb interaction, theoretical predictions have been made only in the limits of perturbation analysis and they do not obey the conservation of states rule. Therefore, no physically meaningful model of the DOS correlation effect could be implemented.

Fortunately, we were able to verify in a detailed manner that the tunneling characteristics can be, at a large scale of voltages $100 - 1000$ meV, fit with the coherent tunneling model given by Eq. 2.3 (we demonstrate this in Section 3.2) and that the tunnel current can at intermediate voltages well approximated by an odd-power third-order polynomial. This polynomial predominantly reflects the change in tunnel current due to change of the barrier shape under voltage bias. Therefore, it could be used to analyze the correlation effect in the voltage range $-100..+100$ mV.

We use an approximate expression for the DOS deviation, essentially identical to the zero-temperature expression

$$\frac{\nu}{\nu_0}(\mathcal{E}) \doteq \frac{\frac{d}{dV}I^{exp}(V)}{\frac{d}{dV}I^{fit}(V)} \quad , \tag{2.7}$$

where the $\frac{d}{dV}I^{exp}(eV)$ is the experimental conductance, and $\frac{d}{dV}I^{fit}(eV)$ is the fitted model conductance curve. We use two alternative expressions of $I^{fit}(V)$ to fit the data $I^{exp}(V)$ (the superscript is omitted in the reference to experimental characteristics throughout most of the thesis). As the effect of thermal smearing is localized to energies $|eV| \lesssim \pm k_B T$, we can consider the data at higher energies as satisfying Eq. 2.7 almost exactly[13]. When value $\frac{\delta\nu}{\nu}(\mathcal{E} = 0, T = 0)$ is needed for the analysis,

[13]The temperature dependence in Abrikosov's expression for $\frac{\delta\nu(\mathcal{E})}{\nu(\mathcal{E})}$, Eq. 1.20, which goes as $f(E + eV) - f(E - eV)$, so that the range of observed thermal smearing effect in the data is approximately equal to $\sim 2k_B T$, see Subsection 3.1.2.

we can determine it with reasonable precision by extrapolation of the higher-energy data to $eV = 0$.

As mentioned above, $|V| << \Phi/e$, the model tunneling characteristics given by Eq. 2.3 can be approximated with an expansion odd in voltage, such as

$$I(V) = aV + bV^3 \quad , \tag{2.8}$$

where symbol a has the meaning of the free-electron model zero-bias conductance. Henceforth, this expression is refered to as the *elastic expansion*. Simmons [53] approximated Eq. 2.3 in the case of high tunneling barrier $\Phi >> \max(|V|)$ with another analytic formula and showed that the expansion coefficients a and b of Eq. 2.8 are tied to barrier parameters Φ and t_0 by expressions we added to this thesis in Appendix C. We tested his approximate expression with Eq. 2.3 and we found that the unsatisfied assumption of $|V| << \Phi/e$ (the voltage range we used was $100 - 230$ mV, while $\Phi/e \sim 300$ mV) lead to systematic errors in the resulting parameters Φ and t_0.

While fitting the experimental data with numerically calculated curves according to Eq. 2.3, we observed that fits are significantly improved over the whole range $100 - 1000$ mV by adding a term $\propto V|V|$, which has been suggested by Kirtley et al. as a suitable treatment of inelastic tunneling channels [28]. Although there are limitations to this approach both in the low-bias and high-bias part of the tunneling characteristics, the addition of a term proportional to $V|V|$ seems to be correct at the intermediate voltages $100 - 230$ mV (explained in this section below), which we used for fitting. For these reasons we also used an expression, which included the inelastic tunneling term in the form

$$I(V) = aV + bV^3 + cV|V| \quad . \tag{2.9}$$

This expression is referred to as the *inelastic expansion* in this thesis.

In order to determine, what voltage range is optimal for fitting the tunneling

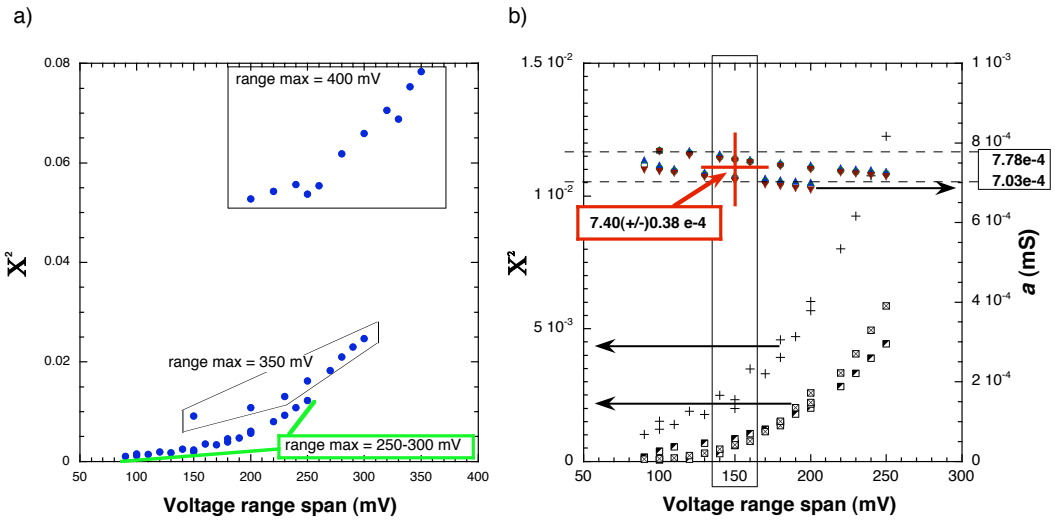

Figure 2.2. Illustration of the Procedure Carried Out to Determine the Optimal Voltage Range for the Expansion Fits to the Tunneling Background. Several Series of Fits were Performed on a Few Datasets and χ^2 Optimization Was. Details of the Figure Are Discussed in the Text.

characteristics (from the point of view of the correlation effect in the DOS this fitting procedure is, effectively, an *estimate of tunneling background*, or simply "background fitting"), we ran a series of tests on several data files, and also on the numerically calculated model curves from Eq. 2.3. Tests with the model curves only determined that the higher limit of the fit range ought to be below Φ/e, which was an expected result. In second step we ran the elastic expansion fits on experimental data, choosing a variety of fitting ranges below 300 mV, while observing the variation of χ^2. The resulting values of χ^2 (not normalized to the number of fitted data points) obtained on one particular expermental $I(V)$ were displayed in Figure 2.2 plotted versus the size of the voltage range. In part a) we can observe that the choices of fit range maxima 200 mV and 250 mV resulted in consistent, overlapping datasets of χ^2, while choices 300 mV and 350 mV gave much larger errors. This verifies the conclusion based on tests run on model curves.

In Figure 2.2b, the χ^2 scale is expanded and the values of parameter a representing the zero-bias conductance were plotted on a second vertical axis. The χ^2 values could be approximated with a line upto approximately 150 mV rfit range span, beyond which they rise observably faster. We concluded that the fit range span ought to be ≤ 150 mV, while the range maximum is below 250 mV. There wa an additional hint, as we observed that the data tended to depart from the fits below $70-110$ mV, when elastic expansion had been used, and $50-80$ mV after using the inelastic expansion. Based on these observations we decide to adopt the range $100-230$ mV as the optimal for carrying out the expansion fits from Equations 2.8 and 2.9.

It ought to be added that the zero-bias conductance values, as shown in Figure 2.2b, vary by only $\sim 5\%$ with variation of fit ranges, which spanned $100-150$ mV with maxima less than or equal to 250 mV. In the analysis leading to Figure 2.2, the elastic expansion (Eq. 2.8) was carried out on $I(V)$ data with observable asymmetry and parameters χ^2 and a of the two polarities were plotted in Figure 2.2 separately. For every voltage range span, the a values were found within 10% from each other. The uncertainty of the a in each polarity alone was less (the above-mentioned 5%), as the fit range span varied. Therefore, we consider the fits reliable enough to allow further analysis of the DOS correlation characteristics (the scattering time determination in Section 3.3) after normalization using fits in the $100-230$ mV range. Finally, the analyzed data were measured at temperature 4.2 K. This accounts for a smearing $k_BT/e \sim 0.35$ mV of the spectra. As the DOS correlation effect alone is smeared by temperature in the voltage range $|V| \lesssim 1.6k_BT/e$, the expected total thermal smearing of the tunneling spectra was $\sim 2.6k_BT/e \approx 0.9$ mV and it agreed with the amount of thermal smearing actually observed.

2.2 Point Contact Tunneling Instrumentation

Most of the experimental work presented in this thesis has been carried out

using point-contact spectroscopy. With this technique, junctions are created by pressing a metal tip against the sample surface. Combination of sample material and tip determines the types of junctions that can be created. In majority of tunneling junctions made on LSMO we used mechanically sharpened gold tips. Many materials, including high-T_c superconductors and bi-layered LSMO of certain doping levels, feature an intrinsic insulating layer on their surface. A small area contact between the gold tip and the sample can, therefore, satisfy the tunneling spectroscopy assumption of existence of a well-defined, uniform insulating barrier between two metallic electrodes. In such cases, equations 2.6 and 2.7 are valid to reveal the details of the sample electronic density of states.

In our experiments with bi-layered LSMO 36% single crystals at temteratures below insulator-to-metal transition point, $T < T_c$, the insulating tunneling barrier was represented by a single surface bi-layer. This was the conclusion of previous PCT experiments by Özyüzer presented in [18], and we verify, confirm and refine this model in Sections 2.1 and 3.2. We also use the model to calibrate the otherwise unknown areas of our point contact junctions.

The point contact instrument used in the experiments had been made by Dr. Özyüzer and described in detail in [47] and [45]. No changes in functionality of the mechanical setup have been inflicted upon the aparatus since then and, therefore, this shall be only briefly described. The electronics setup has been used in several variations, all of which were quite straighforward. They will be listed and briefly described.

2.2.1 Mechanical Hardware Setup. The mechanical hardware consists of two major components: the Dewar can with cryostat and a superconducting electromagnet, which allows variable-temperature and variabe magnetic field conditions, and the insert through which we realize motion transfer to the tip to create adjustable point contact junctions and electrical connections to all active parts, as shown in

Figure 2.3a[14] To allow stable functionality in high magnetic field, the key parts of the insert had been designed using non-magnetic materials (titanium, copper). In addition, the insert accommodates a Cernox temperature sensor selected for its small magnetoresistance across the temperature range.

The Dewar can with a continuous flow cryostat was manufactured by Janis Research Co. It allows the control of temperature between 1.5 K and room temperature by (I) varying the flow rate of cryogen (liquid He or liquid N_2) from reservoir to sample space by means of a needle valve, (II) varying the electrical heating of the cryogen by a vaporizer, (III) by varying the rate of pumping of the sample chamber using a valve on the pumping line, and (IV) by varying the electrical power through a heating element optionally placed below the sample, on top of the sample holder. Temperature sensors are placed at the vaporizer and in the sample holder for monitoring of the thermal state of the system. The vaporizer temperature sensor and heater are connected to one LakeShore 91C temperature controller, which provides a feedback loop for an automatic temperature control. Another LakeShore 91C temperature controller monitors the temperature sensor located at the sample holder, while the adjacent heating element is operated manually using a standalone Kepco d.c. voltage/current source. The maximum achievable temperature stability is 0.01 K.

The cryogen reservoir of the system contains a superconducting solenoid located around the lower end of the sample space, co-axially. It can supply vertical magnetic fields of induction $B_0 = 0 - 6$ T, with typical stability approx. 1 mT. In our measurements involving variable magnetic field we used LakeShore magnet power supply, model 622, to power the magnet.

---

[14]Both parts of the Figure 2.3 were reprinted from [47]: Cryogenics 38.9, L. Ozyuzer, J.F. Zasadzinski and K.E. Gray, *"Point Contact Tunneling Apparatus with Temperature and Magnetic Field Control"*, pp. 911 − 915. Copyright (1998), with permission from Elsevier.

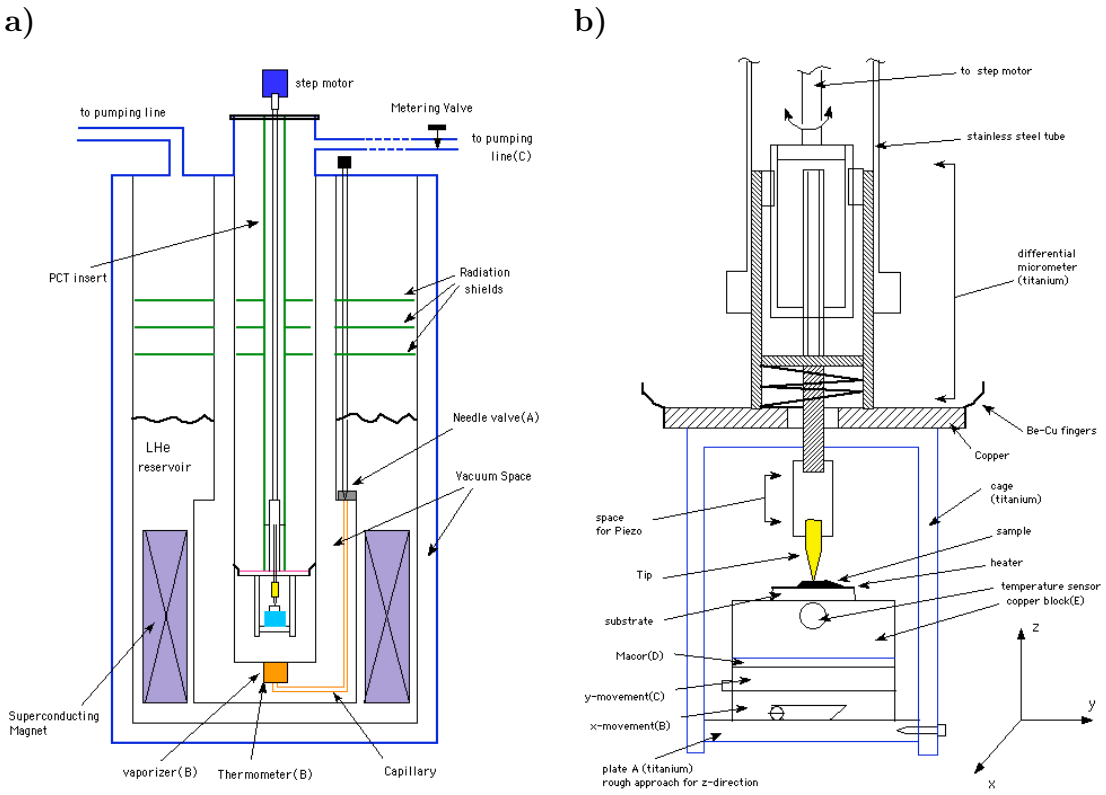

Figure 2.3. Schematic Representation of the Mechanical Setup with Details Described in Text. a) Dewar Can with Cryostat and Insert. b) Detail of the Bottom Part of the Insert. Reprinted from [46], with Permission from the Authors and the Publisher.

The point-contact insert consists of a thin-walled stainless tube, which carries the measuring PCT head and all the necessary mechanical and electrical connection of the PCT head to the outside of the sample space. The PCT head is depicted in 2.3b. It consists of a titanium cage, which houses a multi-component sample holder, and a titanum differential micrometer, which is used to control the vertical position of the tip. This differential micrometer has a compound pitch of 11.5 nm per degree of revolution over a total travel range of 0.4 mm (about 100 full turns). The sample holder carries the Cernox temperature sensor, sample on a substrate, and the optional heating element (an SR-4 strain gauge). It contains two horizontal positioners for alignment of the sample with the tip before every experiment. The usual initial distance between the tip and sample set before an experiment is set manually to a value anywhere within 0.2 mm, i.e. well within the above-mentioned 0.4 mm range of the differential micrometer. The tips are always mechanically sharpened and chemically cleaned before use. It is usually desirable that the tip does not touch the sample before the first junction is created under controlled conditions within the cryostat and this rule has been followed in all experiments presented here.

Mechanical stability of the junctions is determined mainly by the rigid design of the measurement head, which has eigenfrequencies in the high acoustic range. To prevent these acoustic frequencies from getting to the junctions, the Dewar can is immersed in a drum filed with silica sand and the whole is suspended on three air suspension legs. All wires and pumping-line hose are fed through another sand-filled box, which further reduces the influence of the external mechanical noise.

2.2.2 Sample Mounting. Samples of bi-layered LSMO were all cleaved shortly before the experiment, because the surfaces of this compound are known to slowly degrade (loose oxygen) on the time scale of days. A freshly cleaved crystal is glued to an alumina substrate using the Hardmann fast-curing epoxy or the TorrSeal vacuum-

compatible epoxy. Electrical connections are then made using gold wires affixed to the crystals with a conductive silver paint. We consider these electrical contacts acceptable for measurement, when the two-terminal resistance across the sample with leads is below 50 Ω, which is much lower than typical minimum resistance (approx. 1 kΩ range) of the measured tunnel junctions.

2.2.3 Electronic Hardware Setup. The point contact tunnel junctions on LSMO generally had a rather low tunneling barrier height, $\Phi \sim 300 - 400$ meV. As the existence and basic properties of this intrinsic surface barrier has not been firmly established to date, our measurements included measurement of current-voltage characteristics both above and below the voltage corresponding to the tunneling barrier height. Because the differential conductance varied between zero bias and 1 V (roughly the maximum bias applied, with some exceptions) by ~ 4 orders of magnitude, we had to arrange the electronic instrumentation so that satisfactory precision of measurements was achieved in both extremes and between them. It is a situation as challenging as the measurements of tunneling spectra of superconductors, where the conductance extremes (quasiparticle peak height and gap conductance minimum) may differ in a similar order. Moreover, while spectroscopy of superconductors rarely focuses on the detailed structure of the high-resistance part of the curve near zero bias, this is the region of interest in our spectroscopy investigation of LSMO.

The measurement of $I(V)$ is straightforward in essence and the block diagram of electronic connections is presented in Figure 2.4. We supply voltage sweeps (mHz-frequency triangular waveforms) either from a battery-powered homemade sweep circuit or from an HP waveform generator. Both current and voltage are invariably monitored using Stanford Research Systems (SRS) voltage differential amplifiers SR560, while current is measured as a voltage across a known resistor (selector with 1 Ω to 10 MΩ resistors is used, with steps of one order of magnitude). There have been two

distinctly different ways, in which the signals from the preamplifiers' single-ended outputs were digitized. In the first case, the signals were fed into front-side inputs of Keithley 2001 multimeters. The multimeters carried out the A/D conversion and output the values through the GPIB interface. A Macintosh G4 PowerPC computer equipped with National Instruments' (NI) PCI-to-GPIB card was used to read the data and store them in spreadsheet files. In an alternative setup (described in detail in [51]) a high-speed NI BNC-to-SCSI board replaces the two Keithley multimeters to digitize the data. The computer then uses NI PCI-to-SCSI board to collect the data. In both cases the programs operating the data acquisition process are written in NI LabVIEW graphical programming language. Additional controllers and power supplies have been used to measure and control the temperature and magnetic field. These are not displayed in Figure 2.4, because their connection to heaters, sensors and magnet coil are trivial, they were usually not part of the GPIB data-acquisition ring, and they were always operated manually using their front-panel interface.

Differential conductance dI/dV data analyzed in the following chapters were obtained as numerical derivatives of $I(V)$ data, or were measured by a lock-in technique. We used SRS dual-phase lock-in amplifier SR830 with a differential preamplifier SR550 in the arrangement shown in fig:exm. The lock-in amplifier was used as source of a sine waveform. This A.C. signal was de-coupled from chassis ground using a Gertsch shielded 1:1 transformer and then added to the low-frequency triangular waveform (D.C. voltage sweeps) using a low-noise operational amplifier. The resulting voltage was then applied across the junction. The voltage measurement line was then forked: one branch was connected to the SR560 preamplifier as in $I(V)$ measurement, the other branch connected to the SR550 preamplifier, from where the signal continued (still double-ended) to the lock-in preamplifier. In the lock-in measurement, the output signal is proportional to the intensity of the Fourier transform of the signal coming from the junction, measured at a selected harmonics (the 1st

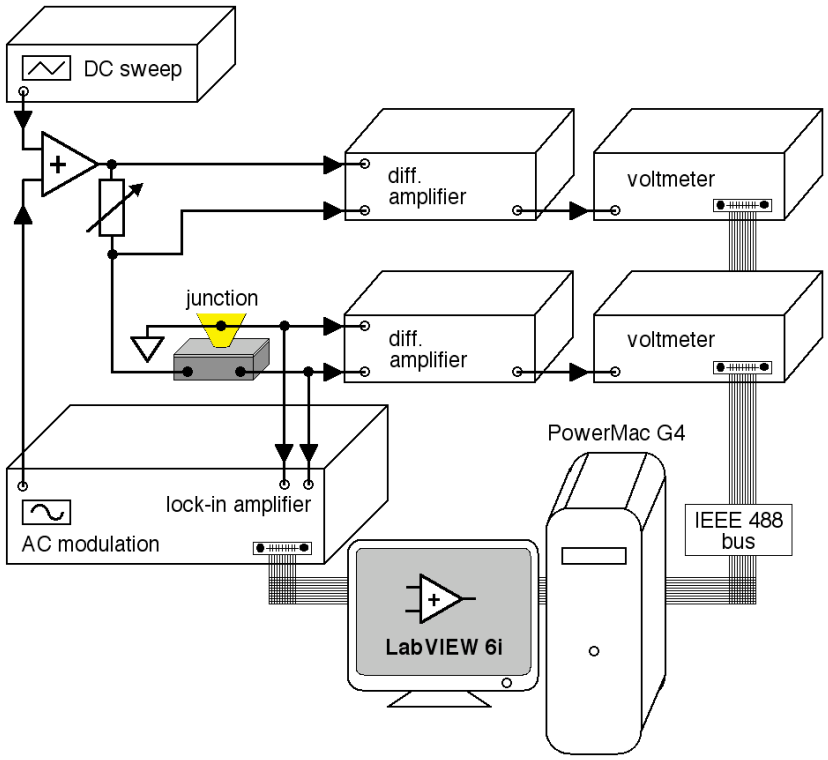

Figure 2.4. Electronic Hardware Configuration Diagram of the Data Acquisition Ring Used in the Point-Contact Electron Tunneling Spectroscopy Experiments. Details Described in the Text.

harmonics for measurements of the 1st derivative) of the frequency of the input sine A.C. signal.

If the A.C. modulation source was an ideal current source, the inverse of the lock-in output would be proportional to $dI/dV(V)$. In our case the signal needs to be calibrated with respect to the numerical derivative of $I(V)$. The relation between the inverse lock-in signal and the numerical derivative is usually linear, with a small quadratic correction. This calibration provides real conductance units to the lock-in data and gives a feedback regarding artifacts of the lock-in technique that may appear in the data. Tunneling data presented below were verified to not contain lock-in artifacts, or else the possible artifacts are pointed out where appropriate.

CHAPTER 3

TUNNELING SPECTROSCOPY OF LSMO 36%

Electron tunneling spectroscopy theory in $T = 0$ K approximation, Eq. 2.6, predicts that tunneling dynamical conductance $dI/dV(V)$ is proportional to the correlation effects in the electronic density of states of materials in the junction. We used this in successful measurements of the superconducting features in the DOS of the high-temperature superconductor $Tl_2Ba_2CaCu_2O_8$ and of an anisotropic low-temperature superconductor CaC_6. Results of the experiments are expected to be published in Physical Review B [39] and Physical Review Letters [30], respectively.

In this chapter we present our discovery of the electron-electron interaction effect in the density of states of the bi-layered LSMO 36%. Our results presented in this chapter are being prepared for publication in Physical Review Letters [40] In the first section, we identify the corresponding feature in the tunneling spectra and present evidence for our interpretation of the data as the DOS correlation effect. Then our task is to analyze the data in detail, using Abrikosov's theory presented in Section 1.5. A correct separation of the DOS effect from the tunneling background[15] is crucial for the analysis, and it is especially challenging due to the low height of the tunnel barrier. Section 3.2 is therefore dedicated to the procedure, through which we determined the actual tunneling background. The fits are then used to normalize the conductance spectra in order to obtain the correlated DOS $\nu(eV)/\nu_0$.

In Section 3.3 we show that the normalized tunneling conductance spectra conserve states. We derive the characteristic energy range of the correlation effect and present the elastic scattering time τ estimates derived from normalized conduc-

[15]By "tunneling background" we always mean the tunneling characteristics of the real tunnel barrier, which would be measured, if both electrodes had uncorrelated DOS at Fermi energy.

tance spectra of a number of junctions. The resulting values are cross-examined for consistency and discussed in relation to parameters of the bi-layered LSMO obtained from the data of others, namely the ARPES data published recently by Mannella et al. [36] and Sun et al. [56].

Like most experimental techniques, the point contact tunneling may produce data containing artifacts, which mask the density-of-states effects and lead to misinterpretation of the tunneling spectra. Discussion of several alternative interpretations of the data we measured is presented separately, in Chapter 4. Eventually, we were able to use the models of tunneling background to make improved estimates of point-contact junctions' areas. This project is presented in Chapter 5, which concludes the electron tunneling part of the thesis.

3.1 Identification of a Correlation Effect in LSMO

We carried our point-contact tunneling spectroscopy measurements of bi-layered LSMO 36% single crystals. We consistently observed a cusp-like zero-bias anomaly in the tunneling conductance characteristics, as shown in Figure 3.1a). The displayed characteristics belong to junctions with zero-bias conductance varying across 2 orders of magnitude $10^{-1} - 10^{1}$ μS and, therefore, have been scaled and offset for the presentation. The cusp-like shape of the zero-bias anomaly corresponds to the $\sqrt{\mathcal{E}}$ dependence of the electron-electron interactions in the three-dimensional and quasi two-dimensional metallic density of states.

Point-contact junctions on bi-layered LSMO are tunneling junctions, as discovered by Freeland et al., and so the characteristics are at low bias voltages approximately proportional to the correlation effect in DOS. Theory of Al'tshuler and Aronov, as well as Abrikosov's extension to quasi-two-dimensional metals, predict proportionality $\frac{\delta\nu}{\nu_0}(E = eV) \propto \sqrt{|eV|}$ near Fermi energy (i.e. near zero bias in tun-

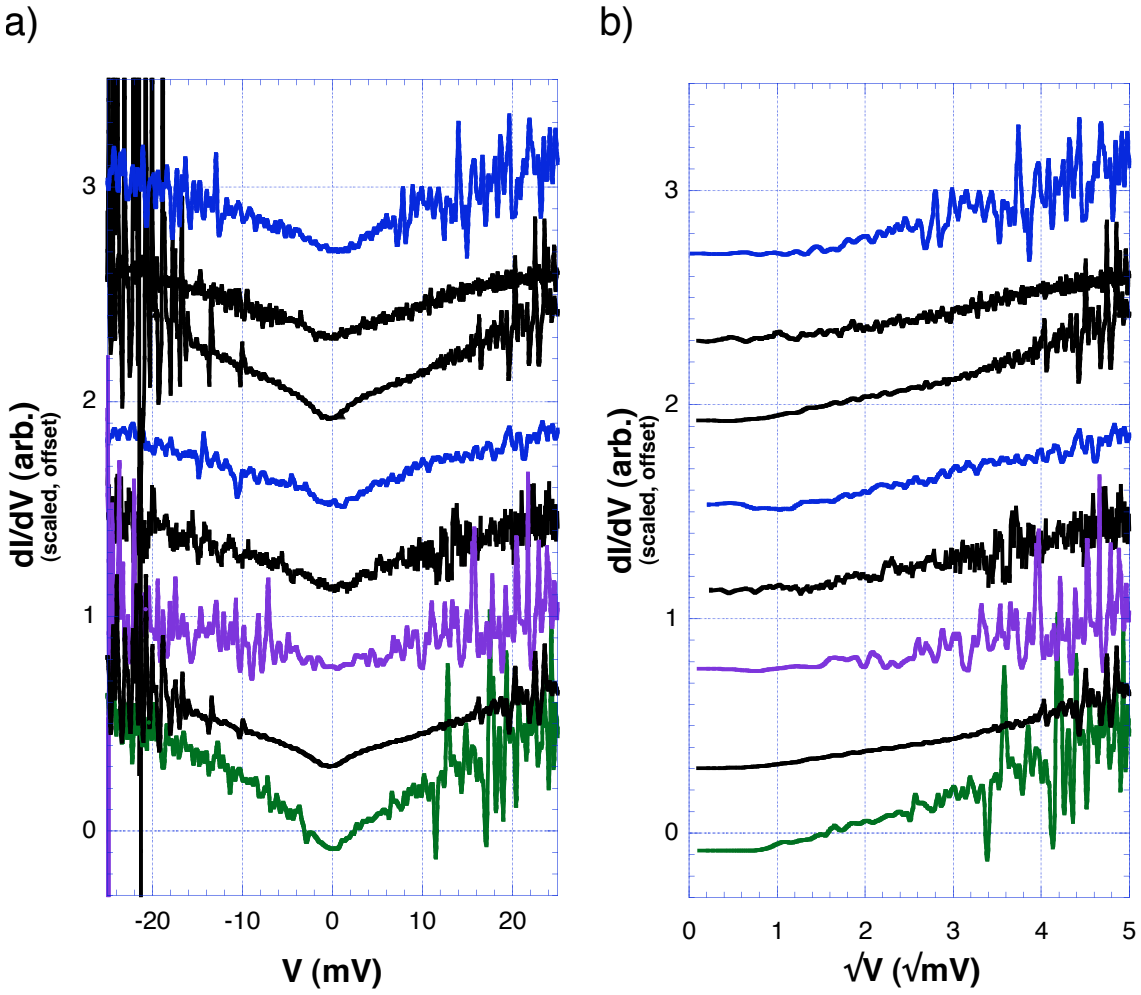

Figure 3.1. Overview of the Correlation Effect in the Raw Low-Bias Tunneling Conductances. For an Easier Identification of the $\sqrt{\mathcal{E}}$ Dependence the Datasets Are Plotted Versus a) Voltage, and b) Square-Root-Voltage.

neling spectra). In order to examine this proportionality of the presented tunneling data, the conductance characteristics from Figure 3.1a) are presented in part b) of the figure versus $\sqrt{V}$. In part b) only positive-bias branches of datasets from part a) were displayed. There is a reproducible region $\sim 0.8 - 3.5\ \sqrt{\mathrm{mV}}$, where the plots can be, with very good precision, approximated with straight lines. This agreement with the theoretical square-root dependence and the high reproducibility of the feature over a range of junction resistances are strong indicators that the effect is indeed a DOS correlation effect, not an artifact. Below, we show some temperature dependence and magnetic-field dependence, which are consistent with the electron-electron interaction predictions.

3.1.1 Magnetic Field Dependence. Magnetic field dependence of point contact junctions on LSMO 36% was measured at $T = 4.2$ K in fields up to $\mu_0 H = 6$ T. No changes were observed beyond the noise contribution, hence only $dI/dV(V)$ curves measured at 0.05 T and at 6 T are shown in Figure 3.2. Solid black circles represent the low-field measurement, whereas the solid grey triangles represent the high-field data. Due to junctions instability and loss in rising magnetic field [16], presented curves correspond to different junctions. For the purpose of the display, plots in Figure 3.2 were scaled and offset. Part b) of the figure shows the same characteristics plotted against $\sqrt{V}$, so that we could evaluate any change in the $\sqrt{V}$ proportionality. The solid black lines laid over the data remain parallel between the two datasets, within error bars given by the noise. It can be concluded that in the range of magnetic fields $0.05 - 6$ T, the effect of magnetic field on the studied low-bias feature in the tunneling $dI/dV(V)$ characteristics is negligible. It is important to mention that this does not answer the question of origin of the zero-bias anomaly, whether it is density of states effect or barrier effect. For example, the experimental results of thin film tunneling

[16]The low-temperature LSMO is ferromagnetic, so there is some mechanical strain change related to change of the magnetic field.

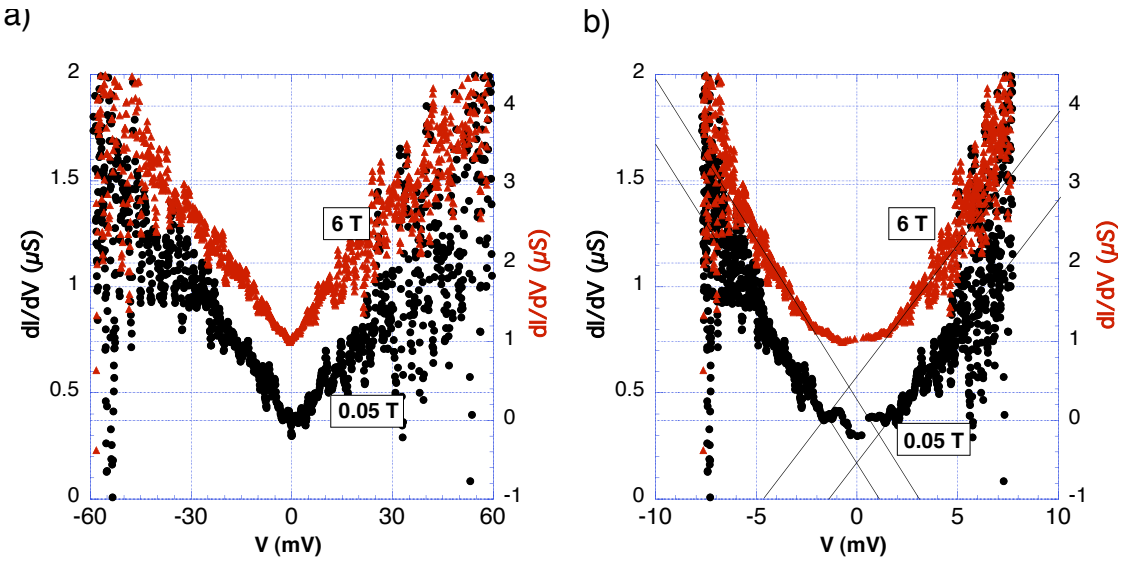

Figure 3.2. Dependence of LSMO 36% Tunneling Conductance on Magnetic Field. Neither of the Plots, a) in Voltage or b) in $\sqrt{V}$, Indicates a Distinguishable Difference Between Spectra at 0 and 6 Tesla.

between normal metals [28] across a barrier with magnetic impurities show very little sensitivity to magnetic field up to μ_0H$\sim$15 T, which is quite consistent with our data as well.

3.1.2 Temperature Dependence. When temperature dependence of point contact junctions was measured, junction instability was an even larger issue than in the magnetic field-dependence measurement. A pair of scaled $dI/dV(V)$ curves (measured on different junctions on one sample) is displayed in Figure 3.3a, which shows the temperature dependence of the cusp-like zero-bias anomaly at temperatures 4.2 K and 58 K. The low-temperature dataset is denoted by solid blue/black diamonds, and the data measured at 58 K is represented by empty red/grey circles. The dynamical conductance characteristics measured at 58 K differs from the 4.2 K measurement in the voltage range $\pm$16 mV, owing to thermal smearing[17]. In Figure 3.3b we present the

[17]The smearing is, by a small part, also due to the numerical smoothing we had to employ during the data analysis.

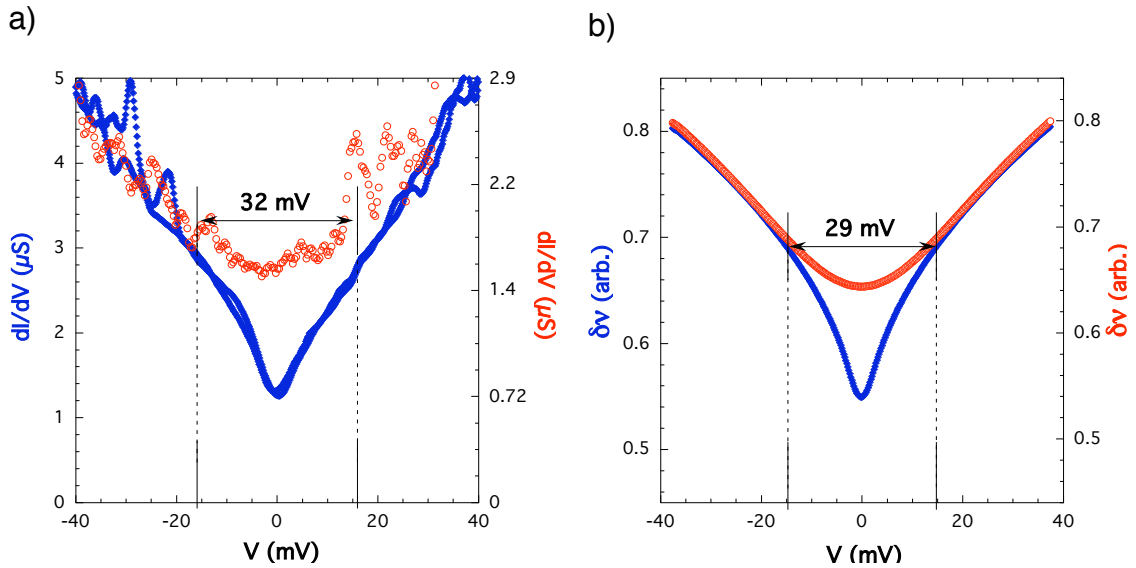

Figure 3.3. Temperature Dependence of a) LSMO 36% Tunneling Conductance and b) of Theoretical DOS Effect as Predicted by Equation 1.20. Blue/Black Diamonds Represent $T = 4.2$ K Data, Empty Red/Gray Circles Represent $T = 58$ K Data.

corresponding calculated tunneling conductance curves, for $T = 4.2$ K and $T = 58$ K. The thermal smearing in these curves is both due to the tunneling-inherent smearing and due to the temperature dependence of the correlation effect predicted by Abrikosov's result in Eq. 1.20. The observed voltage range at which the two model curves differ is ± 14.5 mV. Considering the ~ 1 meV uncertainty in the overlay of the two experimental curves, the experimental smearing is in a very good agreement with the smearing predicted by Abrikosov's theory. This agreement adds to the arguments for the electron-electron interaction mechanism. Note that the extent of smearing in the curves presented in the Figure 3.3 at 4.2 K and at 58 K is larger, both in experimental data and in the model curves, than the theoretical $2.6k_BT$ predicted in Section 2.1. This is because numerical smoothing had to be used on the experimental data to reduce random noise. For consistency, we applied the same level of smoothing on the calculated curves, so that the comparison of the temperature dependence

between data and model stays meaningful.

3.2 Tunnel Barrier Analysis

In point contact tunneling spectroscopy, junction areas and parameters of the tunnel barrier are usually unknown and they are not studied. In tunneling experiments the tunnel barrier is a necessary prerequisite to successful observation of density of states effects, but it is not necessary to know any details about the barrier, if it is high enough. The barrier material is usually of quite different chemical nature from the electrodes, like metal-oxides in metal-insulator-metal (NIN) or in metal-insulator-superconductor (NIS) junctions[18].

This is not true in case of the bi-layered LSMO (at low temperatures), which exhibits insulating character across one full surface bi-layer. The insulating phase then has *nominally* the same chemical composition as the underlying bulk metallic phase. However, the low barrier height of this surface phase requires us to extend our analysis of the tunneling spectra to include the characterization of the tunnel barrier. In this chapter we restrict our analysis of the barrier to a simple symmetrical rectangular barrier tunneling model.

Six $I(V)$ characteristics we measured are displayed in semilogarithmic plots in Figure 3.4. Freeland et al. showed [18] that the observed shape of the $I(V)$ characteristics is typical to electron tunneling through metal-insulator-metal junctions, where barrier is lower than the maximum bias voltage. In part a) the characteristics are displayed in actual units, where the only processing applied was correction of the data for the $\sim$ 50 MΩ leakage resistance. The leakage limit added to the plot as a dashed line. This plot illustrates that very similar-looking characteristics were

[18]In HTS this is also true, as the superconductivity is feature of the copper-oxide layers and tunneling barriers in point contact junctions are made of the rocksalt material separating the layers.

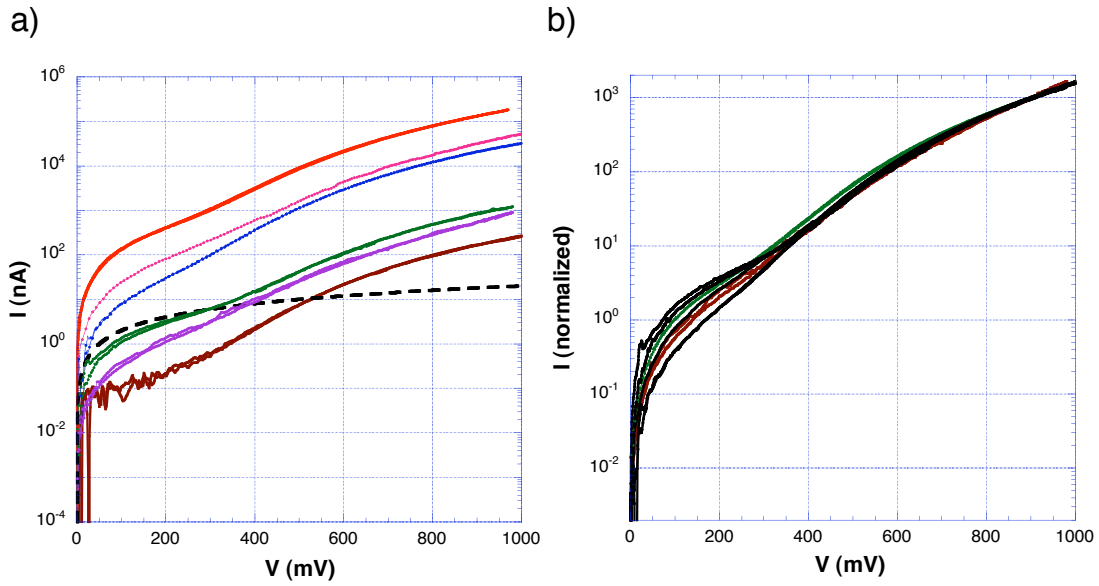

Figure 3.4. Example Set of Large-Range $I(V)$ Curves of Point-Contact Junctions in Semilog. Plots. Curves Displayed a) in Actual Current Units, and b) Scaled to Stress out Shape Reproducibility.

measured with junctions varying by 2 orders of magnitude in junction resistance[19]. For display in part b) of Figure 3.4, the $I(V)$ curves were scaled (to 10^3 at 900 mV) to display the level of the shape reproducibility. We can see that for $V > 350$ mV, the curves are almost identical, and that there is some spread in the low-bias region. As we show in Figure 3.5, there is some spread of values of barrier heights Φ among the junctions. The spread of barrier parameters explains the spread observed in the low-bias part of curves in Figure 3.4b.

An inflection is observed in most curves in Figure 3.4a around voltage $V \approx 300$ mV. It has been explained in Section 2.1 that above voltage $V \approx \Phi/e$, tunneling happens across an effective triangular barrier with thickness strongly dependent on voltage. This leads to a change in the order of power law, which approximates the

[19]Junction resistance is hereby defined as the zero-bias junction resistance. This definition is used throughout this thesis, unless explicitly stated otherwise.

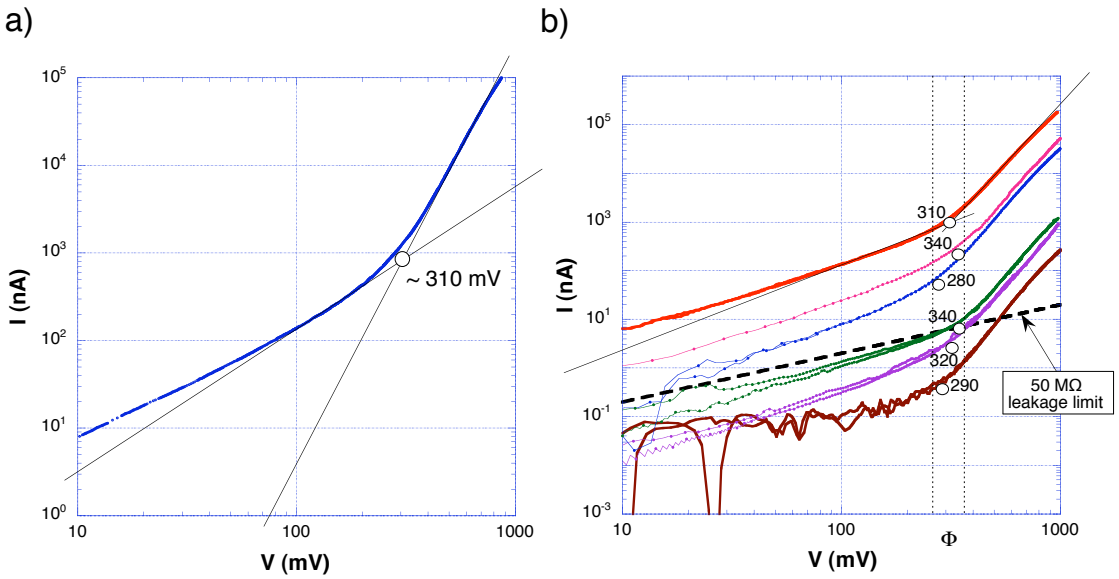

Figure 3.5. How Barrier Height Can Be Estimated From Large-Range Tunneling Characteristics in Log-Log Plots. a) Demonstrated on a Model Curve, b) Applied to 6 Experimental $I(V)$ Curves. Figure Described in Detail in the Text.

$I(V)$ below ($V < \Phi/e$) and above ($V > \Phi/e$) barrier height. This effect is best observed in the log-log plot of an $I(V)$, as presented in Figure 3.5.

In Figure 3.5a we demonstrate, how the barrier height Φ can be estimated from an $I(V)$ characteristics displayed in the log-log plot. In the particular case of the LSMO 36%, the barrier heights in the junctions were around 300 meV. We modeled an $I(V)$ characteristics using the model of coherent tunneling (Eq. 2.3) through a symmetrical rectangular barrier with berrier height $\Phi = 300$ meV, and displayed in a log-log plot in Figure 3.5a. The simulated tunneling $I(V)$ curve in the log-log display was approximated by two lines in two ranges. One line was fit in the range $100 - 200$ mV and the other was fit in the range $500 - 700$ mV. The intercept of these lines laid at a voltage $V_\Phi \approx 310$ meV. This is a good estimate of the original barrier

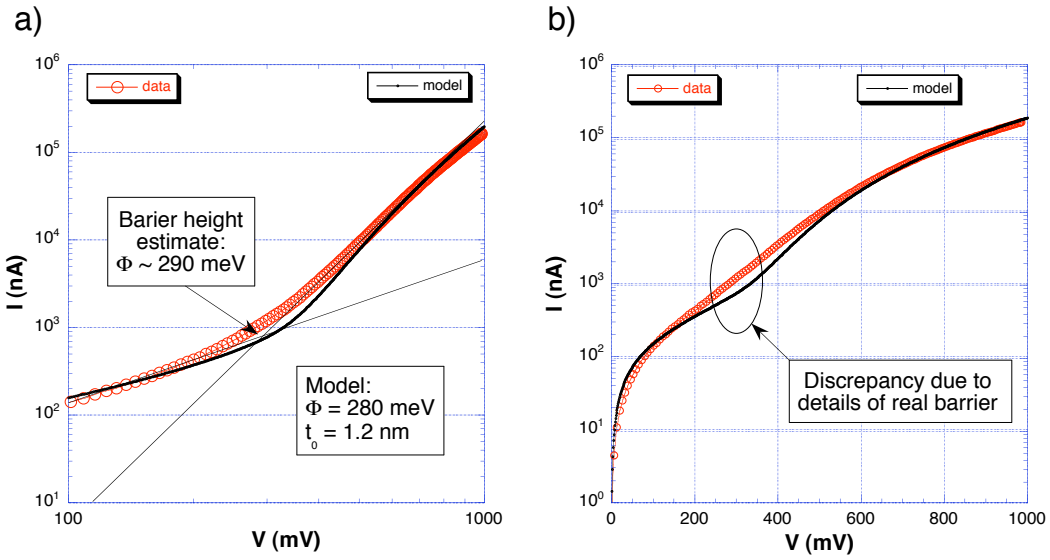

Figure 3.6. Fitting a Tunneling $I(V)$ Curve with a Model over a Large Voltage Range. a) Log-Log Plot Shows the Barrier Height Estimate at Work, b) Log-Lin Plot to Highlight the Discrepancy Between the Data and Rectangular Barrier Model.

height, and we obtained similarly satisfying results[20] when testing the procedure with model curves in the ranges of $\Phi = 100 - 700$ meV and thickness $t_0 = 0.2 - 4.0$ nm. The estimates of Φ are not extremely precise, because they are sensitive to the choice of the voltage ranges to fit those two lines. The resulting estimates have errors about ± 15 mV when Φ is close to 300 meV, and the procedure has a slight tendency to overestimate the Φ.

In Figure 3.5b we applied the graphical procedure to all six datasets from Figure 3.4 and we observed that the estimates all fell in the range $\Phi \approx 280 - 340$ meV. This represents a satisfactory consistency, considering that the junctions' resistances vary across 2 orders of magnitude. The bottom curve (the one with highest resistance) displays significantly different low-voltage dependence from the others, but this is an

[20]Naturally, the voltage ranges to fit the two lines varied with Φ.

artifact of the high resistance and related noise. This only makes that one dataset not suitable for analysis, but does not invalidate the tunneling model.

We found no *simple* test to estimate the barrier thickness t_0, which means that we had to determine it by fitting the data with an exact model tunneling $I^{model}(V)$. We used a MATLAB implementation of the Holm's expression in Eq. 2.3 and manually fitted our data. In the Figure 3.6 we show an example of a resulting best fit over a large range of voltage. The dataset, which is in both parts of the figure represented by empty red/grey circles and line, was best fit with a curve simulated for barrier height $\Phi = 280$ meV and barrier thickness $t_0 = 1.2$ nm. The initial barrier height estimate worked well, when arrived at a value 290 meV. In the semilogarithmic display in part b) of the figure we show, that in the vicinity of the fitted barrier height voltage the data is rounder than the model curve. This is most probably due to the fact that the real barrier is not rectangular - rounding of a barrier would result in rounding of the respective feature in the tunneling characteristics. It is also possible that an inelastic tunneling channel exists, which contributes to the tunnel current, but has not been included in the model.

Kirtley et al. [28] has shown that inelastic tunneling channels are not uncommon, and Zasadzinski [61] pointed out that inelastic tunneling has been frequently observed in case of other complex oxides (same category, where the LSMO belongs), the cuprate superconductors. A linear tunneling background, which is a fingerprint of tunneling via a broad-spectrum of barrier excitations was, moreover, also observed in spectra we measured on the $Tl_2Ba_2CaCu_2O_8$ cuprate. We have observed that quality of the fit in the range $100 - 1000$ mV increased, when an inelastic channel (term proportional to $V|V|$) was added. However, as we have no knowledge, what the barrier spectrum of excitations might be, we decided to proceed using elastic tunneling models in the first place and add some inelastic terms only to verify, if results change a

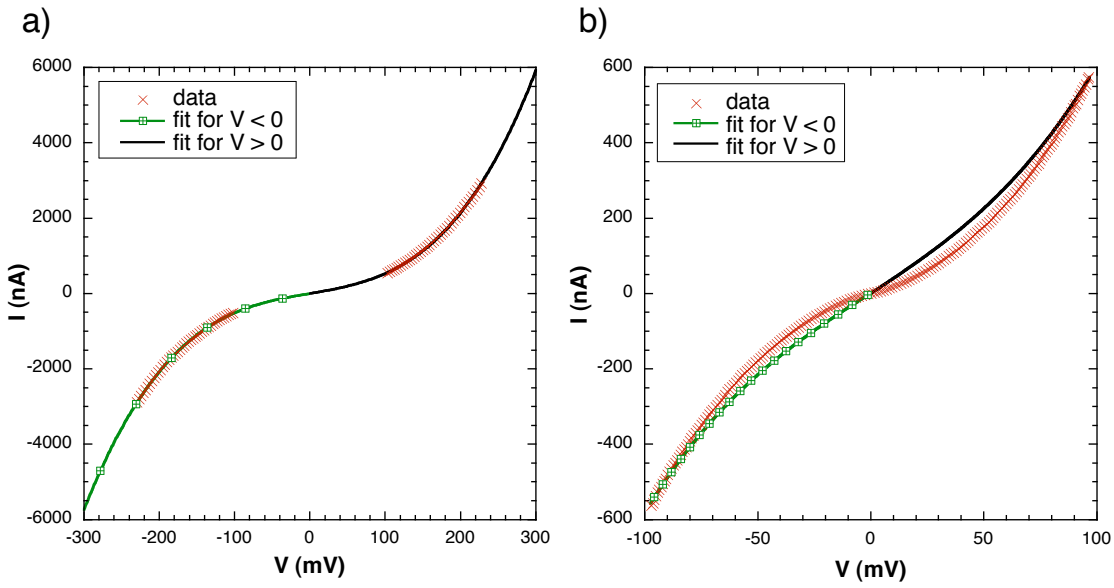

Figure 3.7. Illustration to Fitting Tunneling $I(V)$ with the Elastic Expansion Fits, Eq 2.8. a) Each Branch Was Fitted Separately over $100 \leq |V| \leq 230$ mV. b) Low-Bias Data Show Deviation from the Fits Due to Electron Correlation.

lot or not. As is shown later in this chapter, the effects on our results were negligible.

It has been mentioned in Chapter 2 that a full barrier model can be approximated with an *elastic expansion*, as given by Eq. 2.8. We have verified that this is a valid approximation for the coherent tunneling model[21]. As we observed that the simple inelastic term improved the manual fit significantly, we used a mixed model for background fits as well, the *inelastic expansion* from Eq. 2.9. In application of any background fit, the zero-bias value of the fit conductance (labeled a in the expansion expressions) is the most important parameter. If determined correctly, it is proportional to the *desity of states at Fermi energy with interactions removed* ν_0.

Using a χ^2 optimization presented in Subsection 2.1.2 we established that a

[21]The coefficients a and b could not be satisfactorily related to barrier parameters Φ and t_0 via Simmons' model, though (see Appendix C)

near-optimal range for fitting the tunneling background is $100 - 230$ mV of each polarity. There is, consistently, an asymmetry in the tunneling spectra. Quantitatively, the asymmetry varies, and is apparently a result of a slightly asymmetrical barrier and mechanical instability of the point-contact junctions. We accounted for the asymmetry by fitting the positive and negative parts of tunneling $I(V)$ curves separately, but we made no attempt to quantify it.

3.3 Determining the Elastic Scattering Time

An example illustration to our fitting procedure is shown in Figure 3.7. Plot a) displays the -230 to -100 mV and $+100$ to $+230$ mV sections of a tunneling $I(V)$, along with two a fit curve in each branch (polarity). The fits were made using elastic expansion Eq. 2.8. Plot b) shows the same dataset and fits in the range $|V| \leq 100$ mV, which is where the correlation effect is found. The effect is evident from the discrepancy between the data and the fit curves. By using the Eq. 2.7 on each branch of the $I(V)$ with its fit $I_{fit}(V)$ we obtain normalized conductance curves, such as the ones displayed in in Figure 3.8.

In Figure 3.8a, two normalized conductance curves have been displayed. Both red (grey) and black datasets represent one tunneling conductance datafile, where each branch was normalized with its own elastic expansion fit. The displayed data represent one of the most successful measurements, with relatively the least amount of noise. Therefore, conservation of states is very well observable. In many other datasets we analyzed, the observation of the state conservation was severely obstructed by noise. In Figure 3.8b the low-bias parts of the same normalized conductances have been displayed versus $\sqrt{V}$. We measured the slopes $\delta\nu(eV)/\nu_0\sqrt{eV}$ for each branch and displayed the values in thick red- (grey-) outlined boxes. Using Eq. 1.28 we calculated values of the elastic scattering time $\tau_- = 21.2$ fs and $\tau_+ = 20.5$ fs (subscripts denote polarity of the respective branch). We also measured the voltage crossover values V_{CO}

corresponding to points, where $\nu(eV_{CO})/\nu_0 = 1$. These voltage values are displayed in Figure 3.8b in thin black-outlined boxes. We used Eq. 1.31 with the corresponding crossover energy $\mathcal{E}_{CO} = eV_{CO}$ to obtain another set of elastic scattering time estimates $\tau_- = 16.6$ fs and $\tau_+ = 13.43$ fs. These values roughly agree with the ones obtained above using the slopes and Eq. 1.28.

Due to fragility of the fitting procedure and the varying quality of the original data, we could only gain confidence in these estimates by examining a number of junctions. We did that and the calculated estimates of τ for 8 junctions [22] have been summarized in Table 3.1. In this table, the first column contains the codenames of the junctions and the second contains the values of the experimental zero-bias conductance (ZBC) values, in microsiemens. For every junction we recorded the estimates from positive and negative branches separately. We have also taken into account the possibility of inelastic tunneling, from reasons stated earlier in this chapter. Therefore, separate values were obtained and recorded when elastic expansion (denoted "Bgnd. A" in the table) or inelastic expansion (denoted "Bgnd. B" in the table) background fits were employed. And naturally, values of τ obtained from slopes $\delta\nu(eV)/\nu_0\sqrt{eV}$ and crossover points $\mathcal{E}_{CO}$ were also recorded separately.

In order to evaluate the data efficiently, we grouped parts of Table 3.1 into several histograms. The histograms invariably show the mean value of τ estimates over the currently displayed group of data denoted $\overline{\tau}$. The discussion of relevance of the absolute value of these $\overline{\tau}$ quantities, though, is put off until the conclusion of this chapter. As the differences between τ values obtained using elastic or inelastic expansion fits are well within the error bars of our method, we primarily evaluate the data coming from the elastic background fits. After that we briefly compare these results with those based on the inelastic expansion fit and then we conclude this

[22] Measured on 2 different samples.

Table 3.1. Table of τ Values Derived Using the Slope $\delta\nu/\nu_0\sqrt{\mathcal{E}}$ and the Crossover Energy $\mathcal{E}_{CO}$. Both Types of Expansion Fits Were Used, "Bgnd. A" Is a Label for Eq. 2.8, "Bgnd. B" Is a Label for Eq. 2.9. Details Discussed in Text.

Junction	ZBC (μS)	Branch	τ (fs) from $\frac{\delta\nu}{\nu_0\sqrt{\mathcal{E}}}$		τ (fs) from $\mathcal{E}_{CO}$	
			Bgnd. A	Bgnd. B	Bgnd. A	Bgnd. B
S6-1-28	1.13	negative	22.1	27.2	16.1	19.6
		positive	28.7	46.5	18.3	23.4
S6-1-19	0.37	negative	13.8	13.5	12.0	11.7
		positive	14.8	14.0	13.1	12.7
S12-1-6	0.37	negative	12.7	15.5	15.1	17.1
		positive	12.2	11.7	14.2	17.1
S12-1-7	2.25	negative	21.2	18.1	16.6	19.6
		positive	20.5	13.5	13.4	18.9
S12-2-1	0.53	negative	16.9	15.2	14.2	18.3
		positive	13.1	15.2	14.2	19.6
S12-2-2	1.15	negative	13.8	14.2	15.1	20.3
		positive	14.1	13.5	14.7	28.3
S12-3-2	2.20	negative	17.7	15.5	18.3	28.6
		positive	18.5	12.8	17.1	27.4
S12-3-3	0.97	negative	10.6	10.2	15.1	19.6
		positive	13.4	8.2	12.7	14.2

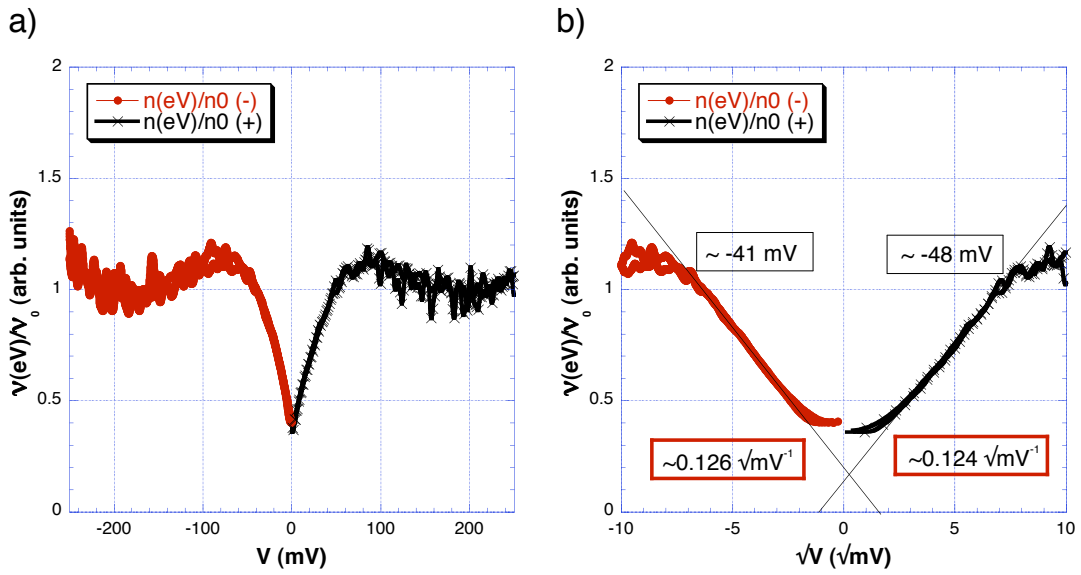

Figure 3.8. Normalized Low-Bias Tunneling Conductance Displayed a) Vs. Voltage, and b) Vs. $\sqrt{V}$. Values of the Slope $\delta\nu/\nu_0\sqrt{\mathcal{E}}$ and the Crossover Energy $\mathcal{E}_{CO}$ Have Been Extracted. Figure Described in Detail in the Text.

chapter by discussion of how our results compare with results of others.

In the Figure 3.9 we present two histograms to τ vaues. The one in part a) represents τ values, which we estimated using the method of normalized conductance slopes. This histogram was created regardless of polarities of the conductance branches and gives the maximum of values grouped in the range[23] $\overline{\tau} = 15 \pm 3$ fs. In part b) of the figure, there are τ values estimated using the crossover energy $\mathcal{E}_{CO}$ method. The values are again distributed in the $\overline{\tau} = 15 \pm 3$ fs range.

Figures 3.10 and 3.11 show the non-grouped τ values, i.e. there were only eight datapoints forming each histogram. The figure captions are give enough details about each particular histogram here. The number of data points is too low to draw serious

[23]Here and further on, the error given with the mean value $\overline{\tau}$ has been determined as the standard deviation in the respective set of τ values.

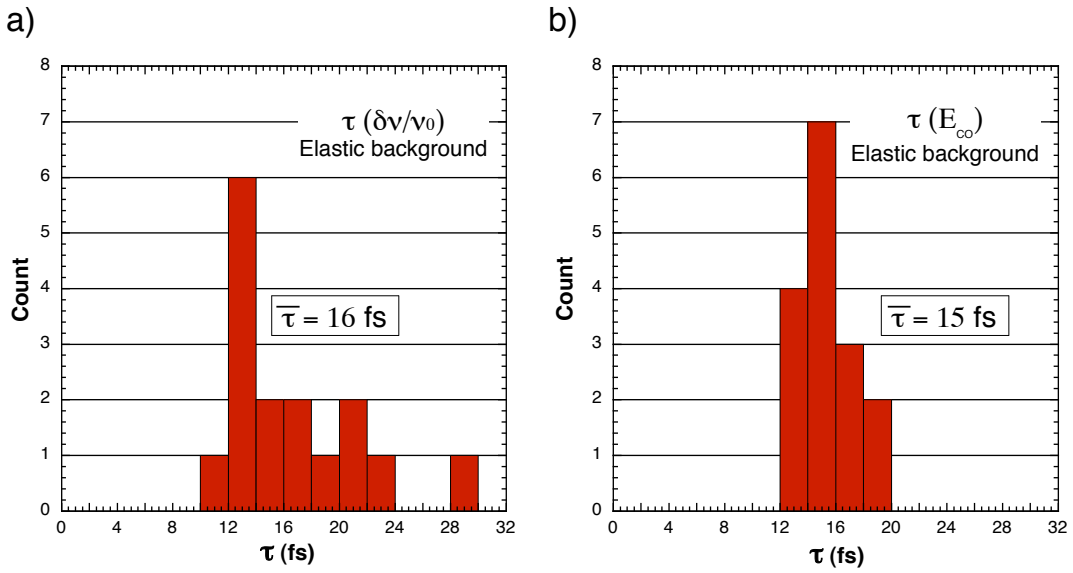

Figure 3.9. Histograms of τ Values Estimated Using a) the Normalized Conductance Slopes Method and b) the Crossover Energy Method. Each Histogram Groups τ Values Regardless of the Polarity. Plots Based Elastic Expansion Fits Only.

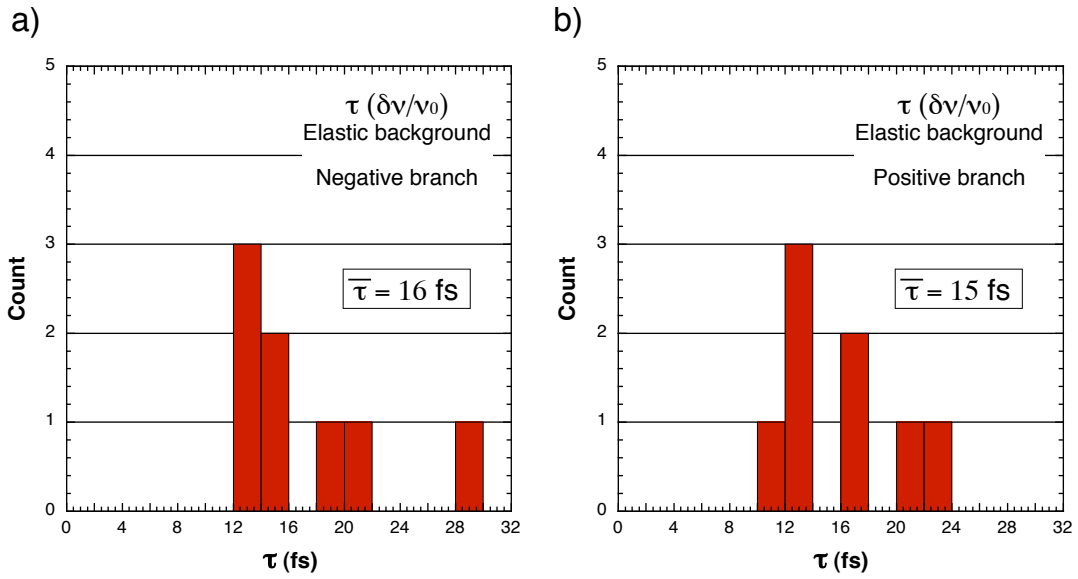

Figure 3.10. Histograms of τ Values Estimated Using the Normalized Conductance Slopes Method, a) from the Negative Branches, and b) from the Positive Branches. Plots Are Based Elastic Expansion Fits Only.

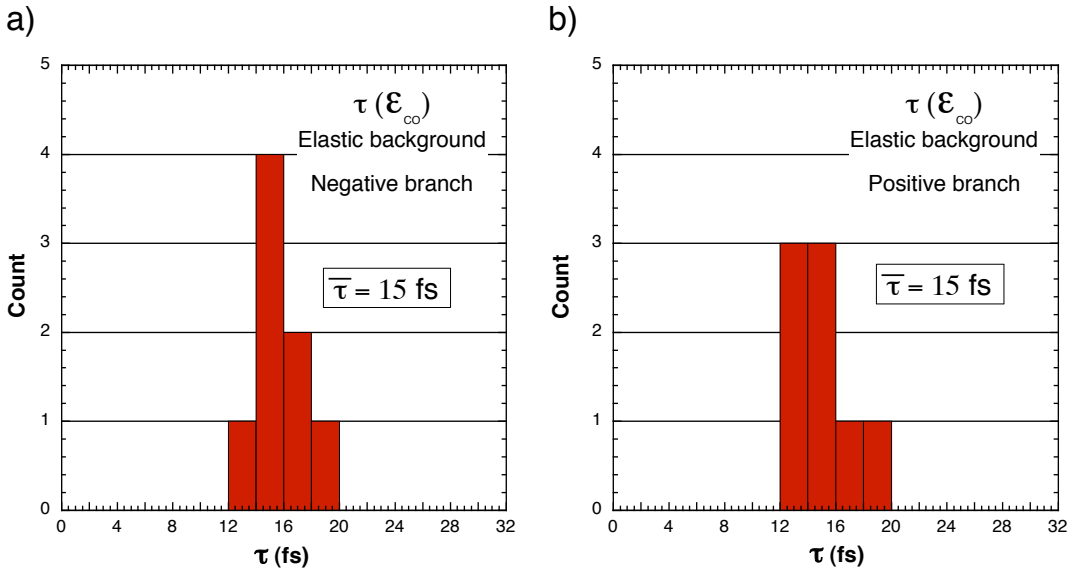

Figure 3.11. Histograms of τ Values Estimated Using the Crossover Energy Method, a) from the Negative Branches, and b) from the Positive Branches. Plots Are Based Elastic Expansion Fits Only.

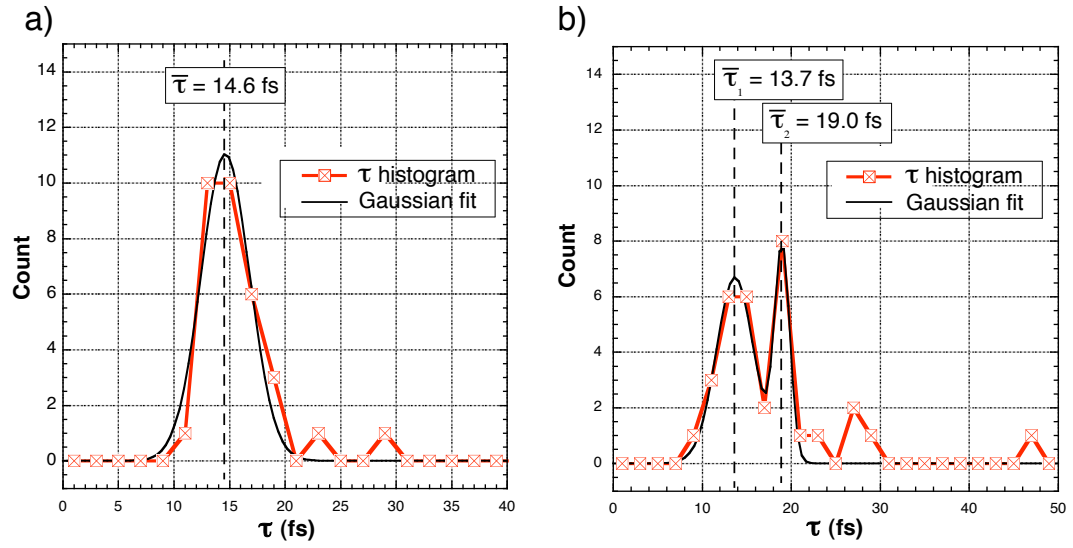

Figure 3.12. Histograms of τ Values Obtained Using a) Elastic and b) Inelastic Expansion Fits. Each Histogram Groups τ Values Regardless of the Method (Slopes or Crossover Energies), and of the Polarity. Figure Described in Detail in the Text.

conclusions. However, in each set the values are distributed quite evenly around the mean values $\overline{\tau} = 15$ fs obtained from Figure 3.9. We can interpret this so, that the obtained estimates do not substantially depend on the method, and that the two polarities are, on average, equivalent.

Finally, in the Figure 3.12 we attempted a comparison of τ distributions obtained based on conductance normalization with a) the elastic expansion fit, and b) the inelastic expansion fit. Considering the previous figures, which addressed only data based on the elastic fit, it comes as expected that the distribution in part a) of Figure 3.12 is compact, with one sharp maximum in the vicinity of $\overline{\tau} = 15$ fs. In part b), the situation is slightly different, because there are two distinct maxima $\overline{\tau}_1 \approx 15$ fs and $\overline{\tau}_2 \approx 19$ fs. Here, if we decompose the histogram in methods, one set for the "slope" method and one for the "crossover" method (not shown here, but can be reconstructed from Table 3.1), we find that values obtained using the method of normalized conductance slopes are distributed in the range $\overline{\tau}_1 \approx 14 \pm 3$ fs, whereas values obtained using the crossover energy method have a sharp distribution in the range $\overline{\tau}_2 \approx 19.0 \pm 1.5$ fs. This observation gives some reason to the fit in Figure 3.12b consisting of two Gaussians rather than one. Otherwise, the values are all within the error bars of the estimate methods and the small number of data points means that definite statistical conclusions cannot be drawn in any case. It is our best knowledge, though, that the analyzed and presented junctions are representative of all the junctions measured on LSMO in all macroscopic measurables (state parameters) of a point-contact experiment using the instrument presented in Section 2.2.

3.4 Discussion and Summary

In this chapter we have shown that the zero-bias feature in the tunneling conductance matches with the theoretical prediction made by Abrikosov for electron-electron interactions effect in quasi two dimensional metallic density of states, in the

three-dimensional limit of the model. We have verified that point contact spectra match reliably and reproducibly with a simple two-parameter model of coherent electron tunneling through a rectangular barrier. By fitting our data to this model we found the barrier height Φ for LSMO 36% in the range of $280 - 340$ meV, and barrier thickness t_0 in the range $1.2 - 1.5$ nm. These values are in agreement with those measured on LSMO 40% by Freeland et al., which verifies the insulating character of the surface bi-layer.

We have demonstrated that, by careful analysis, we were able to isolate the DOS effect from the tunnel barrier effect, despite the low barrier height. We have shown that even though the tunneling spectroscopy condition $|V| << \Phi/e$ was barely satisfied, it is possible to approximate the tunnel barrier effect by expansion $I(V) = aV + cV^3$ at intermediate voltages $100 - 230$ meV. Using this fit we were able to obtain some normalized conductance curves, which, up to the uncertainty given by the noise level, conserved states.

The normalization process is very sensitive to the choice of the tunneling background, and it was encouraging to find that an analysis of a number of measured junctions produced results in a reasonably narrow range. We analyzed the normalized tunneling conductances using two results of theory of the electron-electron interactions, which we had presented in the Introduction. We demonstrated that the resulting elastic scattering time estimates τ mostly fall in the range $15 - 20$ fs, independent of the estimating method. ARPES experiments were carried out by Sun et al. [56] and Mannella et al. [36] on LSMO $36 - 40\%$ and on LSMO 40%, respectively. From analysis of their data, which we discuss in detail in Appendix D, elastic scattering time was derived. In the $(\pi, 0)$ direction measured by Sun et al., the ARPES spectra predict $\tau \approx 5.0$ fs, whereas the prediction based on measurements in the (π, π) direction by Mannella et al. was $\tau \approx 6.6$ fs. Since the theory of electron-electron

interactions had been developed to give predictions quantitatively accurate only up to a factor of $2-3$, the absolute values of our τ estimates cannot be regarded as more accurate than that[24]. The *consistency* of our τ estimates among themselves indicate that Abrikosov's theory is an appropriate one to explain our low-bias tunneling spectra.

In the process that lead to the estimates of τ we obtained the values to the crossover energy $\mathcal{E}$ in the range $\sim 30-50$ meV. Apart from this being the energy, where (by definition from Eq. 1.31) the normalized tunneling conductance crosses over from the depression region into the enhancement region, the energy scale approximately agrees with the energy scale over which Sun et al. [56] observed renormalization of the bandstructure of LSMO 36%. For an overview of relevant ARPES measurements and a discussion of the resulting parameters, which can be derived from them, please refer to Appendix D. A brief summary and discussion has been also added to the Conclusions.

[24]Li et al. [34], for example, measured a two-fold discrepancy between their measurement of conductivity anisotropy and the prediction of Abrikosov's model. That model is the same as the one underlying the theory of electron correlations.

CHAPTER 4

OTHER SOURCES OF ZERO-BIAS ANOMALIES

In electron tunneling special attention needs to be paid to the role of the tunneling barrier. Tunneling between two normal metals through a barrier with impurities (especially magnetic ones) produces conductance spectra quite substantially different from what is expected from Equations 2.1. Conductance curves of distinct V-shape or cusp, or even a peak have been observed [28]. Barrier impurities in general can have several disturbing effects: create a conducting channel, which adds a linear term to $I(V)$ and a constant to $dI/dV(V)$, create an inelastic tunneling channel, which (according to the simplest model [28]) adds a $\propto V|V|$ term to $I(V)$ and a $\propto |V|$ term to $dI/dV(V)$, or create a distinctly anomalous tunneling channel, where the voltage dependence can be virtually any at all. We are going to discuss these effects now in relation to our observations of LSMO 36% tunneling spectra.

4.1 Direct Conducting Channels

Direct conducting channel can hardly be responsible for the zero-bias anomaly. A single conductance channel adds a constant to the junction conductance, which means that the only way to manufacture the zero-bias feature from conductance channels is to have the *number* of channels increasing as $N \propto \sqrt{V}$. To our knowledge such behavior has not been observed or even suggested in tunneling junctions to date. While it seems generally possible that number of "pin-holes" in a tunneling barrier can increase with voltage, we found no plausible explanation that would justify the necessary $\sqrt{V}$ dependence of N.

4.2 Barrier Memory Effect

In several experiments we observed a barrier effect, which implies that we can to a large extent disregard the existence of conducting channels through the

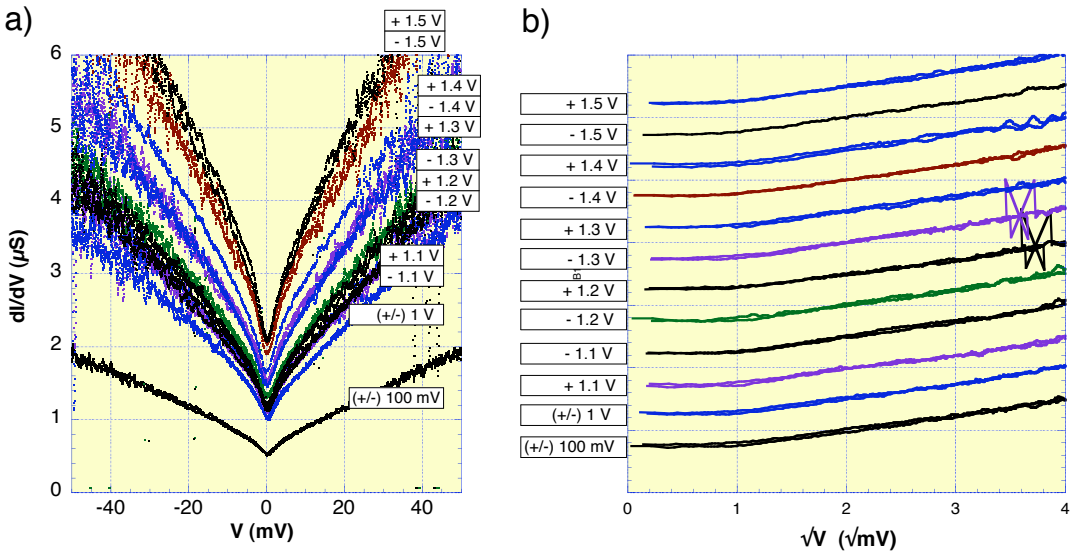

Figure 4.1. Low-Bias Tunneling Characteristics Changed Depending on the Maximal Voltage V_{max} Experienced by the Junction. Plot a) Shows the Evolution of the Tunneling Conductance with Rising V_{max}. Conductance Curves Scaled and Offset to Show Persistence of the $\sqrt{V}$ Proportionality.

tunneling barriers in our experiments. We observed, that if a junction was first created at low voltage (within ±100 mV), measured with corresponding D.C. voltage sweep, then measured with large bias sweep $\sim \pm 1$ V, and then again with sweep ±100 mV, the characteristics *before* and *after* application of the large bias were different. Since this means that junction characteristics are significantly influenced by *history* of the junction, specifically the maximum applied bias voltage V_{max}, we refer to this as the "memory" effect. As shown in the Figure 4.1a, we observed an increase in the tunneling conductance around zero bias, as the *maximal absolute bias voltage experienced by the junction* V_{max} increased. Part a) of Figure 4.1 displays dynamical conductance curves in real units, while we scaled (with fixed zero) them in part b) and then offset vertically. The offsets in this plot are artificial, without them all curves would collapse on a single one.

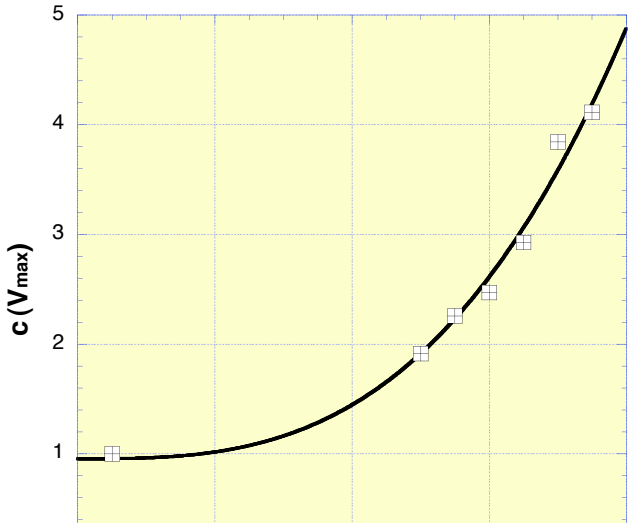

Figure 4.2. Scaling Factors of the Change in the Low-Voltage Tunneling Conductance Due to Maximal Experienced Voltage V_{max}.

This observation can be expressed as a proportionality in the voltage range $0 - 40$ mV the tunneling characteristics

$$G(V)[V_{max}] = c(V_{max})G(V)[\text{min}] \quad , \tag{4.1}$$

where the baseline conductance$G(V)[\text{min}]$ is taken from the $V_{max} = 100$ mV measurement, i.e. the smallest measured range. As a consequence, $c(V_{max} = 100 \text{ mV}) \equiv 1$. The scaling factors $c(V_{max})$ from Eq. 4.1 were plot versus V_{max} in Figure 4.2. We observe a dependence on V_{max} that can be approximated as

$$c(V_{max}) = 0.95 + 0.96 \times V_{max}^3 \quad , \tag{4.2}$$

where the numeric factor in the cubic term has units V^{-3}.

Until this point we discussed behavior of the low-bias tunneling conductance of LSMO 36% junctions, due to the the highest voltage experienced by the junction. We observed that the tunneling conductance curves do not scale at large voltages as they did at low voltages (where the empirical expressions in Eq. 4.2 is valid),

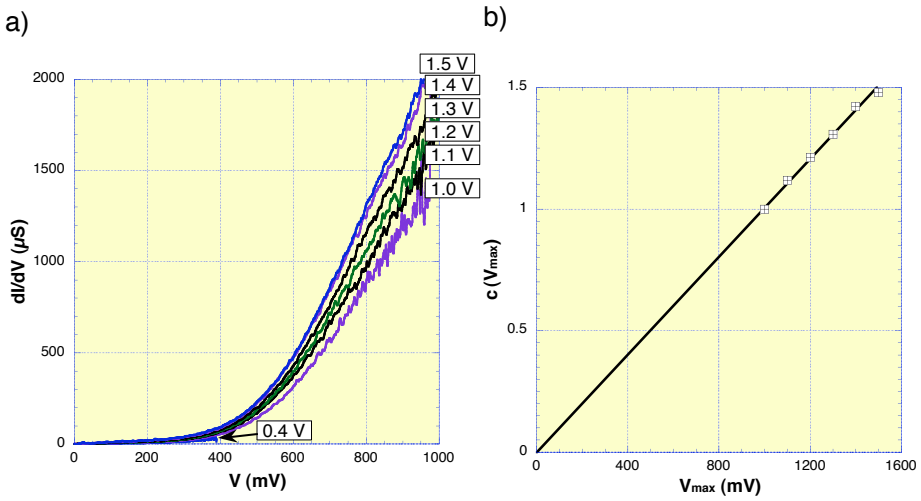

Figure 4.3. Change in High-Voltage Tunneling Conductance Due to V_{max}. Display of a) Conductance Curves, and b) Scaling Factor Values, Both vs. V_{max}.

which is illustrated in Figure fig:memorylarge. Instead, above ∼250 mV the effect is approximately following Eq. 4.1 with scaling

$$c(V_{max}) = 1.0 \times V_{max} \quad , \tag{4.3}$$

where the proportionality factor is in units V^{-1}. This proportionality law *would* be expected from linear increase of junction area, or number of directly conducting channels, but only if it was valid over the complete range of voltages.

Also, the barrier "memory effect" is partially reversible: after the measurement of the highest V_{max} range junctions were left at controlled zero bias for $10 - 16$ hours. All of them exhibited a partial return to the original conductance $G(V)[min]$: the final scaling factor after the junctions "resting" was between 1.2× and 1.8× the $G(V)[min]$. This "memory" effect is a (partially) reversible process, where the high-voltage-induced state is unstable with life-time (decay constant) in the order of $10^0 - 10^1$ hours. It is highly unlikely that such decay would occur, if the V_{max} effect

was driven by change of junction area.

At present we do not have a firm-based model to explain the observed "memory" effect, but our opinion is that it is caused by damage inflicted on the tunneling barrier by high electrical field. At fields $\sim 10^6 - 10^7$ V.cm^{-1}, damage can be caused to the barrier in the junction area, e.g. ionic dislocations or change of surface conformation[25], which may locally lower or *thin* the effective tunneling barrier. We do not observe a significant change in barrier height due to the "memory" effect and the tunneling characteristics are much more sensitive to barrier thickness, roughly as $exp(t_0)$ versus $\exp(\sqrt{\Phi})$. The fact that the effect is large in the low-voltage range and small in the high-voltage range is consistent with the picture of the defects causing a *local* change in the junction thickness. At voltages larger than barrier height, tunneling occurs across a reduced barrier thickness all over the junction and the contribution of current flowing through the damaged spot in the barrier becomes relatively less significant. The observed partial reversibility of the effect tells us that at least some of the introduced defects can recover. Naturally, the recovery rate is slow at 4.2 K owing to very limited atomic mobility.

As the "memory" effect changes the magnitude of tunneling conductivity, but does not observably change the low-voltage shape of the characteristics (i.e. the $\propto \sqrt{V}$ law is valid throughout the low-voltage data), we consider this experiment an evidence that the tunneling conductance characteristics we are measuring are influenced by barrier effects, but the zero-bias anomaly is *not* a barrier effect, but a true image of the LSMO density of states.

4.3 Inelastic Tunneling Effect

---

[25]It has been known for some time that crystal structure of real mixed manganites is more or less distorted from the basic cubic (rectangular) shape. Naturally existing stationary distortions, for example, are called polarons.

We discussed the effect of inelastic tunneling via a linear spectrum of barrier excitation modes on the tunneling characteristics earlier. Constant spectrum of inelastic tunneling states in the barrier leads to contribution to tunneling current proportional to $V|V|$. We have considered such inelastic tunneling channel in our manual fitting procedure and in one of the computer-aided least-square fitting procedures. We have verified that in the low-bias region the influence of the inelastic channel on the fit coefficients is not negligible. Major drawbacks of inclusion of the $V|V|$ term in the background fitting are that a) it does not reflect the fact that a real-life spectrum of barrier excitations might have a very different voltage dependence near zero bias, b) the continuum of excitations must have an upper limit due to Debye cutoff, and c) the linear dependence of the inelastic contribution to conductance may be a bad approximation of the real dependence. Points a) and b) act as systematic errors in the fitting and determination of τ in Chapter 3, but they do not change the fact, that the effect is linear near zero bias, which means it cannot explain the $\sqrt{V}$ character of tunneling conductance. Point c) may, in some cases, produce an effect (artifact) in the tunneling spectra, which mimics the electron-electron interaction effect. There is no comprehensive theory available, which would allow for elimination of this effect from our consideration. We limit our discussion to listing several systems, where a zero-bias anomaly was observed and the effect was attributed to barrier effect/inelastic tunneling. The inelastic tunneling channels were due to magnetic impurities, and therefore the discussion follows in the respective paragraph below.

Out of completeness we ought to say that the barrier "memory effect" cannot be successfully described by an increase in the proportion of inelastic tunneling in the barrier. An inelastic channel we consider here does not move the zero-bias conductivity $G(0)$ value, while we see it move in Figure 4.1. Furthermore and more convincingly still, if we add a term linear in V to square-root of V effect and then normalize without subtraction of the inelastic channel, the curves do not collapse on

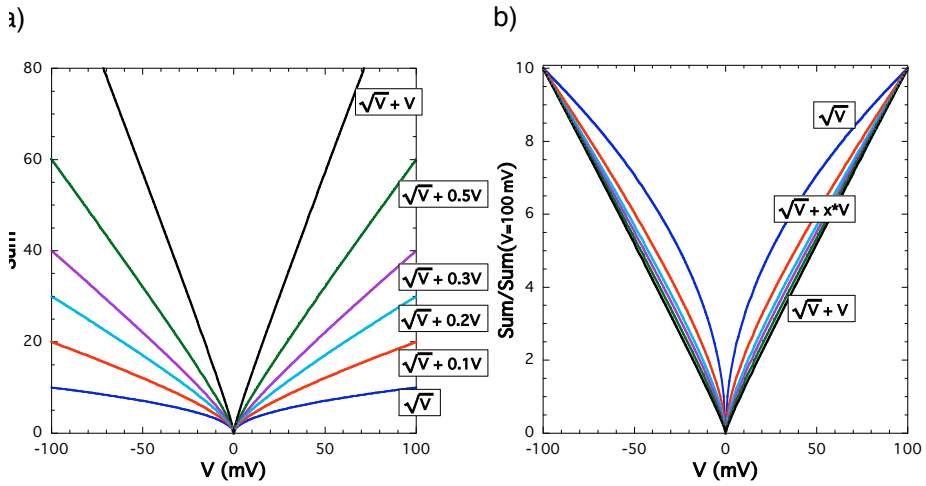

Figure 4.4. Test of the Influence of a Linear Term Mixed at Various Weights with a Model $\sqrt{V}$ Dataset. Displayed as a) Plain Weighted Sums, b) Normalized Weighted Sums.

one as the LSMO tunneling curves did in Figure 4.1. Instead, they will change from the $\sqrt{V}$ shape to the linear shape as we demonstrate in Figure 4.4.

4.4 Anomalous Barrier Effect

While it was straightforward to ascertain the probable influence of conducting channels and linear-spectrum inelastic tunneling channels on our results, it is virtually unfeasible to completely eliminate the possibility that the zero-bias anomaly we measure is some anomalous barrier effect. Below, we briefly discuss a few anomalous barrier effects, which occur in other materials and evaluate the possibility that either one of them is *in principle* equal to the observed zero-bias anomaly in LSMO. As the full account of zero-bias anomalies ever observed in tunneling would require a separate study, we limit our evaluation to anomalies discussed in Wolf's book, Reference [59], section 8.5 named "Zero-Bias Anomalies".

4.4.1 Giant Resistance Peak. A large zero-bias peak has been observed in tunneling junctions with barriers containing magnetic impurities [50][28]. This effect,

however, is so large that in terms of conductances (to compare easily with our results) at 20.4 K, $G(40\text{ mV}) \doteq 8 \times G(0)$. In our case, even at 4.2 K the effect is $G(40\text{ mV}) \approx 5 \times G(0)$, while the latter value is before subtraction of the inelastic tunneling channel, which should be considered in detailed analysis. In our junctions the barrier contains magnetic material intrinsically. However, there has been virtually no change observed with magnetic field raised up to $\mu_0 \text{H} = 6$ T. Finally, the conductance observed by Rowell and Shen [50] has a logarithmic dependence on bias voltage, which is not the case in our tunneling to LSMO.

4.4.2 Magnetic Impurities in the Barrier. It has been observed by Cooper and Wyatt that doping the insulator in junctions by various transition metals resulted in a series of zero-bias conductance peaks and dips [13].Namely doping with Mn and Cr introduces zero-bias conductance minima with shapes and sizes similar to the ones we observe in LSMO tunneling. The manganese-doped $\text{Al} - \text{Al}_2\text{O}_3 - \text{Ag}$ junction at 4.2 K exhibits zero-bias minima with $\sim \sqrt{V}$ dependence in the range $|V| \leq 18$ mV, which had $G(40\text{ mV}) \approx 1.3 \times G(0)$, while manganese-doped $\text{Al} - \text{Al}_2\text{O}_3 - \text{Al}$ junction exhibits similar $\sqrt{V}$ dependence, while $G(40\text{ mV}) \approx 1.1 \times G(0)$. This is not as large as the observed effect in LSMO, but it can make a contribution, which is not negligible and cannot be separated from the major effect. We conclude that the magnetism in the barrier does not make a major contribution to the observed zero-bias anomaly, certainly not as large as the effects in $Cr - CrO - Ag$ junctions measured by Rowell and Shen. A contribution along the lines of the Mn-doped $Al - Al_2O_3 - Ag$ junctions is possible and it would be indistinguishable from the electron-electron correlation effect in the LSMO density of states.

4.4.3 Semiconductor Conductance Minima. Hall et al. published in 1960 their observation of zero-bias conductance minima in characteristics of metal-insulator-semiconductor junctions [22].This effect was to high degree of confidence explained

by Duke et al. [15] as originating from phonon emission. The anomaly can have various shape and magnitude, but it is remarkably insensitive to temperature changes, which eliminates the underlying mechanism from our consideration of barrier effects in LSMO.

4.4.4 Giaever-Zeller Resistance Peak. This effect has been first observed by Giaever and Zeller as in $Al - Al_2O_3 - Al$ thin film junctions, where Sn particles were deposited onto the barrier and oxidized before deposition of the second Al electrode [20].The tunneling mechanism here is effectively a parallel sum of direct tunneling between the Al electrodes and two-step tunneling along the path $Al \rightarrow Sn \rightarrow Al$. This is one of the best understood systems, which however seems to be of little relevance in our problem. The conductance minimum has a profile distinctly proportional to V rather than $\sqrt{V}$, and the effect is large $G(40\text{ mV}) \approx 12 - 30 \times G(0)$. For these reasons we eliminate this type of tunneling barrier effect from our considerations on LSMO.

4.4.5 Nonequilibrium Effects in Tunneling. The last type of zero-bias anomalies Wolf discussed in Reference [59] is the influence of nonequilibrium on the tunneling conductance. It has been observed in $Mg - MgO - Mg$ tunneling junctions by Adler et al. [4] and we choose to mention this effect here out of completeness. Magnitude of this effect in the above-mentioned junction was about 1% (or $G(5\text{ mV}) \approx 1.01 \times G(0)$), the minimum was localized in the range ± 4 mV, and the conductance profile had little resemblance to $\sqrt{V}$ dependence. For this, once again, we disregard the nonequilibrium effects from our analysis.

4.5 Summary

To sum up, among the candidates for barrier effects that might produce the observed zero-bias conductance minimum in LSMO we found one possible candidate.

It is the effect observed in the junctions with manganese-doped barriers. Neither Cooper and Wyatt, nor Kirtley et al., who studied effects of Cr_2O_3 barrier doping, published temperature dependence of the zero-bias anomalies they observed. We are not aware of any model of the magnetic impurity effects, which make predictions on the temperature dependence of the impurity effect in tunneling conductance. Model that would be acceptable explanation to the tunneling effect in LSMO must predict the temperature dependence of the anomaly with similar of better precision than the prediction of Abrikosov, as demonstrated in Figure 3.3. Magnetic field dependence of the zero-bias anomaly in the Cr_2O_3-doped tunnel junctions was measured and published by Kirtley et al., however the effect of magnetic field $\mu_0 \mathrm{H} = 6$ T in the voltage range ± 5 mV was approximately 0.2%. The electron-electron interaction, being of Coulomb electrostatic character, is predicted to have no magnetic field dependence. We conclude that our data from tunneling in magnetic field were not decisive.

CHAPTER 5

CALIBRATION OF JUNCTION AREAS

The seemly uniformity of the surface insulating phase allowed a successful calibration of the areas of our tunneling junctions by comparison with the rectangular-barrier tunneling models described in detail in Section 3.2. The key step in this analysis was the preparation of tunneling junctions with known areas. Continuous thin films of gold (of nominal thickness $\sim$ 50 nm) were sputtered on in-situ cleaved surfaces of LSMO 36% single crystals. The thin films were then patterned into arrays of 1μm$\times$1μm and 5μm$\times$5μm large contacts using the Zeiss 1540XB Focused Ion Beam (FIB) instrument. Scanning Electron Microscope (SEM) images of the resulting patterns are presented in Figure 5.1. Electrical contacts were attached to the unpatterned parts of gold covered crystal bulk and the PCT instrument was used to measure the (possibly tunneling) $I(V)$ characteristics. Instead of a bulk gold tip as in case of freshly cleaved LSMO samples, we used a soft mechanically sharpened "finger" made of annealed 100 μm gold wire to contact the gold patches in the patterned areas.

A set of current-voltage characteristics measured on the 1×1 μm^2 patterned sample is shown in the Figure 5.2a, a series of junctions measured on the 5×5 μm^2 patterned sample is shown in plot b) of the figure. These characteristics differ from the curves analyzed in Chapter 3 in one major aspect, and that is the observed "back-bending" of the $I(V)$ curves at $\sim$1 V on 1×1 μm^2 pads and at $\sim$0.6 V on 5×5 μm^2 pads. However, the same behavior was observed on several point contact junctions as well, as shown in plot c) of Figure 5.2.

Most point contact junctions, when biased with large enough voltage, exhibit the same behavior as shown in Figure 5.2. Locations of the $I(V)$ local extremes vary in thin film junctions as well as in point contact junctions. Current-driven

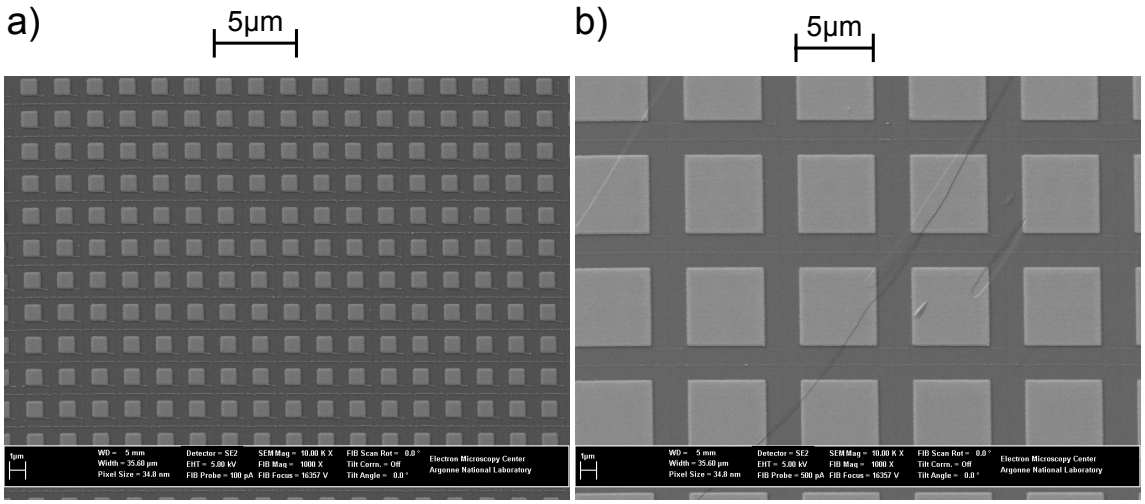

Figure 5.1. SEM Detail Images of Patterned Thin Gold film on LSMO 36%, Fabricated Using Focused Ion Beam. a) Array of 1 μm $\times$ 1 μm Pads with 1 μm Spacing, b) Array of 5 μm $\times$ 5 μm Pads with 2 μm Spacing.

instabilities of bulk conductance of LSMO have been observed before. We consider the extremes in the point-contact $I(V)$ to be results of similar instabilities in the tunnel barrier, perhaps due to a combination of imperfections in the barrier and high current flow. While it is impossible to tackle the data near and above the $I(V)$ extremes with tunneling models, analysis of data obtained well below those extremes can be successful, as demonstrated in Chapter 3. The point contact data and the data measured on the 5×5 μm^2 thin film junctions do not offer large enough voltage range to reliably apply a tunneling model. We focused on analysis of the 1×1 μm^2 thin film junctions.

When applying the tunneling models to LSMO thin film spectroscopy data, we need to consider a few distinctions from point contact spectroscopy. Thin film junctions have a fixed area and it is likely that the gold patches cover areas much larger than any mean distance of crystal imperfections - steps after cleaving, shear dislocations, impurities, intergrowths[26], and more. It is likely that some of these im-

[26]An intergrowth is a grain embedded in the bi-layered single crystal that has

perfections in the junctions are responsible for the instability described above, and while point contact junctions can be created small enough to avoid these imperfections, thin film junctions are fixed and avoiding imperfections can be only done by down sizing the contacts at the sample preparation stage. Secondly, it is possible that the insulating character of LSMO surface is a result of the free boundary condition, which does not hold, when additional material is deposited. Therefore we cannot make any assumptions about thin film spectra based on the point contact measurements.

In order to use the tunneling model we are going to *assume* that tunneling takes place in the thin film junctions too. This assumption is to a likely to be a valid one. In Figure 5.3, we show that below 600 mV the thin film $I(V)$ characteristics can be fit with the coherent (momentum conserving) tunneling model with inclusion of inelastic tunneling channels. The same effect could be simulated by using a different shape of the tunnel barrier than the rectangular one, for example one including significant influence of image forces (for details please refer to Ref. [59]). In Figure 5.3 we show the same model (with different parameters) applied on a) point contact data and b) thin film $I(V)$ data. The upper limit of the fitting range (600 mV) is chosen to avoid influence of the instability, while lower limit is ∼80 mV so as to avoid the region of the zero-bias anomaly[27]. Owing to the large proportion of inelastic tunneling the thin film $I(V)$ fits are burdened with more uncertainty in Φ and t_0 as the analyzed point contact tunneling data, which in the end results in an error on the estimate of point contact junction areas.

---

a perovskite character. It is not possible to manufacture perfect crystals and certain amount of intergrowths needs to be taken into consideration.

[27]The tunneling conductance of thin film junctions near zero bias is clearly V-shaped with no suggestion of a $\sim \sqrt{V}$ cusp. This is consistent with the large proportion of inelastic tunneling necessary to fit the data.

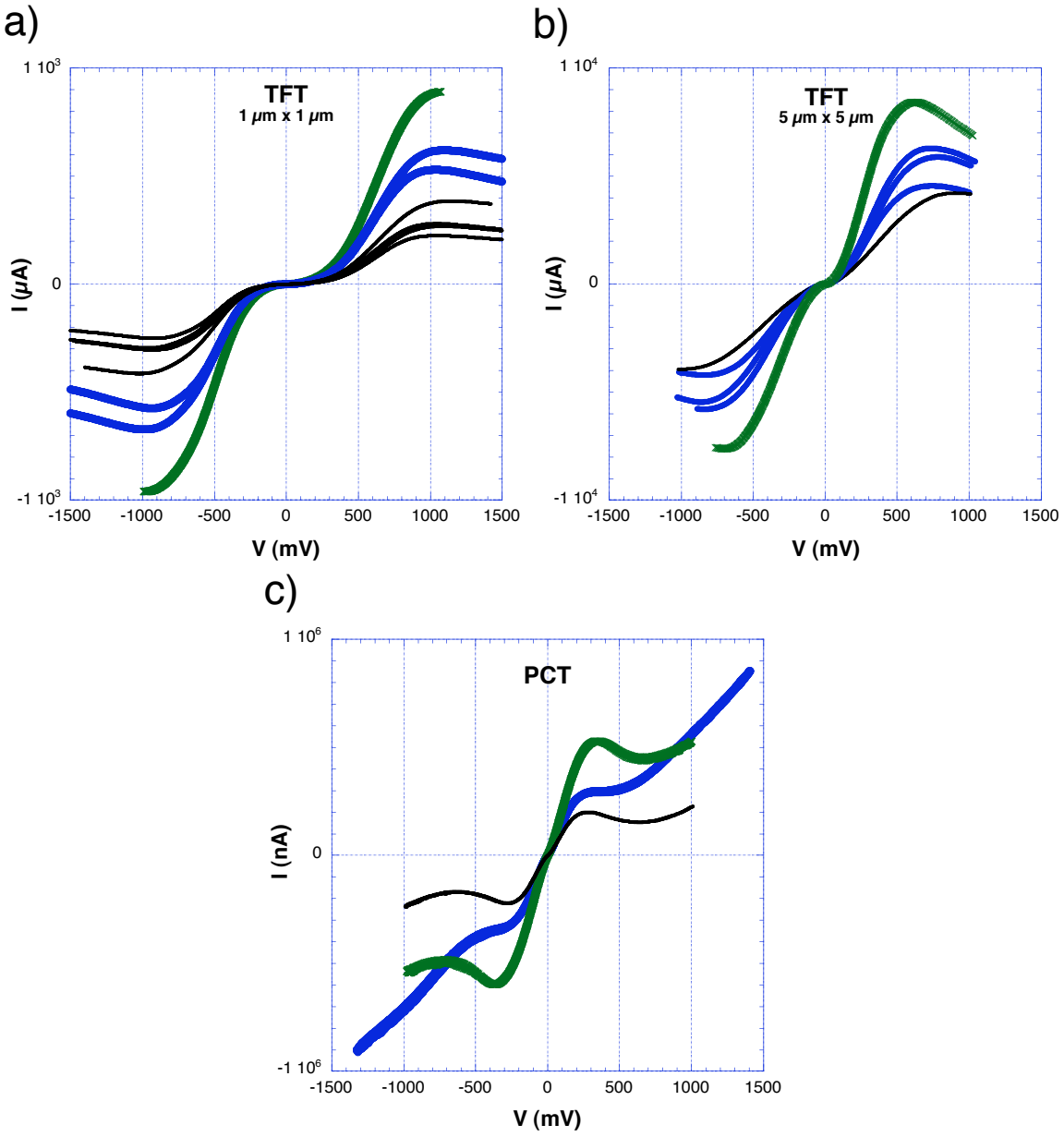

Figure 5.2. Tunneling $I(V)$ Characteristics of Some Junctions Exhibit an Instability. Curves Measured on a) an Array of 1 μm $\times$ 1 μm Pads, b) an Array of 5 μm $\times$ 5 μm Pads, c) Some Unstable Point Contact Junctions.

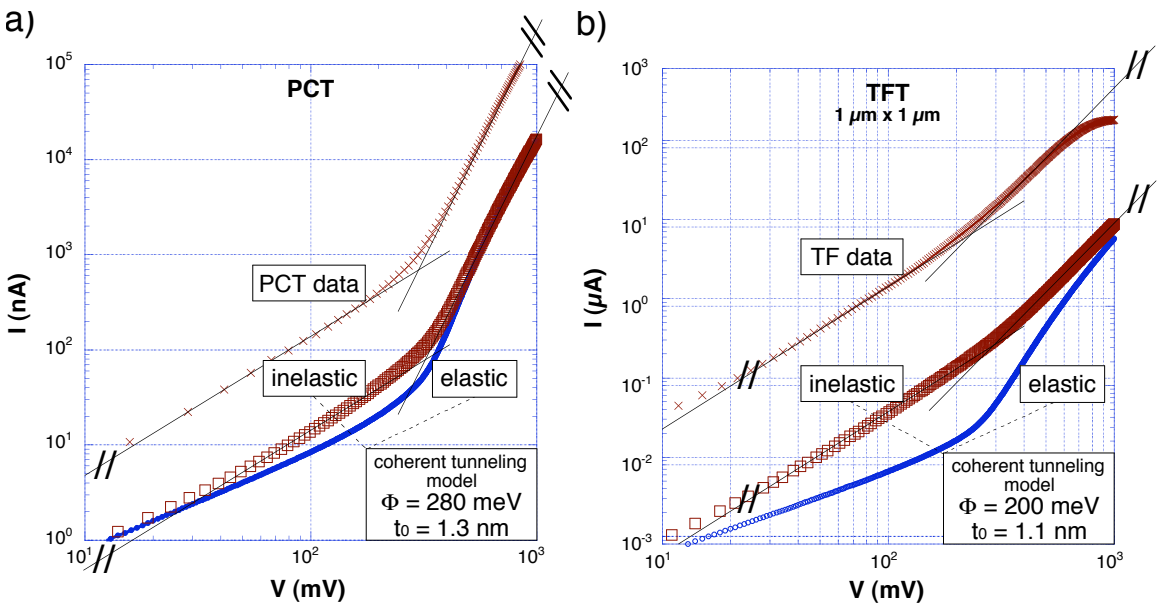

Figure 5.3. Manual Fitting of Tunneling $I(V)$ Characteristics Using Coherent Tunneling Model with Inelastic Channels. We Display a) Fitting Point Contact Junction Data, b) Fitting 1 μm $\times$ 1 μm Pad Thin Film Junction Data.

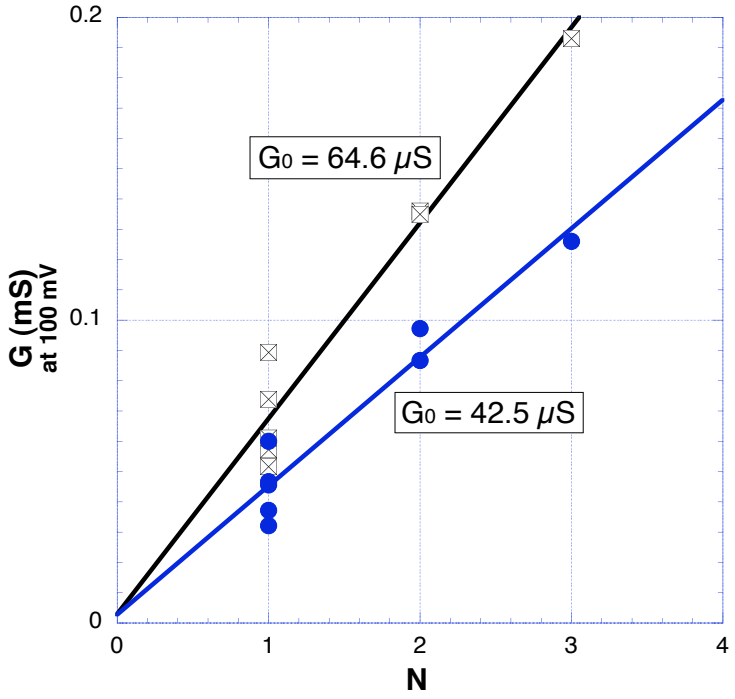

Figure 5.4. Illustration of the Procedure of Calibration of Thin Film Junctions Areas. Figure Described in Detail in the Text.

As the soft "finger" tip used in thin film experiments is expected to bend rather than flatten (which is the case with bulk gold tip in point contact experiments), it is unlikely to contact as large areas as the bulk tip would. Based on this idea we assume that the gold "finger" contacts most likely one to four gold patches at a time, occasionally making contact in the area between gold patches. We have calibrated the number of contacted patches N in Figure 5.4 based on this assumption. The two datasets in the figure correspond to G(+100 mV) (the higher dataset) and G(-100 mV) (the lower dataset) of the same tunneling conductance curves. The linear fits through the data make intercept near zero of the plot for both polarities, although the slopes are different (it can be demonstrated that this is due to barrier asymmetry, but it does not make any difference in the rest of the analysis). As the nominal patch size is $A_0 = 1\mu\text{m}^2$, the scaling of the histogram axes can be interpreted in terms of conductance per unit area

$$\gamma_{TF}(V) \equiv \frac{G(V)}{N \cdot A_0} \quad , \tag{5.1}$$

where the subscript TF distinguishes thin film junctions (barrier heights $\Phi \approx 150 - 200$ meV and thickness $t_0 \approx 1.1 - 1.2$ nm) from point contact junctions. We are going to use the subscript PC to distinguish the latter.

Until this point we have been using normalized model $I(V)$ curves in fitting, for easy manipulation. However, to connect the point contact tunneling characteristics with the thin film tunneling, we need to work with model curves *not* normalized. For the approximate area calibration we used the $G(V{=}0){=}\frac{dI}{dV}|_{V=0}$ values of model curves fitting the point contact $I(V)$ data. It can be observed in Figure 5.2a that there is a spread of barrier parameters among the measured $1\mu\text{m}^2$ gold pads. We carried out the following calibration procedure for one $N = 1$ junction, one $N = 2$ and one $N = 3$ junction from Figure 5.2a. The results presented below have been

averaged and the errors estimated to include all three values.

We have fitted the positive-bias part of the thin film $I(V)$'s using Eq. 2.1 with parameters $\Phi = 190 \pm 15$ meV and $t_0 = 1.1 \pm 0.1$ nm, in point contact fit we typically used $\Phi = 280 - 380$ meV and $t_0 = 1.3 - 1.7$ nm. We used one MATLAB program to generate the corresponding coherent tunneling model curves (not normalized), so that the set of $I(V)$ model curves thus generated could be treated as using a common value of junction area. Inelastic tunneling term added in determining barrier parameters does not change the zero-bias conductance $G(0)$. Then the experimental data were compared with the not-normalized best fitting model curves, so that ratios $G(0)^{exp}_{TF}/G(0)^{m}_{TF}$ and $G(0)^{exp}_{PC}/G(0)^{m}_{PC}$ could be determined[28]. If we define the ratio of the zero-bias conductances of the two model curves $\chi = \frac{G(0)^{m}_{PC}}{G(0)^{m}_{TF}}$, then the point contact junction's are can be estimated as

$$A = \chi \frac{G(0)^{exp}_{PC}/G(0)^{m}_{PC}}{G(0)^{exp}_{TF}/G(0)^{m}_{TF}} A_0 \quad , \tag{5.2}$$

where A_0 is the unit area $A_0 = 1\mu\text{m}^2$.

The results for six sample point contact junction are presented in Figure 5.5 and Table 5.1. Junctions D, E and F have too high resistance junctions, D: $R(0\text{ mV}) \approx 50$ MΩ, E: $R(0\text{ mV}) \approx 80$ MΩ, and F: $R(0\text{ mV}) \approx 170$ MΩ, so that our instrumental leakage current dominated the low-voltage parts of the characteristics. The resistance values, as well as the presented junction areas have been extrapolated from high-voltage regions and, therefore, exhibit larger error. Errors presented in Table 5.1 are dominated by the principal uncertainty in barrier fit parameters. Due to the necessity to use a manual fitting procedure, our sampling of the parameter space

[28]All measurements analyzed in this chapter were taken at temperature 4.2 K, which means all $G(0)^{exp}_{TF}$ and $G(0)^{exp}_{PC}$ were comparable.

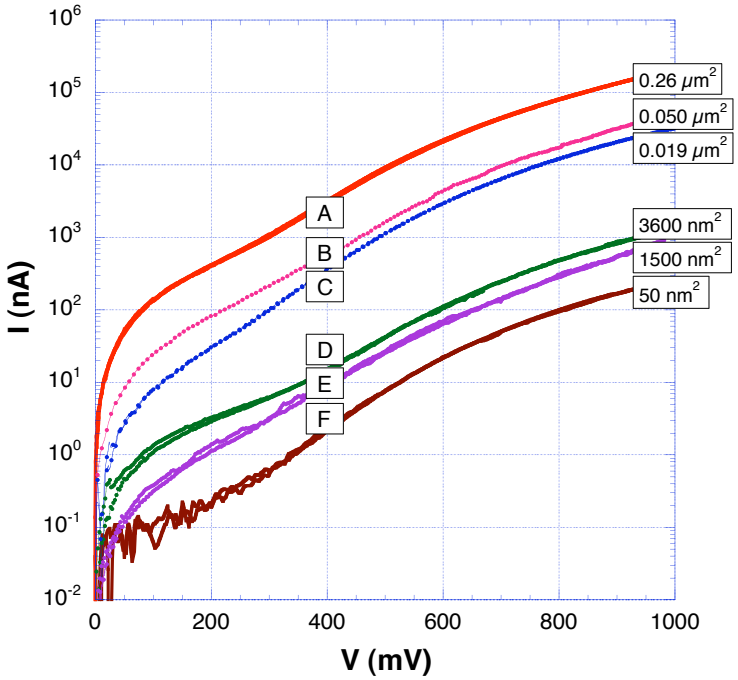

Figure 5.5. Example Set of Six Point-Contact Tunneling $I(V)$ Curves With Areas Calibrated by Our Method.

Table 5.1. Table of Six Point Contact Tunneling Junctions and Their Areas.

Junction Label	Area (nm^2)	Error (%)
A	26×10^4	35
B	5.0×10^4	40
C	1.9×10^4	40
D	3600	50
E	1500	50
F	50	60

was $\Delta\Phi = 5$ meV and $\Delta t_0 = 0.05$ nm. Combination of these two errors alone gives $\sim 25-30\%$ uncertainty. An automated fitting procedure programmed on a dedicated computational cluster (because of numerical integration involved and expected $\sim 10^2$ iterations per fit) seems indicated.

Under the assumption stated at the beginning, that the thin film junctions are predominantly tunneling junctions, it is the best attempt to date to estimate the point contact junction areas in our laboratory. We have not observed any signs that the thin film junctions might be incompatible with tunneling models. As an outlook to the future, the correlation of junction areas with amount of inelastic tunneling included in the rectangular barrier model fits *may* provide a measure of the uniformity range of LSMO surface insulating phase. An in-depth analysis of this correlation, however, goes beyond the scope of this work.

CHAPTER 6

SURFACE CHEMICAL ANALYSIS USING XPS

The x-ray photoelectron spectroscopy (XPS) is a widespread tool for investigation of chemistry of surfaces of solids. The XPS is one of few spectroscopies that allow quantitative chemical analysis of specimens. Recently, there have been reports [29] that surface of cleaved LSMO single crystals experiences strontium enrichment. Such depth variation of concentration could be directly translated as depth variation of doping x, as used in the general formula $La_{2-2x}Sr_{1+2x}Mn_2O_7$, and would present a likely cause for the insulating character of the surface LSMO bi-layer. We applied the quantitative analysis on data we measured on in-situ cleaved crystals of bi-layered LSMO 36% to determine the depth profile of $\xi(Sr)/\xi(La)$ (relative abundance of lanthanum and strontium) in the surface. We found that in the range of probed information depths $0.6 - 2.5$ nm[30] the relative concentrations of lanthanum and strontium do not change significantly. Our experiment, however, did not address depths between 0 and 0.6 nm, and concentration changes localized in the first three atomic monolayers, if they happened, could not be resolved.

6.1 Principles of Photoemission Spectroscopy

6.1.1 Description of a Photoemission Spectrum. Photoelectron spectropy probes occupied energy levels in materials, usually solids, by creating electron-hole pairs in the material by incident electromagnetic radiation (photons) and collecting the electrons that escape the solid in the direction of analyzer. The mechanism of photoemission is illustrated in Figure 6.1, part a). Part b) of the figure contains an

[29]Private communication with Chuck Fadley and Von Braun Nascimento, Oak Ridge National Laboratory, from LEED experiments.

[30]These are values of inelastic mean free path in LSMO 36% given by standard predictive formula by Tanuma, Penn and Powell. It may not be fully applicable to LSMO.

illustration to the Auger mechanism, which is a secondary mechanism accompanying photoemission and creating additional peaks in photoemission spectra. Auger mechanism, which can be separately used for chemical analysis in Auger Electron Spectroscopy (AES), brings the core-level hole created by photoemission up to the valence band by upper level→ core level transition, and the released energy is released as another electron is emitted. Three electrons are involved in this process, which is why Auger peaks are usually labeled by letters corresponding to the involved subshells, e.g. KLL, MNN, etc. In our analysis we only need to identify the Auger peaks correctly to remove them from the analysis, which only involves photoelectron peaks. Apart from these sets of peaks, photoelectron spectra contain satellite peaks adjacent to photoelectron peaks, and characteristic inelastic loss peaks. These can be subject to analyses via specialized spectroscopies, such as Electron Energy Loss Spectroscopy (EELS). Finally, every photoemission spectrum contains signal background, which is made of electrons inelastically scattered on the way from their originating atom to the analyzer. For quantitative analysis the background is estimated and only intensity (area) of peak above the background is counted in.

Electrons in atoms of every element occupy a unique series of energy levels given primarily by total charge of the atom nucleus. The energy distribution of electrons collected by the analyzer will, therefore, have peaks at kinetic energies characteristic to the elements in the studied compound. Due to energy conservation law, a photoelectron spectrum cannot contain information about energy levels deeper below the Fermi level than what is given by energy of incident photons hf. More precisely, the formula of energy balance is

$$hf = BE + KE^{vacuum} + \Phi_{sample} = BE + KE^{analyzer} + \Phi_{analyzer} \quad , \tag{6.1}$$

where BE is the binding energy of the electron core subshell, KE^{vacuum} and $KE^{analyzer}$ are representations of photoelectron kinetic energy with respect to "vacuum" (kinetic

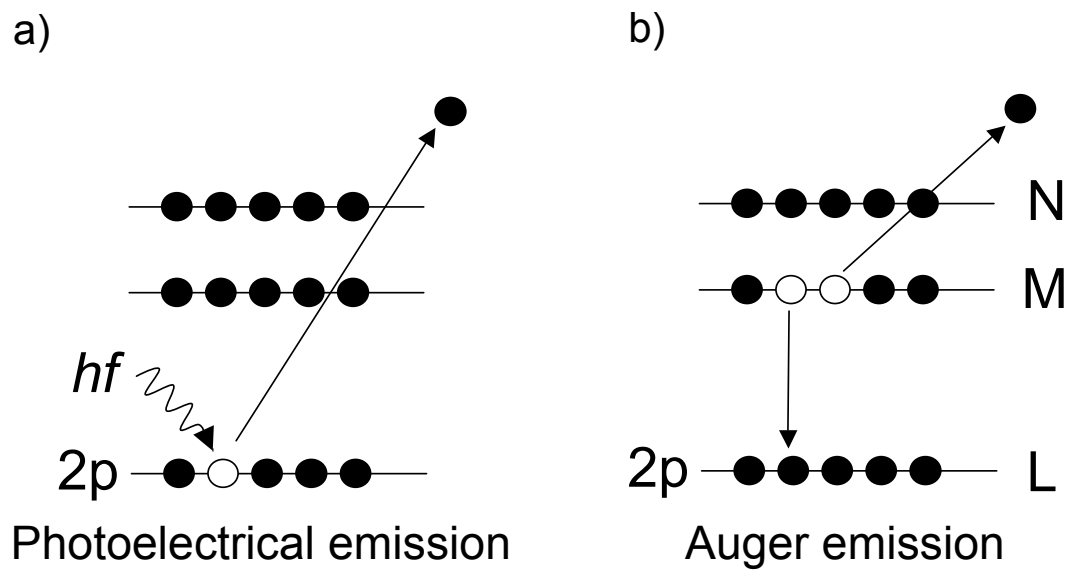

Figure 6.1. Diagrams of a) Photoemission and b) Auger Mechanisms. Figure Described in Detail in the Text.

energy, with which photoelectron escapes sample) and with respect to the analyzer Fermi energy, and Φ_{sample} and $\Phi analyzer$ are work functions of sample and analyzer, respectively.

The key material property that determines information depth of the method is the inelastic mean free path (λ_{IMFP}) of electrons. Although the IMPF depends significantly on the studied material and on the kinetic energy of the photoelectrons, its values in our experiments are in the order of $10^{-1} - 10^{0}$ nm. Therefore, photoelectron spectroscopies and AES are considered *surface-sensitive* probes. Advantages and limitations that come as consequences of this fact will be pointed out in due course, wherever relevant to our experiment.

Size of valence bands in solids is in the order of electronvolts, while core electron levels of the highest two or three core subshells are typically $10^{1} - 10^{3}$ eV below Fermi energy. Photoelectron spectroscopy that focuses on the valence band, usually used to study band structure of conducting solids, uses incident radiation in the ultraviolet

range and is called Ultraviolet Photoelectron Spectroscopy (UPS). To identify the elements in a materials, information about a few core subshells is needed, which asks for $hf \sim 1$ keV, which lies in the soft x-ray part of spectrum and gives a distinctive name to the spectroscopy, the X-ray Photoelectron Spectroscopy (XPS).

Core energy levels of atoms experience changes due to chemical composition. These changes are: shifts of the binding energy of a subshell and change of shape of the corresponding peak. Both changes are distinct, but limited, and unlike the case of valence band, superposition principle between several chemical states (bonds to various other elements) of the same element remains valid. This allows for identification of chemical states of elements in new compounds by comparison with spectra of well known, simpler compounds. The superposition principle also allows for quantitative determination of the relative amounts of bonds, which at the appropriate conditions can lead to identification of entire complex molecules. For these reasons, XPS (also known as Electron Spectroscopy for Chemical Analysis, ESCA) is most commonly used in studies of surface chemical composition, contamination and chemical processes on surfaces of solids. The same type of quantitative analysis can be used to determine relative abundance of various elements in sample surface. This analysis relies on parameters (λ_{IMFP} and the so-called transition sensitivity, which is explained below) computed using sophisticated models and deemed inaccurate in systems others than ordinary metals. However, a depth-profiling method is available, which allows us to by-pass the use of some of these parameters, and gives us reliable instrument-independent profile. We describe this method below (Section 6.3) and we present results of its application in Section 6.4.

6.2 Instrumentation

The basic hardware setup necessary for XPS measurement is sketched in Figure 6.2. First of all, photoelectron spectroscopy only works well in ultra-high vacuum,

i.e. at pressures lower than 10^{-8} torr. The better vacuum is in the chamber, the better results. A series of pumps is necessary to bring the chamber down to acceptable vacuum. Usually, a rotary mechanical pump and turbomolecular pump are connected in series on the "roughing" pump line and then ion pump is attached to the chamber. The other two necessary components of an XPS setup are the source of x-rays (this can be a lamp, or a connection to a synchrotron beamline), and the detector of photoelectrons. Nowadays the most widely used are hemispherical detectors with one or more electron multipliers (channels) for increased sensitivity. The last necessary component is sample holder attached to a manipulator. In order to measure angular dependence of photoemission, which can then be calibrated to obtain concentration depth profile near sample surface, a manipulator that allows for rotation of the sample in the direction of angle ϕ marked in the diagram in Figure 6.2. Translational motion of the manipulator in three dimensions is usuallu highly desirable for sample alignment. Modern XPS instruments are operated by data acquisition applications through a computer.

6.2.1 Standalone Instrument. We have run two XPS experiments at very different conditions in two places. The first one, the lead-in experiment in our was carried out at the Department of Electronics and Vacuum Physics at Charles University in Prague, while the collaborating experts were Dr. Kateřina Veltruská and Mr. Miloš Cabala, M.S. Their photoelectron spectroscopy (PES) vacuum chamber is equipped with an X-ray lamp, which allows the use of Al-Kα ($hf = 1486.6$ eV) or Mg-Kα ($hf = 1253.6$ eV) non-monochromatized x-rays. We used the Al cathode in our experiment in order to eliminate overlap of key photoelectron peaks with Auger peaks in the spectrum[31]. The x-ray lamp floods an area of the sample holder ≈ 1 cm

[31]Photoelectron peaks are at constant BE, while Auger peaks are at constant KE, when the incident energy hf changes. Hence, the two types of peaks *shift* with respect to each other, which must avoided for successful quantitative analysis.

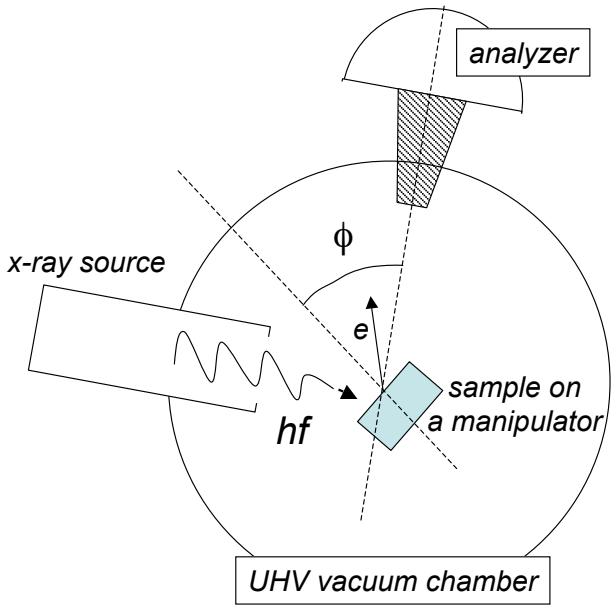

Figure 6.2. Basic Setup of an Angle-Resolved XPS Experiment. Figure Described in Detail in the Text.

in diameter, spatial resolution was not possible on our sample. By focusing on the analyzer side we selected an aperture to collect signal primarily from an area ≈ 3 mm in diameter. Even with this focusing, signal coming to the analyzer from the sample neighborhood (sample holder, glue, ...) could not be avoided and needed to be considered in data analysis.

The system is equipped with 9-channel hemispherical electron analyzer by Omicron Nanotechnologies, Inc. and the sample holder is fixed on a goniometer, which allows sample rotation along the two axis. This allowed for a measurement of spectra at various angles ϕ between sample c-axis and the analyzer input optical path axis (ϕ is called *emission angle*). The ultra-high vacuum (UHV) chamber is evacuated by a combination of turbomolecular pump and a cryogenic pump and the ultimate pressure is about 5×10^{-10} torr. The system is equipped with a load lock, which allows sample transfer into the main experimental chamber at UHV. We benefited from this

due to our implementation of in-situ cleaving of sample crystals.

6.2.2 Beamline Instrument. The second experiment was carried out at Argonne National Laboratory, at the 4-ID-C beamline of the Advanced Photon Source synchrotron, in collaboration with Dr. Richard Rosenberg. The x-ray source was the synchrotrone x-ray beam, which can be tuned in the range $hf = 500 - 2800$ eV of incident energy. When focused, the beam diameter was ~ 0.1 mm, which allowed a complete elimination of the sample neighborhood from our measurement. In order to match the other, standalone laboratory experiment we worked with the beam at primary energy $hf = 1486$ eV, which approximately matches the Al-Kα line energy.

The instrument is equipped with a single-channel hemispherical analyzer and a goniometric sample holder, which allowed measurements at various emission angles. A load-lock with magnetic transfer allowed to move samples into measurement chamber in vacuum (UHV). The ultimate vacuum pressure in the system is $5{\times}10^{-11}$ torr.

6.2.3 Sample preparation. Single crystals of bi-layered LSMO 36% with *ab*-plane cross-sections $\sim 2 - 3$ mm^2 were glued to sample plate using the TorrSeal vacuum epoxy, so that the crystal *ab*-plane was parallel with the plate. After the epoxy cured, a copper rod (~ 3 mm in diameter, ~ 30 mm long) was glued to the top of the sample using the same vacuum epoxy. After the glue cured, i.e. in several hours at room temperature, the sample destined for the experiment in the standalone laboratory instrument was covered with gold by means of vacuum evaporation. This overlayer, which covered the whole assembly of sample plate, sample and the copper rod, was necessary to avoid the variety element signals, which would be picked up by the analyzer from sample neighborhood. At the same time the gold supplied a conductive path between the sample and sample holder, which is a necessary requirement for successful photoelectron spectroscopy. This conductive path was created in the beamline setup as well, by application of colloid silver paint.

The in-situ cleaving was implemented in both experiments so that the samples were cleaved in the load chamber at pressures $\sim 10^{-7} - 10^{-8}$ torr, shortly before they were transfered to the experimental chamber. The pressures were not low enough to prevent an adsorption of several monolayers of residual atmosphere, but the conditions did prevent surface contamination with hydrocarbons, which normally happens, when crystals are cleaved in air. The actual cleaving was done by means of a force applied on the copper rod. Samples were transfered to the experimental chambers (far better vacuum) within minutes after cleaving.

6.3 Quantitative Analysis of Photoemission Spectra

Intensity I_A of a line of an element A in the spectrum is generally given by the expression

$$\begin{aligned} I_A = s_A(hf)F(KE_A) \int_{\gamma=0}^{\pi} L_A(\gamma)\sec(\delta)\times \\ \times \int_{x=-\infty}^{\infty}\int_{y=-\infty}^{\infty} J_0(x,y)T_{tr}(x,y,\zeta,\gamma,KE_A)\times \\ \times \int_{z=0}^{\infty} \xi_A(x,y,z)\exp\left[-\frac{z}{\lambda_{IMFP}(KE_A)\cos(\phi)}\right] dzdydxd\gamma \quad , \end{aligned} \tag{6.2}$$

where s_A is photoionization cross-section of the respective core level, F is the electron detector efficiency, x, y, and z are coordinates of the sample inertial system where z is in the direction of the c-axis and rises with depth from the exposed sample surface, γ, δ and ϕ are relative angles between the axis of incident x-rays ("incidence axis" for short) and the axis of analyzer ("emission axis"), between incidence axis and sample c-axis, and between sample c-axis and the emission axis, respectively. The ϕ is the *emission angle* as mentioned above mentioned above. The angle ζ is the angle between planes "incidence axis−sample c-axis " and "sample c-axis−emission axis". Then, L_A is the coefficient of angular asymmetry of photoelectrons, J_0 is the incident photon flux, T_{tr} is the transmission function of the analyzer, ξ_A is the atomic concentration of element A in the sample compound and λ_{IMFP} is the inelastic mean

free path of electrons in the compound.

The Eq. 6.2 can be much simplified under assumptions that the surface is homogeneous in x and y directions and it is homogeneously illuminated over area Σ, that the input aperture of the analyzer is small (γ and ζ dependences vanish), and that the measurements are done at constant analyzer energy (CAE mode). The simplified expression is then

$$I_A = J_0 \Sigma S_A(KE_A) \int_0^\infty \xi_A(z) \exp\left[-\frac{z}{\lambda_{IMFP}(KE_A)\cos(\phi)}\right] dz \quad , \qquad (6.3)$$

where S_A is an *analyzer sensitivity factor*, which depends on the experiment geometry and therefore is characteristic for an element A line measured in one instrument, at a given incident photon energy hf.

The Eq. 6.3 can be used for analysis of z-dependence of element A concentration, the *depth profile*, in two ways. We can vary the angle ϕ, while keeping all else (especially the incident energy hf) constant, or we can vary the incident energy and keep the angle fixed (usually at $\phi = 0$ for best signal-to-background ratio). The standalone instrument described above did not allow variation of x-ray energy. The beamline instrument allowed for both and both dependences were measured. Because, however, the sensitivities S_A depend strongly on incident energy hf and their values were not available for the analysis, it is only the angle-dependent photoemission spectra that we analyzed and present below.

The depth profiling using angular dependence of $I_A(\phi)$ has been applied to the relative concentration of Strontium and Lanthanum, $\frac{\xi_{Sr}}{\xi_{La}}$, and in the simplest form, which was only applied to our data, it works as follows. As the ϕ rises, the decay constant $\lambda_{IMFP}\cos(\phi)$, called the "information depth", drops. This means that the information about the depth-dependent concentration $\xi(z)$ contained in the intensity I_A is coming from smaller "average" depth. If we only measure a single photoelectron

peak intensity at various angles, there is always a significant error induced by the fact, that the rotation axis of the instrument is not aligned with the sample surface plane and therefore intensity may vary due to morphological imperfections of the crystal, or misalignment with respect to the analyzer axis. Measuring *relative* concentrations of elements eliminates these problems by large part, because the lines of the two elements in question are measured always at the same conditions[32]. The qualitative question of the quantitative analysis is: "Does the relative concentration of these two elements change with depth or not?" The qualitative answer to this question can be given by simple observation of the ratio of the intensities of the two peaks. This ratio I_A/I_B is not proportional to the concentrations ratio ξ_A/ξ_B, but equivalence holds that when the concentrations ratio varies with z, the intensity ratio varies with ϕ, and vice versa.

When we observe that I_A/I_B varies with ϕ, the appropriate analysis requires a knowledge of the "bulk standard" intensities of reference samples of each of the components. The intensities of peaks measured on such calibration samples of element A and B, denoted I_A^∞ and I_B^∞ respectively, then allow usage of an approximate formula

$$\frac{\xi_A}{\xi_B} \doteq F_{AB}^A \frac{I_A/I_A^\infty}{I_B/I_B^\infty} \quad , \tag{6.4}$$

where F_{AB}^A is given approximately by

$$F_{AB}^A \approx \frac{\lambda_{AB}(KE_A)\lambda_B(KE_B)r_A^3}{\lambda_{AB}(KE_B)\lambda_B(KE_A)r_B^3} \quad . \tag{6.5}$$

In this formula $\lambda_{AB}(KE_A)$ reads "inelastic mean free path of a photoelectron in an AB compound of a photoelectron emitted from a line of atom A", the r_A and r_B are respective atomic radii. This analysis avoids the need for sensitivity factors S_A, but requires separate measurement of calibration samples of element A and B, which is rarely possible.

[32]Provided the incident flux J_0 is constant. If it is not, steps can be taken to correct for this, to some extent, in the analysis.

Our approach to this analysis is that we assume λ_{IMFP} of the lines of interest Sr $3d$ at $BE \approx 133$ eV and La $4d$ at $BE \approx 100$ eV is about 2.4 nm, as predicted using Tanuma-Powell-Penn (TPP-2M) phenomenological formula. This formula has been developed by calibrating photoemission data of ordinary metals and there are sings, that in oxides λ_{IMFP} may be substantially larger. As we do not have any experiment-based calibration curve of LSMO λ_{IMFP}, we use the TPP-2M value, while acknowledging its possible error. As any changes in surface chemistry are bound to be localized to $1-4$ monolayers, i.e. $0.2-0.8$ nm, the measurement of LSMO at $\phi = 0$ can be regarded as measurement of bulk LSMO 36% with nominal chemical composition. As measurement proceeds to grazing angles, any ξ_{Sr}/ξ_{La} redistribution near surface will cause a deviation from the bulk value, which can be later quantified by proper analysis using profile modeling and Eq. 6.3.

6.4 Results

Firstly, the wide-range scans were measured for element identification in each experiment (standalone and beamline). The spectrum measured on the in-situ cleaved sample by the standalone laboratory instrument is displayed in Figure 6.3a. The photoelectron peaks in the spectrum are labeled. We observed the expected peaks of Lanthanum (La $3d$), Strontium (Sr $3d$ and Sr $3p$), Manganese (Mn $2p$) and Oxygen(O $1s$). In addition to them, contribution of Gold (Au $4f$) and Carbon (C $1s$) was detected.

6.4.1 Carbon Content Detection. In Figure 6.3b, beamline measured wide-range scan of core levels is presented. As the x-ray beam has a spot ~ 0.1 mm in diameter, there was no need for covering sample with gold. Measured signal only comes from the sample. This measurement reveals the same lanthanum, strontium, manganese and oxygen peaks, which the standalone instrument measured, but does not feature any gold peaks (naturally), and very importantly does not show any

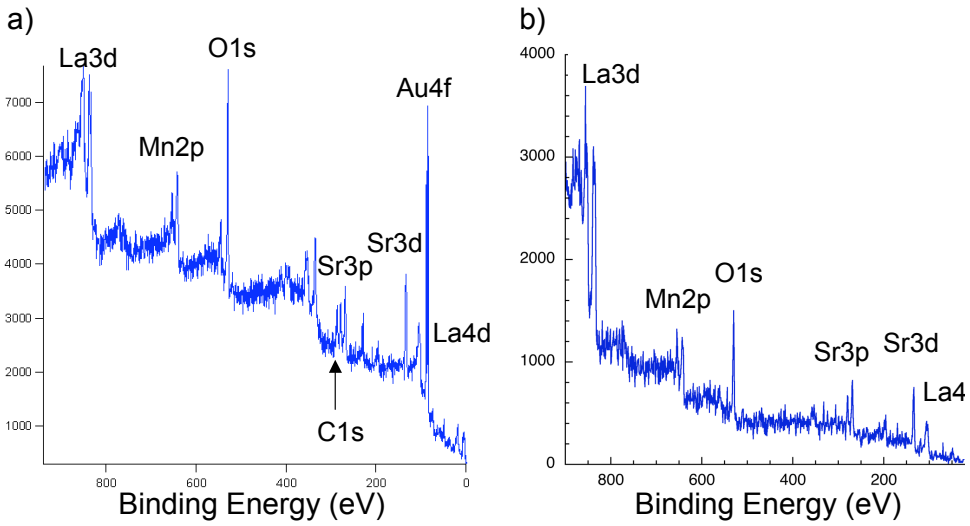

Figure 6.3. Wide Energy XPS Spectra of LSMO 36%. a) Measured in the Standalone Instrument, C 1s and Au 4f Present, b) Measured at a Beamline, C 1s and Au 4f Absent

trace of carbon. This verifies that the single-crystal manufacturing procedure results in material without any detectable amount of contaminants. We verified this by measuring detailed scans in an energy range $260 - 290$ eV and no trace of carbon C 1s peak was detected there either.

6.4.2 Strontium-Lanthanum Relative Concentration. Our standalone laboratory measurement was carried out at two angles, $\phi = 0$ and $\phi = 68^o$. We measured peaks La 3d and Sr 3d, which are displayed in Figure 6.4. We calculated the ratios of the intensities of the peaks and used formula in Eq. 6.4 assuming $I^{68^o}/I^{0^o} = I^{68^o}/I^{\infty}$ for each element and assuming validity of TPP-2M formula. The observed relative change in calculated ξ_{Sr}/ξ_{La} was an increase by $\sim 30\%$.

In the beamline experiment we measured peaks La 4d and Sr 3d at the following angles ϕ: $0^o, 17.5^o, 35^o, 52.5^o, 61^o, 65.5^o, 70^o, 75.5^o$. A series of spectra of lanthanum and strontium lines are displayed in Figure 6.5. We calculated the ratios of peak

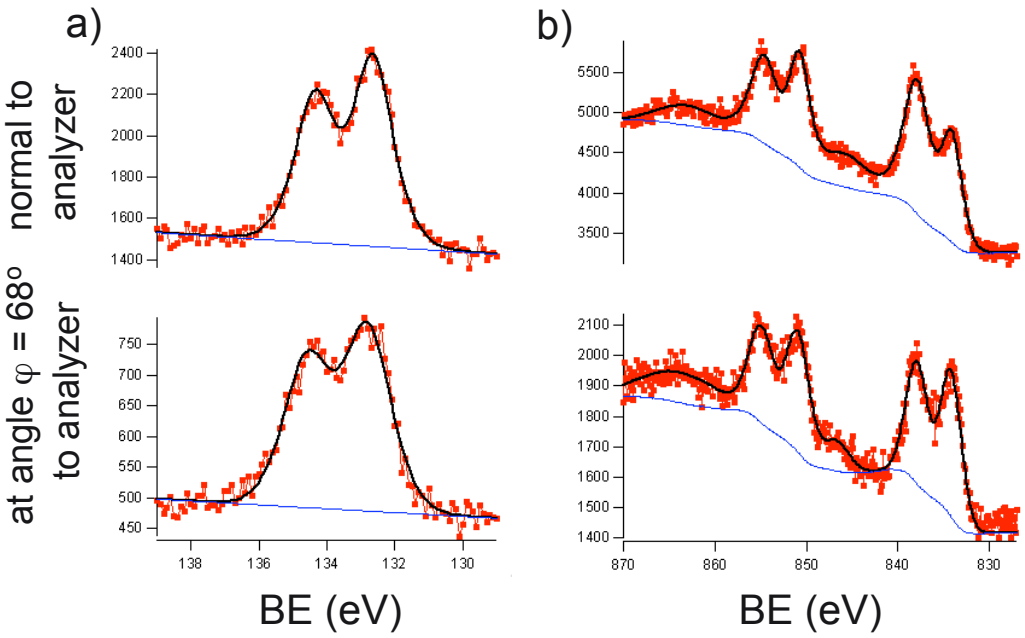

Figure 6.4. Pairs of Sr 3d and La 3d Spectra Measured in the Standalone Laboratory Experiment at Emission Angles $\phi = 0$ and $\phi = 68^o$.

intensities at every angle (some angles have been measured two times) and corrected to the difference between IMFP values of the lines La 4d and Sr 3d. The results were plotted in Figure 6.6 versus calculated information depth $\lambda_{IMFP}\cos(\phi)$. In this plot we observe that there in no observable change in the peak intensity ratio in the examined range of information depths $6 - 24$ Å. Due to the higher number of data points and better defined conditions of the beamline experiment compared to the standalone one, we conclude that in that range of information depths $6 - 24$ Å the relative concentration ξ_{Sr}/ξ_{La} does not change.

As a discussion of this result, let us stress out the note we made earlier about the information depths calibration. The λ_{IMFP} values were derived from a predictive formula, which has proven validity only for normal metals. Its applicability for estimates of oxide systems is uncertain. If, for example, the λ_{IMFP} corresponding to the range of kinetic energies $1350 - 1390$ eV is doubled, the information depth scale

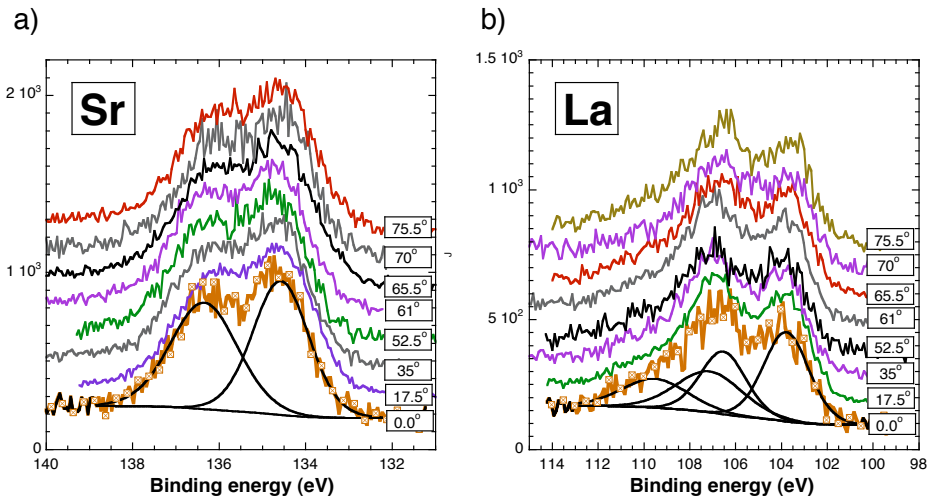

Figure 6.5. Series of Sr 3*d* and La 4*d* Spectra Measured in the Beamline Experiment at Various Emission Angles. Background and Fits Added for Zero-Angle Datasets.

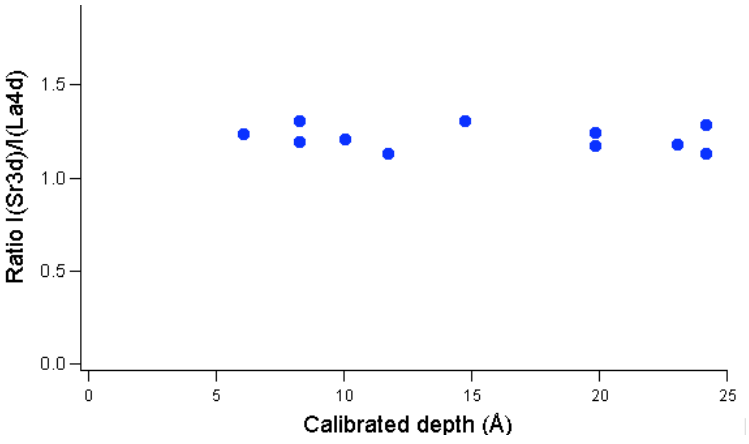

Figure 6.6. Dependence of Intensity Ratio I_{Sr3d}/I_{La4d} on Calibrated Information Depth. The Ratio Is Independent of the Information Depth in the Measured Range.

changes to $12 - 48$ Å, which would make our experiment completely inconclusive about concentration shifts within the first bi-layer, which is 1 nanometer thick.

Although we did no calculation of the atomic ratio ξ_{Sr}/ξ_{La} from the observed intensity ratio $I_{Sr}/I_{La} = 1.2$, the constant nature of the information depth dependence indicates that we the intensity ratio corresponded to the stoichiometric $\xi_{Sr}/\xi_{La} = 1.34$. This information may be used in future experiments for relative calibration of sensitivity factors of elements in LSMO.

CHAPTER 7

CONCLUSION

7.1 LSMO 36% Tunneling Spectroscopy Results

We have discovered that the characteristics of the Gold-LSMO point contact tunnel junctions at low temperatures consistently exhibit a a cusp-like zero-bias anomaly. We have shown in this thesis that this anomaly has the proportionality $dI/dV(V) \propto \sqrt{V}$, it is not significantly affected by application of external magnetic field up to μ_0H= 6 tesla, and it exhibits a temperature dependence (smearing) consistent with predictions of the theory of electron-electron interactions. All these features are in agreement with Al'tshuler and Aronov perturbation theory [8] of electron interactions in disordered three-dimensional systems, adapted for quasi two-dimensional system like the bi-layered LSMO by Abrikosov [3]. We conclude that the zero-bias anomaly is due to a Coulomb electron-electron interactions effect on the metallic density of states of the bi-layered LSMO 36%. This conclusion is indirectly supported by our reasoned elimination of a number of other mechanisms known to produce negative zero-bias anomalies in the tunneling spectra. The only alternative to the electron-electron interactions, which could not be completely eliminated by reasoning, is a special case of inelastic tunneling channel in the barrier, when the continuum of inelastic modes rises as $\sqrt{\mathcal{E}}$. The strongest point in favor of electron-electron interactions here is, that the theory not only predicts the right effect in the tunneling spectra $I(V)$ and $dI/dV(V)$, it also correctly predicts the temperature dependence of bulk conductivity $\sigma(T) \propto T$. No barrier effect can make any predictions on bulk material properties such as conductivity. So far the only alternative model explaining $\sigma(T) \propto T$ proportionality was the spin glass model, but as it predicts significant difference between LSMO 36% and LSMO 40%, which has never been observed, it can be disregarded. Based on solid evidence we state with high level of confidence, that

we have discovered the electron-electron interaction correlation effect in the density of states of LSMO 36%.

By calculating the expected elastic scattering time using Abrikosov's formulae we obtained values $\tau = 13 \pm 3$ femtosecond. These are about $2 - 3$ times larger than values $\tau = 5.0$ fs [56] or $\tau = 6.6$ fs [36], which we obtained independently from published measurements of LSMO 36% using angle-resolved photoelectron spectroscopy. However, the estimates of τ from the characteristic energy range $\mathcal{E}_{CO}$ were consistent with the τ values calculated from the proportionality co-efficient between $\delta\nu/\nu_0(\mathcal{E})$ and $\sqrt{\mathcal{E}}$. This verifies that the observed state conservation is real. This is a significant advance in the field of tunneling observation of density of state effect due to electron-electron interactions. To date, a number of articles presented evidence of electron-electron interaction effects in the DOS of various materials, but due to ill-defined tunneling barriers in most systems no publication addressed the conservation of states of this effect. Apart from the observation of the DOS correlation itself, the observation of the state conservation is the second most important discovery. The discrepancy between $\tau = 10 - 15$ fs measured by us and $\tau = 5 - 6.6$ fs measured by ARPES can be accepted on the basis that the first-order theory of perturbations, which underlies all the available theories of electron-electron correlation in metals, was not meant to give correct predictions for too strongly correlated metals like LSMO. At Fermi energy $\delta\nu/\nu_0(\mathcal{E}_F) \sim 0.5 - 0.7\nu_0$, which shows that in the LSMO 36% the correlation effect if much stronger than acceptable by the assumptions of the theories. In this light, the agreement within a factor $2 - 3$ in numbers can be considered an unexpected success of the theory.

7.2 Study of the Surface Insulating Phase

By highly reproducible results of the point-contact spectroscopy, which were in a very good agreement with the general theory of coherent electron tunneling, we

confirmed the existence of an insulating phase on the surface of metallic LSMO 36% at low temperatures. This phase spans $1.3 - 1.6$ nm in point contact tunneling junctions, which corresponds to thickness of approximately one bi-layer. We observed the barrier height to be $\Phi \approx 280 - 350$ meV in the point contact tunnel junctions, which is in agreement with values $\Phi \approx 350 - 400$ meV published by Freeland et al. [18] for the LSMO 40%. The best large-range fits of tunneling characteristics were based on the coherent tunneling model with inclusion of a linear inelastic tunneling spectrum. We have found, however, that inclusion of the inelastic tunneling channels is not necessary to obtain reasonable estimates of nu_0 and that it had no influence on τ values derived from $dI/dV(V) \propto \sqrt{V}$ proportionality. Inclusion of the inelastic tunneling channels however significantly reduced the energy range $\mathcal{E}_{CO}$ of the correlation effect, which expanded the $\tau = \hbar/\mathcal{E}_{CO}$ estimates to the range $40 - 60$ fs. This increased discrepancy lead us to the conclusion that inelastic tunneling channels, although they improve the large-range fit of a model to the tunneling spectra, should be disregarded and confidence should be given to results obtained by purely elastic analysis. Nevertheless, we consider this a fulfilled duty, because inelastic processes could not be ruled out by reasoning in advance and they are frequently observed in tunneling spectra of other complex oxides, namely the cuprate superconductors. Disregarding the inelastic tunneling based on anything else but experimental evidence would have been improper.

We manufactured thin film LSMO 36%-on-gold junctions by in-situ single-crystal cleaving and gold deposition, and subsequent patterning using the focused ion beam. Analysis of the thin film data showed that gold deposition lowered the instability threshold, but we were able to fit the data with the same tunneling model as the point contact data. The effective barrier parameters obtained on the thin film junctions were reduced to $t_0 = 1.1 \pm 0.1$ nm and $\Phi = 140 - 200$ meV. We took the applicability of the tunneling model as indication that the thin film junctions are still

tunneling junctions. In other words, the insulating phase persisted under a 50μm thin film of gold. We were able to utilize this fact in a procedure of an approximate calibration of the point contact junctions' areas.

The more detailed and reliable of our XPS measurements of an in-situ cleaved LSMO 36% sample showed no changes of lanthanum and strontium relative concentration near the surface of LSMO 36%. Angular dependence measured between 0^o and 75.5^o emission angles showed no variation. Using the standard Tanuma-Powell-Penn phenomenological formula for determination of the inelastic mean free path, we calibrated the range of angles as $6 - 24$ Å information depth. Indications exist that the TPP predictive formula underestimates the IMFP, because it was developed based on data of ordinary metals. However, this does not influence the conclusion that our experiment we entirely inconclusive with respect to concentration fluctuations in the first three atomic monolayers and another experiment will need to be performed, perhaps measuring up to 89^o emission angle, to verify recent LEED results indicating strontium enhancement in the surface monolayer.

APPENDIX A

THE DOUBLE-EXCHANGE MODEL

In 1951 Zener proposed [62][63] the double-exchange model to explain how ferromagnetic coupling arises in manganites. According to the DE model, ferromagnetic order is favorable when an indirect coupling via charge carriers exists between the incomplete d-shells of the Mn ions. Zener proposed such indirect coupling mechanism, where electron transfer from one Mn ion to another happens in fact via simultaneous transfer of two electrons: one from the initial ion to the apical oxygen, the other one from that oxygen to the final manganese ion, as visualized in Figure A.1a. There are two states then, $\psi_1 : [Mn^{3+}O^{2-}Mn^{4+}]$ and $\psi_2 : [Mn^{4+}O^{2-}Mn^{3+}]$, which are degenerate in energy, if core spins of the Mn ions are parallel. This is because the carrier spin does not change in the hopping process and Hund's coupling fines misalignment of unpaired electrons.

These ideas were formalized by Anderson and Hasegawa in 1955 [9]. The details of their calculation is not of great importance, but there is an important results coming out. It says that a semi-classical model, one that treats manganese core spins as three-dimensional vectors of magnetic moment rather than quantum operators and numbers, gives a very good approximation of the quantum picture. It becomes transparent that if the core spins are considered classical and with an angle θ between the nearest-neighbor ones (see Figure A.1b), the effective hopping amplitude becomes proportional to $cos(\theta/2)$. When we move from a pair of coupled Mn ions to a model manganite crystal, the local angle θ gets replaced by a mean value throughout all nearest-neighbor pairs $\langle\theta\rangle$ and bulk conductivity turns out obeying the relation

$$\sigma \propto M^2 \propto cos^2\left(\frac{\langle\theta\rangle}{2}\right) \quad . \tag{A.1}$$

When $\langle\theta\rangle = 0$, order is ferromagnetic and the conductance is the largest, while if $\langle\theta\rangle = \pi$, order is anfi-ferromagnetic and conductance drops down to thermally activated (insulating) level. Full quantum version of this process has been described in 1972 by Kubo and Ohata [29]. Later, theoretical work and computer simulations

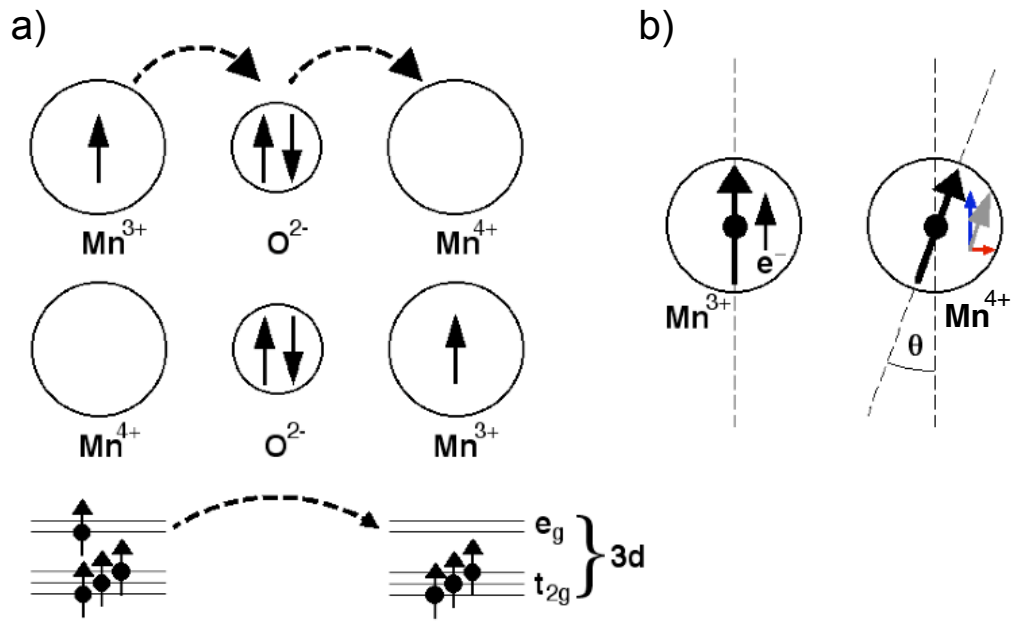

Figure A.1. Illustration to the Double-Exchange Mechanism. a) Simultaneous Two-Electron Hopping, b) Angular Dependence of Hopping. The Local Transport Probability Depends on Angle θ as $cos^2(\theta/2)$.

have been successfully carried out that avoid the apical oxygen in the construction of Hamiltonian, while still give rise to FM coupling from large Hund's coupling and e_g electron kinetic energy optimization. These models are, however, still referred to as *double-exchange* models and remain consistent with Eq. A.1. The importance of double-exchange for our later discussion lies in explaining the existence of a conduction band in manganites, and in providing the Eq. A.1 relation between conductivity and magnetization.

APPENDIX B

FUNDAMENTALS OF WEAK LOCALIZATION

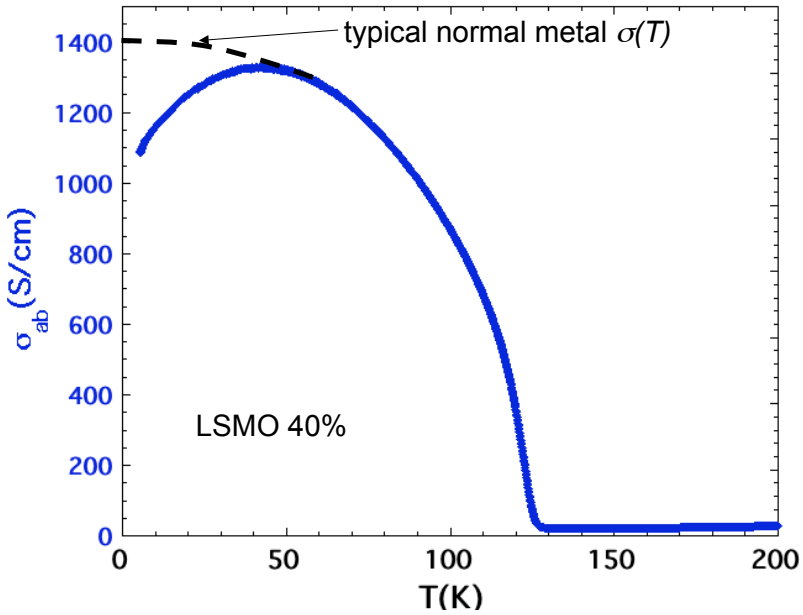

Figure B.1. Temperature Dependence of *ab*-Plane Conductivity of LSMO 40% (Solid Blue/Grey Line). Sketch of $\sigma(T)$ of a Metal Without Interaction Effects Added as a Dashed Line. Data Courtesy of Dr. K. E. Gray, Published with Permission.

Using the maximum metallic resistivity criterion in Section 1.4 we demonstrated that classical theory of metallic conductivity may not be sufficient to describe the conductivity in LSMO. Experimental evidence of this came from the measurements of temperature dependence of LSMO 40% bulk conductivity [43][34] exhibit an anomalous temperature dependence of conductivity of the metallic phase at low temperatures, see Figure B.1. It is known [10] that in classical metals the bulk conductivity rises with decreasing temperature and reach a finite value at zero temperature limit, while $\frac{\partial\sigma}{\partial T}(T = 0\text{K}) = 0$. In metals metals the low-temperature conductivity limit is caused by electron scattering on defects and impurities. The density of states is constant in temperature, and the diffusivity $\mathcal{D}$ is tied to temperature via electron scattering on the metal crystal lattice, the electron-phonon scattering. With rising temperature the population of phonons grows, causing more scattering and, therefore, lowering the diffusivity.

As shown in Figure B.1, conductivity of LSMO 40% reaches maximum at ∼50 K, and then drops with decreasing temperature to reach a finite value in the zero temperature limit. This temperature dependence is very similar to the σ_{ab} of LSMO 36% has been shown in Figure 1.6 in the $\sqrt{T}$ scale. The dependence is typical for disordered metals, metals heavily doped with impurities[14, 57], insulators doped with metallic elements [37, 38] and granular metals[17]. However, the same dependence is predicted by several quite different theories: quantum interference, spin glass (tied to the double-exchange model of conductivity in manganites) and electron-electron Coulomb interactions. The LSMO has a well defined crystal structure, but there is electronic disorder (disorder in local potentials) introduced by the mixed doping with divalent and trivalent elements. It is possible, therefore, that one or more of the above listed effects give rise to the observed anomalous temperature dependence of conductivity. Okuda et al., who were the first to publish the low-temperature $\sigma(T)$ data, classified the effect as "weak localization". This in their terminology encompassed both quantum interference and DOS correlation effects, which lead to the same temperature dependence $\sigma(T) \propto \sqrt{T}$ and cannot be distinguished in $\sigma(T)$.

Theory of quantum interference in disordered metals has been developed around 1980 and major advances in understanding of the phenomenon are due to Gor'kov et al. [21] and Larkin and Khmelnitskii [32]. The basic idea, which we describe in some more detail here, is that electron waves that scatter in random potential, experience self-interference due to several available scattering paths with similar phase shift. Practically, the main contribution comes from self-intersecting scattering paths. An electron wave can travel along the same path in two opposite directions, which leads to amplitude adding $\psi = \psi_\alpha + \psi_\beta$. The probability of this process is then expressed as $|\psi|^2 = |\psi_\alpha|^2 + |\psi_\beta|^2 + \psi_\alpha\psi_\beta^* + \psi_\alpha^*\psi_\beta$, where the first two terms correspond to classical single-path probabilities and the latter two terms are result of interference, which is inherent in quantum mechanics. The interference terms result in a negative correc-

tion to conductivity $\Delta\sigma(H,T) < 0$ with non-trivial dependence of magnetic field and temperature.

As the magnetoresistance effect has been observed in bi-layered LSMO at low temperatures [34], Abrikosov formulated his theory of weak localization for quasi-two-dimensional metals [3]. This theory helped Li et al. [33] [34] extract important macroscopic values from the fits to the LSMO 40% magnetoconductance data. These values were: elastic mean free path $\hat{l} \sim 1.44$ nm, ratio of inelastic to elastic scattering times $\tau_\Phi/\tau \sim 4336$, product of Fermi energy and electic scattering time $\varepsilon_F\tau/\hbar \sim 2.93$, and product of inter-bi-layer tight-binding coupling constant and the elastic scattering time $\alpha\tau/\hbar \sim 0.154$. The quantum interference analysis does not yield the elastic scattering time alone, though. The elastic scattering time τ is widely acknowledged as one of the central parameters in theories of conductivity. Valence-band photoemission (PES, UPS) measures v_F directly and τ can be derived as $\tau = \hat{l}/v_F$, when $\hat{l}$ is known.

As observed by Li et al., the change in LSMO 40% conductance at temperature 4.2 K was in the order of 3% of the total magnitude of σ_{ab} and σ_c, when the external magnetic field was in range $\mu_0 H = 0 - 7$ T. No saturation of the conductance was observed in that range of magnetic field. It was possible that also the other 30% of conductivity magnitude remaining to bring it to classical metallic conductivity characteristics (the expectation normal-metal $\sigma(T)$ was sketched in Figure B.1 could be a continuation of the same effect. The magnitude of the remaining fraction of σ, however, made in equally or more likely that another effect may be responsible for it. A spin-glass model was suggested by Chun et al. in 2001 [12] on LSMO 40%, i.e. on the *canted* phase. Later measurements of conductivity of (almost) fully plan-parallel ferromagnetic LSMO 36% exhibited no substantial difference with respect to LSMO 40%, which showed that spin glass behavior cannot be responsible for the major effect.

APPENDIX C

LOW-VOLTAGE APPROXIMATION OF TUNNELING CHARACTERISTICS

Under the assumption that $|V| << \Phi/e$ for all measured voltages, Simmons demonstrated [53] that the barrier profile $U(x,V) = \Phi - \frac{eV}{t_o}x$ can be approximated as $U(x,V) \doteq \bar{\Phi} - \frac{eV}{2}$. In this Approximation the tunnel current can be represented by

$$I(V) = \frac{eA}{2\pi h t_0^2}\{\left(\bar{\Phi} - \frac{eV}{2}\right) exp\left[-\frac{4\pi t_0 (2m)^{1/2}}{h}\left(\bar{\Phi} - \frac{eV}{2}\right)^{1/2}\right] - \left(\bar{\Phi} + \frac{eV}{2}\right) exp\left[-\frac{4\pi t_0 (2m)^{1/2}}{h}\left(\bar{\Phi} + \frac{eV}{2}\right)^{1/2}\right]\} \quad , \quad \text{(C.1)}$$

where A is junction area and all other symbols have been defined before. If we perform Taylor expansion on the above equation in the first two non-zero terms $I(V) = aV + bV^3$, the coefficients of the expansion are given analytically by

$$a = \frac{Ae^2(2m\bar{\Phi})^{1/2}}{t_0 h^2} exp\left(-\frac{4\pi t_0 (2m)^{1/2}}{h}\bar{\Phi}\right) \quad , \quad \text{(C.2)}$$

and

$$\frac{b}{a} = \frac{\tilde{A} t_0 e^2}{96\Phi^{3/2}} \frac{\tilde{A}^2\Phi - 3\tilde{A}\sqrt{\Phi} - 3}{\tilde{A} t_0 \sqrt{\Phi} - 2} \quad , \quad \text{(C.3)}$$

where A is the junction area and $\tilde{A} = 2\sqrt{2m}/\hbar$.

By these relations the coefficiens are tied to barrier parameters and if condition $|V| << \Phi/e$ is satisfied, one can use the expansion parameters of tunneling background to obtain the barrier parameters, which are otherwise unknown. Unfortunately, this was not the case of our tunneling experiment, where using a tunnel barrier $\Phi \sim 300$ meV we had to address features that extended over $\pm 100 - 130$ mV range. As we state in Chapter 3, we have verified that in our situation the tunneling barrier effect (tunneling background) still can be approximated with an expansion $I(V) = aV + bV^3$ alike Simmons', wherever $|V| < \Phi/e$ reliably holds. However, the Equations C.2 and C.3 cannot be used to estimate the rectangular barrier parameters more precisely than down to a factor of 2 in either parameter, Φ or t_0.

APPENDIX D

ENERGY SCALE AND SCATTERING TIME DETERMINED FROM ARPES

There is a distinct agreement of the energy scale $\mathcal{E}_{CO}$ derived from our tunneling analysis and other energy scales Sun et al. [56] and Mannella et al. [36] observed in the angle-resolved photoemmission (ARPES) dispersion spectra. In this appendix we republish several figures from their articles, with permission from the authors. As the figures were published in color (both on-lina end in print), we have to apologize for the limited resolution ability in greyscale, the requirement for the official submission of this thesis.

Sun et al focused at the observation of LSMO 38% photoemission spectrum in the $(\pi, 0)$ direction, as highlighted in the sketch in Figure D.1a. This is the direction of the in-plane $\mathrm{Mn} - 0$ bonds and, as shown in the plot b) in the figure, the photoemission shows distinct maxima at the Fermi surfaces in that direction. The intensity graphics in part c) of the figure shows the energy dispersion $E(k_x)$ in the antibonding momentum scale, where band structure can be observed. A red (grey arrow points to a region in the dispersion plot near Fermi energy, around $k_x \sim -0.17\pi/a$, where a sharp intensity peak is observed. The peak is shown in part d) of the graphics, where it is compared with an equivalent spectrum of LSMO 40%, which showed only rather indistinct structure at the same energy.

A slice of the dispersion graph c) in Figure D.1 is presented as part a) of Figure D.2. The region, where the peak exists is in the greyscale display best pointed out as the white-surrounded grey line section between the left-hand ends of the overlying arrows. It can be seen from this plot already that the quasiparticle peak "lives" in the energy range approximately $0 - 50$ meV. By tracing this peak in the intensity graph, plot Figure D.2b was created[33]. It shows that there is a peak in the bonding dispersion graphics, which exists in the same energy scale. This plot then is a repre-

[33]Parts c) and d) of the original figure in Ref. [56] are not important to our discussion, so they were omitted from Figure D.2.

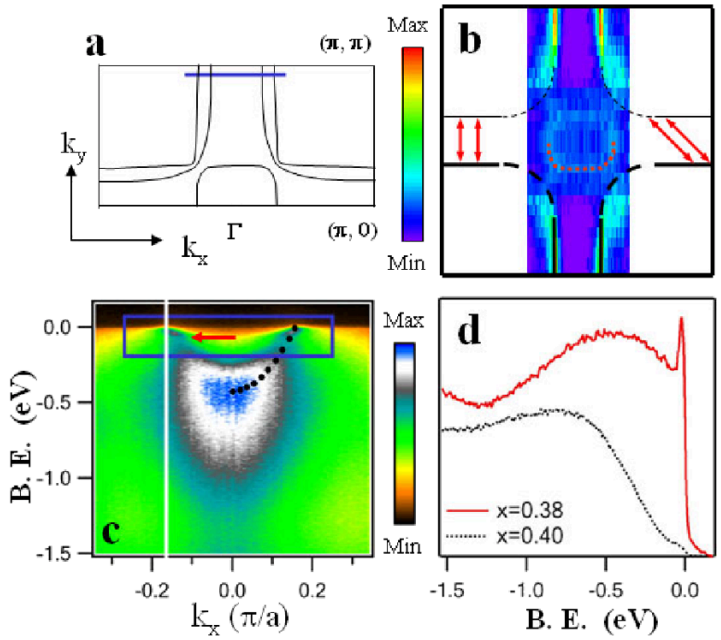

Figure D.1. Low Temperature (20K) ARPES Data from LSMO 38%, Quasiparticle Peak Observed along the $(\pi, 0)$ Direction in k-Space. Figure Described in the Text. Reprinted Fig.1, with Permission, from [56] Z. Sun et al., Physical Review Letters, Vol.97, 056401 (2006). Copyright (2006) by the American Physical Society.

sentation of the band structure of the material, and for comparison the free-electron band modelled by local-density approximation (LDA) was added to this plot in the form of black markers. It is obvious that the peak dispersion deviates considerably from the free-electron model. We can therefore speak about *renormalization* of the band structure near the Fermi energy.

The Fermi velocity $v_F = (1/\hbar)(\partial\mathcal{E}/\partial k)$ in the renormalized range has a value $\sim 2.9 \times 10^7$ cm.s^{-1}, which is about a half of the free-electron model value[34]. Using this value of the Fermi velocity and the elastic mean free path $\hat{l}$ measured by Li et al. by quantum interference on LSMO 40% we obtain an estimate of the elastic scatering time $\tau \approx 5$ fs.

---

[34]High slope in the range $60 - 120$ meV is an artifact and should be disregarded from analysis.

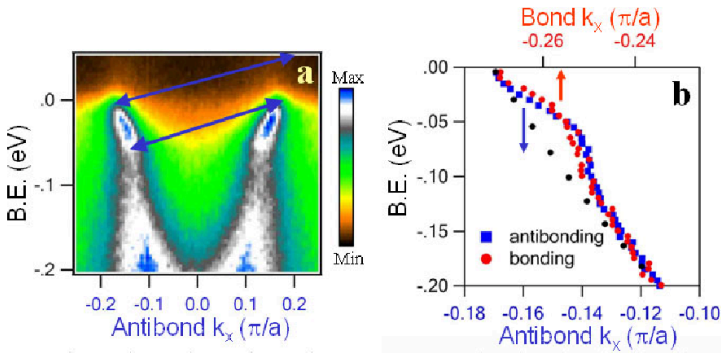

Figure D.2. The LSMO 38% ARPES Data Along the $(\pi, 0)$ Direction. Figure Is Descibed in the Text. Reprinted from Figure 2 in Ref. [56] with Permission from the Publisher.

Mannella et al. did ARPES measurement of energy dispersion in LSMO 40% along the (π, π) direction and they also observed a quasiparticle peak in the photo-electron spectrum, as shown in the re-printed Figure D.3. In the figure, the series a)$-$c) represents "zooming in" onto the Fermi energy in the intensity dispersion graph $E(k)$, while series of plots d)$-$e) represents the same zooming in line graphs. The lines are a sampling of the above color intensity plots and in geyscale provide better distinction of the (π, π) direction quasiparticle peak. Having traced the maxima in the energy dispersion plot, authors created Figure D.4. The broad maximum position is given by the "Hump (EDC)" dataset (the one that has local extreme at the point $\mathcal{E} = 0.3$ eV, $k = 0.35$ Å^{-1}), and the sharp maximum positions are represented by the "Quasiparticle peak (EDC)" dataset, which is best viewed in the inset. In the inset we observe that the quasiparticle peak "lives" in the energy range $0-40$ meV from the Fermi energy. The "Hump" dispersion curve agrees well with a model curve calculated in local-density approximation (LDA) and represents the free-electron band.

Band slopes in $E(k)$ dispersion plots (the energy dispersion curves, EDC) have different meaning that $E(k_x)$ (the momentum dispersion curves, MDC) because of the loss of angular information. Mannella et al. chose a different approach to estimate τ

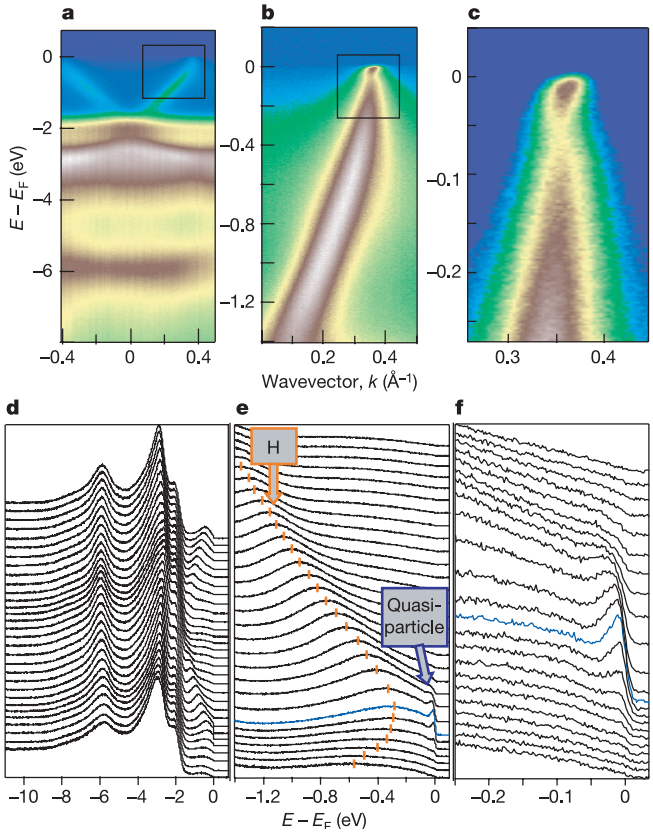

Figure D.3. LSMO 40% ARPES Dispersion Plots along the (π, π) Direction in k-Space. Figure Described in the Text. Reprint of Figure 1 in Reference [36] with Permission from the Authors.

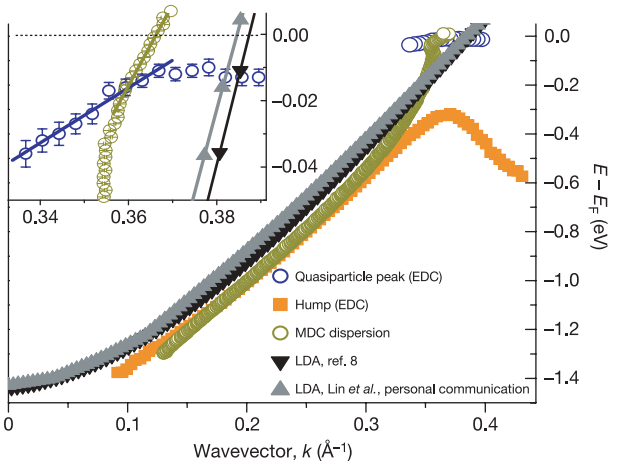

Figure D.4. LSMO 40% Band Structure along the (π, π) Direction Continued. Figure Described in the Text. Reprint of Figure 2 in Reference [36] with Permission from the Authors.

than we did based on the results of Sun et al. A quasiparticle lifetime can be estimated from the width of the quasiparticle peak in the energy spectra in Figure D.3e and assuming that the states along the (π, π) direction are those responsible for LSMO conductivity, the quasiparticle lifetime is then an estimate of the elastic scattering time τ. Mannella et al. published this estimate as 3.28 fs, however, in later private communication it transpired that an error had been made in the publication and that the correct estimate should be $\tau = 6.56$ fs.

To sum up, Sun et al. and Mannella et al. observed a quasiparticle peaks in the dispersion ARPES plots in the $(\pi, 0)$ and (π, π) direction, respectively. These peaks considerably renormalized the free electron band structure in the energy ranges $0 - 50$ meV and $0 - 35$ meV, respectively, which is in a remarkable agreement with the values $\mathcal{E}_{CO}$ we measured as the characteristic energy scale of the electron-electron interaction effects we observed in the density of states of LSMO 36%. To this date we have not found any straightforward explanation for this agreement of energy scales found by ARPES and tunneling. Explanation of this is a task for the future on the field of manganites.

Both ARPES publications also give estimates of material parameters tightly linked to conductivity of LSMO. Sun et al. publish the momentum dispersion curves, from which we derived an estimate of Fermi velocity related to the quasiparticle peak, and the elastic scattering time $\tau = 5.0$ fs. Mannella et al. let us know that their estimate of the quasiparticle lifetime (and hence the elastic scattering time) is $\tau = 6.6$ fs. There are open questions in the derivation of these estimates, because the methods used are not fully compatible and each one is more appropriate in different circumstances. The estimate we made from our point contact tunneling conductance is the average $\overline{\tau} = 15$ fs. Due to approximations made in the theory of electron-electron interactions, and because it is a perturbation theory applied for a metal outside the

preturbation limit, we consider the three-fold difference between our results a success. It has been stated in the discussion of Chapter 3 that Abrikosov's theory is expected to give estimates, which may be $2-3$ times off. We consider it a success that our measurement and the ARPES measurement results are within the error bars of the theory of electron-electron interactions.

BIBLIOGRAPHY

[1] Abrahams, E., P. W. Anderson, P. A. Lee, and T. V. Ramakrishnan. "Quasiparticle Lifetime in Disordered Two-Dimensional Metals." Physical Review B. 24.12 (1981): 6783–6789.

[2] Abrikosov, A. A. Fundamentals of the Theory of Metals. Amsterdam: Elsevier Science Publishing B. V. (1988).

[3] Abrikosov, A. A. "Quantum Interference Effects in Quasi-Two-Dimensional Metals." Physical Review B. 61.11 (2000): 7770–7774.

[4] Adler, J. G. "Nonequilibrium Electron Tunneling in Metal-Insulator-Metal Junctions." Physical Review B. 11.8 (1975): 2812–2820.

[5] Altshuler, B. L. and A. G. Aronov. "Contribution to the Theory of Disordered Metals in Strongly Doped Semiconductors." Soviet Physics JETP. 50.5 (1979): 968–976.

[6] Altshuler, B. L. and A. G. Aronov. "Damping of One-Electron Excitations in Metals." JETP Letters. 30.8 (1979): 482–484.

[7] Altshuler, B. L. and A. G. Aronov. "Zero Bias Anomaly in Tunnel Resistance and Electron-Electron Interaction." Solid State Communications. 30 (1979): 115–117.

[8] Altshuler, B. L. and A. G. Aronov. "Electron-Electron Interaction in Disordered Conductors." In A. L. Efros and M. Pollak, eds., Modern Problems in Condensed Matter Sciences, Volume 10. Amsterdam: North-Holland (1985), 1–154.

[9] Anderson, P. W. and H. Hasegawa. "Considerations on Double Exchange." Physical Review. 100.2 (1955): 675.

[10] Ashcroft, N. W. and N. D. Mermin. Solid State Physics. Orlando, Florida: Harcourt College Publishing, Inc. (1976).

[11] Bardeen, J. "Tunneling from a Many-Particle Point of View." Physical Review Letters. 6.2 (1961): 57–59.

[12] Chun, S. H., Y. Lyanda-Geller, M. B. Salamon, R. Suryanarayanan, G. Dhalenne, and A. Revcolevschi. "Reentrant Spin Glass Behavior in Layered Manganite $La_{1.2}Sr_{1.8}Mn_2O_7$." Journal of Applied Physics. 90.12 (2001): 6307–6311.

[13] Cooper, J. R. and A. F. G. Wyatt. "Systematic Behaviour of Tunnel Junctions Doped with 3d Atoms." Journal of Physics F. 3.7 (1973): L120–L124.

[14] Dolan, G. J. and D. D. Osheroff. "Nonmetallic Conduction in Thin Metal Films at Low Temperatures." Physical Review Letters. 43.10 (1979): 721–724.

[15] Duke, C. B. and M. E. Alferieff. "Field Emission Through Atoms Adsorbed on a Metal Surface." Journal of Chemical Physics, 46.3 (1967): 923–937.

[16] Dulić, D., D. van der Marel, A. A. Tsvetkov, W. N. Hardy, Z. F. Ren, J. H. Wang, and B. A. Willemsen. "c-Axis Penetration Depth and Interlayer Conductivity in the Thallium-Based Cuprate Superconductors." Physical Review B. 60.22 (1999): R15051–R15054.

[17] Dynes, R. C. and J. P. Garno. "Metal-Insulator Transitions in Granular Aluminum." Physical Review Letters. 46.2 (1981): 137–140.

[18] Freeland, J. W., K. E. Gray, L. Ozyuzer, P. Berghuis, E. Badica, J. Kavich, H. Zheng, and J. F. Mitchell. "Full Bulk Spin Polarization and Intrinsic Tunnel Barriers at the Surface of Layered Manganites." Nature Materials. 4.1 (2005): 62–67.

[19] Frenkel, J. "On the Electrical Resistance of Contacts Between Solid Conductors." Physical Review. 36 (1930): 1604–1618.

[20] Giaever, I. and H. R. Zeller. "Superconductivity of Small Tin Particles Measured by Tunneling." Physical Review Letters. 20.26 (1968): 1504–1507.

[21] Gor'kov, L. P., A. I. Larkin, and D. E. Khmel'nitskii. "Quasiparticle Conductivity in a Two-Dimensional Random Potential." JETP Letters. 30.4 (1979): 248–252.

[22] Hall, R. N., J. H. Racette, and H. Ehrenreich. "Direct Observation of Polarons and Phonons During Tunneling in Group $3-5$ Semiconductor Junctions." Physical Review Letters. 4.9 (1960): 456–458.

[23] Harrison, W. A. "Tunneling from an Independent-Particle Point of View." Physical Review. 123.1 (1961): 85–89.

[24] Holm, R. and B. Kirchstein. Zeitschrift für Technische Physik. 16 (1935): 448.

[25] Holm, R. and B. Kirchstein. Physische Zeitschrift. 36 (1939): 882.

[26] Jin, S., T. H. Tiefel, M. McCormack, R. A. Fastnacht, R. Ramesh, and L. H. Chen. "Thousandfold Change in Resistivity in Magnetoresistive La-Ca-Mn-O Films." Science. 264 (1994): 413–415.

[27] Jonker, G. H. and J. H. van Santen. "Ferromagnetic Compounds of Manganese with Perovskite Structure." Physica. 16.3 (1950): 337–349.

[28] Kirtley, J. R., S. Washburn, and D. J. Scalapino. "Origin of the Linear Tunneling Conductance Background." Physical Review B. 45.1 (1992): 336–346.

[29] Kubo, K. and N. Ohata. "A Quantum Theory of Double Exchange. I." Journal of Physical Society of Japan. 33.1 (1972): 21–32.

[30] Kurter, C., L. Ozyuzer, D. Mazur, J. F. Zasadzinski, K. E. Gray, H. Claus, D. Rosenmann, and D. G. Hinks. "Evidence of Strong-Coupled Superconductivity in CaC_6 from Tunneling Spectroscopy." (Dec 2006). In Preparation.

[31] Kusters, R. M., J. Singleton, D. A. Keen, R. McGreevy, and W. Hayes. "Magnetoresistance Measurement on the Magnetic Semiconductor $Nd_{0.5}Pb_{0.5}MnO_3$." Physica B. 155.1-3 (1989): 362365.

[32] Larkin, A. I. and D. E. Khmel'nitskii. "Anderson Localization and Anomalous Magnetoresistance." Uspekhi Fizicheskikh Nauk. 136 (1982): 536–538.

[33] Li, Q. and K. E. Gray. "Numerical Method to Test a Theoretical Model of the Quantum Interference Effect in Layered Manganites." Physical Review B. 63.5 (2001): 52413–52416.

[34] Li, Q., K. E. Gray, and J. F. Mitchell. "Metallic Conductance Below T_C Inferred by Quantum Interference Effects in Layered $La_{1.2}Sr_{1.8}Mn_2O_7$." Physical Review B. 63.2 (2000): 24417–24422.

[35] Li, Q., K. E. Gray, J. F. Mitchell, A. Berger, and R. Osgood. "Double-Exchange Selection Rule for the c-Axis Conductivity in Layered $La_{2-2x}Sr_{1+2x}Mn_2O_7$ Single Crystals Below T_C." Physical Review B. 61.14 (2000): 9542–9548.

[36] Mannella, N., W. L. Yang, X. J. Zhou, H. Zheng, J. F. Mitchell, J. Zaanen, T. P. Devereaux, N. Nagaosa, Z. Hussain, and Z.-X. Shen. "Nodal Quasiparticle in Pseudogapped Colossal Magnetoresistive Manganites." Nature. 438.24 (2005): 474–478.

[37] Massey, J. G. and M. Lee. "Direct Observation of the Coulomb Correlation Gap in a Nonmetallic Semiconductor, Si:B." Physical Review Letters. 75.23 (1995): 4266–4269.

[38] Massey, J. G. and M. Lee. "Electron Tunneling Study of Coulomb Correlations Across the Metal-Insulator Transition in Si:B." Physical Review Letters. 77.16 (1996): 3399–3402.

[39] Mazur, D., J. F. Zasadzinski, K. E. Gray, Y. C. Ma, S. L. Yan, and N. L. Wang. "Point Contact Tunneling Spectroscopy od $Tl_2Ba_2CaCu_2O_8$ Single Crystals and Thin Films." (Dec 2006). Submitted to Physical Review B.

[40] Mazur, D., K. E. Gray, J. F. Zasadzinski, L. Ozyuzer, I. Beloborodov, H. Zheng, and J. F. Mitchell. "Energy Range of State Conservation for Coulomb Interaction Effects in $La_{2-2x}Sr_{1+2x}Mn_2O_7$." (2007). In Preparation.

[41] Mitra, J., M. Paranjape, A. K. Raychaudhuri, N. D. Mathur, and M. G. Blamire. "Temperature Dependence of Density of States Near the Fermi Level in a Strain-Free Epitaxial Film of the Hole-Doped Manganite $La_{0.7}Ca_{0.3}MnO_3$." Physical Review B. 71.9 (2005): 094426–094433.

[42] Mitra, J., A. K. Raychaudhuri, Y. M. Mukovskii, and D. Shulyatev. "Depletion of the Density of States at the Fermi Level in Metallic Colossal Magnetoresistive Manganites." Physical Review B. 68.13 (2003): 134428–134435.

[43] Okuda, T., T. Kimura, and Y. Tokura. "Low-Temperature Transport Properties in a Bilayered Manganite $La_{1.3}Sr_{1.7}Mn_2O7$." Physical Review B. 60.5 (1999): 3370–3374.

[44] Ott, F., M. Viret, R. Borges, R. Lyonnet, E. Jacquet, C. Fermon, and J.-P. Contour. "Interface Magnetism of $La_{0.7}Sr_{0.3}MnO_3$ Thin Films Studied by Neutron Reflectometry." Journal of Magnetism and Magnetic Materials. 211.1-3 (2000): 200–205.

[45] Ozyuzer, L. Doping Dependence of Quasiparticle and Josephson Tunneling in high-T_C Superconductors. Ph.D. thesis, Illinois Institute of Technology (Jul 1999).

[46] Ozyuzer, L., Z. Yusof, J. F. Zasadzinski, R. Mogilevsky, D. G. Hinks, and K. E. Gray. "Evidence of $d_{x^2-y^2}$ Symmetry in the Tunneling Conductance Density of States of $Tl_2Ba_2CuO_6$." Physical Review B (Rapid Communications). 57.6 (1998): R3245–R3248.

[47] Ozyuzer, L., J. F. Zasadzinski, and K. E. Gray. "Point Contact Tunneling Apparatus With Temperature and Magnetic Field Control." Cryogenics. 38.9 (1998): 911–915.

[48] Raychaudhuri, A. K., K. P. Rajeev, H. Srikanth, and N. Gayathri. "Metal-Insulator Transition in Perovskite Oxides: Tunneling Experiments." Physical Review B. 51.12 (1995): 7421–7428.

[49] Renner, C., G. Aeppli, B.-G. Kim, Y.-A. Soh, and S.-W. Cheong. "Atomic-Scale Images of Charge Ordering in a Mixed-Valence Manganite." Nature. 416.6680 (2002): 518–521.

[50] Rowell, J. M. and L. Y. L. Shen. "Zero-Bias Anomalies in Normal Metal Tunnel Junctions." Physical Review Letters. 17.1 (1966): 15–19.

[51] Schmidt, H. Tunneling Study of Two-Band Superconductivity in Magnesium Diboride. Ph.D. thesis, Illinois Institute of Technology, Chicago (Dec 2003).

[52] Searle, C. W. and S. T. Wang. "Studies of the Ionic Ferromagnet (LaPb)MnO_3. III. Ferromagnetic Resonance Studies." Canadian Journal of Physics. 47 (1969): 2703.

[53] Simmons, J. G. "Generalized Formula for the Electric Tunnel Effect Between Similar Electrodes Separated by a Thin Insulating Film." Journal of Applied Physics. 34.6 (1963): 1793–1803.

[54] Simmons, J. G. "Generalized Thermal J-V Characteristic for the Electric Tunnel Effect." Journal of Applied Physics. 35.9 (1964): 2655–2658.

[55] Stratton, R. "Volt-Current Characteristics for Tunneling Through Insulating Films." Journal of Physical Chemistry of Solids. 23 (1962): 1177–1190.

[56] Sun, Z., Y.-D. Chuang, A. V. Fedorov, J. F. Douglas, D. Reznik, F. Weber, N. Aliouane, D. N. Argyriou, H. Zheng, J. F. Mitchell, T. Kimura, Y. Tokura, A. Revcolevschi, and D. S. Dessau. "Quasiparticle Peaks, Kinks, and Electron-Phonon Coupling at the $(\pi, 0)$ Regions in the CMR Oxide $La_{2-2x}Sr_{1+2x}Mn_2O_7$." Physical Review Letters. 97.5 (2006): 056401–056404.

[57] van den Dries, L., C. van Haesendonck, Y. Bruynseraede, and G. Deutscher. "Two-Dimensional Localization in Thin Copper Films." Physical Review Letters. 46.8 (1981): 565–568.

[58] von Helmolt, R., J. Wecker, B. Holzapfel, L. Schultz, and K. Samwer. "Giant Negative Magnetoresistance in Perovskite $La_{2/3}Ba_{1/3}MnO_x$ Ferromagnetic Films." Physical Review Letters. 71.14 (1993): 2331–2333.

[59] Wolf, E. L. Principles of Electron Tunneling Spectroscopy. New York: Oxford University Press (1985).

[60] Xiong, G. C., Q. Li, H. L. Ju, S. N. Mao, L. Senapati, X. X. Xi, R. L. Greene, and T. Venkatesan. "Giant Magnetoresistance in Epitaxial $Nd_{0.7}Sr_{0.3}MnO_{3-\delta}$ Thin Films." Applied Physics Letters. 66.11 (1995): 1427–1429.

[61] Zasadzinski, J. F. "Tunneling Spectroscopy of Conventional and Unconventional Superconductors." In K. H. Bennemann and J. B. Ketterson, eds., The Physics of Superconductors, Volume I: Conventional and high-T_C superconductors. Berlin, Heidelberg, Germany: Springer-Verlag (2003), 591–646.

[62] Zener, C. "Interaction Between the *d*-Shells in the Transition Metals." Physical Review. 81.4 (1951): 440–444.

[63] Zener, C. "Interaction Between the *d*-Shells in the Transition Metals. II. Ferromagnetic Compounds of Manganese With Perovskite Structure." Physical Review. 82.3 (1951): 403–405.